Semiclassical Transport in Semiconductor Superlattices with Boundaries

Dissertation
zur Erlangung des Doktorgrades
der Naturwissenschaften (Dr. rer. nat.)
der Naturwissenschaftlichen Fakultät II - Physik
der Universität Regensburg

vorgelegt von
Bernhard Rieder
aus Ergolding
2004

Promotionsgesuch eingereicht am 9. September 2004
Promotionskolloquium am 28. Oktober 2004

Die Arbeit wurde von Prof. Dr. Joachim Keller angeleitet.

Prüfungsausschuß:

Vorsitzender:	Prof. Dr. Karl F. Renk
1. Gutachter:	Prof. Dr. Joachim Keller
2. Gutachter:	Prof. Dr. Milena Grifoni
Weiterer Prüfer:	Prof. Dr. Klaus Richter

Contents

Glossary iii

Introduction 1

1. Semiconductor superlattices and Gunn diodes 5

1.1 Miniband structure in semiconductor superlattices 5

1.2 Esaki-Tsu model 9

1.3 Ktitorov model 10

1.3.1 Static conductivity 11

1.3.2 High-frequency conductivity 12

1.4 Instabilities in negative differential conductivity (NDC) materials 14

1.4.1 Bulk instabilities 14

1.4.2 Boundary effects 18

1.5 Influence of a cavity 26

1.5.1 Delayed and quenched domains 27

1.5.2 Limited space-charge accumulation (LSA) mode 27

2. Transport models for the superlattice structures 33

2.1 Hierarchy of the approaches for semiconductor transport 33

2.2 Boundary conditions 36

2.2.1 Discontinuous transition 38

2.2.2 Continuous transition 43

2.3 Influence of the surrounding 47

2.3.1 Current circuit 47

2.3.2 Cavity 48

3. Results of the numerical transport treatment 51
3.1 Comparison of different models for a homogeneous system 51
3.1.1 DC transport 51
3.1.2 Behavior under external radiation 56
3.2 Inclusion of the boundaries 65
3.2.1 DC transport 66
3.2.2 Interaction with external radiation 72

4. Summary and Outlook 77
4.1 Summary 77
4.2 Outlook 81

A. Derivation of the driving term in the Boltzmann equation . . . 83

B. Derivation of the Ktitorov model 91

C. The drift-diffusion model 95

D. Tunneling 99
D.1 Zener tunneling 99
D.2 Tunneling through triangular barriers 105

E. The upwind procedure 107

F. Cavity 109

Literature 113

Glossary

a	crystal lattice constant
b	barrier width in the superlattice
β	$1/k_BT$
d	superlattice constant
δ	ν_ε/ν_v
$\delta\varepsilon$	energy difference of a bulk electron to the miniband edge
D	diffusion coefficient
Δ	miniband width
e	electron charge
ε	electron energy
$\tilde{\varepsilon}$	electron energy measured from the miniband center
ε_0	band edge of the lowest miniband
ε_1	band edge of the second miniband
ε_d	mean electron energy in a static homogeneous system with applied field
ε_T	mean thermal energy of electrons in a miniband
ε_{off}	energy offset of the miniband compared to the bulk material
ϵ	dielectric constant in the material
ϵ_0	dielectric constant of vacuum
$\mathbf{E}$	negative electric field
E	z-component of the electric field
E'	field in units of the critical field E_c
E_0	DC field amplitude
E_1	AC field amplitude
E_c	critical field, defined by $E_c = \hbar/ed\tau$
E_c^{ET}	critical field in the Esaki-Tsu model
f	frequency
f	electron distribution function in phase space
f_0	equilibrium distribution function in phase space
g	growth factor in the LSA mode
$\hbar$	Planck's constant
η	creation efficiency for high-frequency radiation
I_n	modified Bessel functions
$\mathcal{I}_n$	phase space integral $\int \cos(nkd) f_0(k) dk$
j_d	drift current density env_d

J_n	Bessel functions
k	electron wave vector in z-direction
$k_\perp$	electron wave vector perpendicular to the z-direction
L	superlattice length
LSA	limited space-charge accumulation
$m^\star$	effective mass of an electron in GaAs
$m_b^\star$	effective mass in the barrier material
$m_w^\star$	effective mass in the well material
$m_l^\star$	effective mass of an electron at the bottom of the miniband
μ_d	differential mobility $\partial v_d/\partial E_0$
μ_ω	high-frequency mobility v_ω/E_1
n	electron density
n_0	doping density
ν	scattering frequency
ν_ε	inelastic scattering frequency
ν_{el}	elastic scattering frequency
ν_v	momentum scattering frequency given by $\nu_v = \nu_\varepsilon + \nu_{el}$
NDC	negative differential conductivity
p	electron momentum in z-direction
ψ	electron wave function
Q	reciprocal vector $2\pi/d$ of the superlattice
r	relative change of the electric field in the superlattice
σ_0	conductivity j_d/E_0
σ_d	differential conductivity $\partial j_d/\partial E_0$
σ_ω	high-frequency conductivity j_ω/E_1
t_{tr}	transit time of a domain
t_f	time of formation of a domain
T	time of one period of an external field
τ	scattering time
τ_c	differential relaxation time
τ_ε	inelastic scattering time
τ_{el}	elastic scattering time
U_0	DC voltage amplitude
U_1	AC voltage amplitude
U_c	critical voltage for a superlattice given by $U_c = E_c L$
v_d	drift velocity in a static homogeneous system with applied field
v_ω	high-frequency component of the velocity
V_b	potential height in the barrier
w	well width in the superlattice
ω	angular frequency $2\pi f$
ω_B	Bloch frequency, defined by $\omega_B = eEd/\hbar$
ω_c	growth velocity of inhomogeneities $\sigma_d/\epsilon\epsilon_0$
ω_n	eigenfrequencies of a cavity
z	superlattice periodicity direction

Introduction

In this thesis the transport properties of semiconductor superlattices are studied using a semiclassical model of electron dynamics. Since their first proposal more than thirty years ago by Esaki and Tsu [Esa70] semiconductor superlattices have been the subject of intense research. In the superlattices a one-dimensional periodic potential is created by a periodic variation of semiconductor materials in one spatial direction.

The implications of a periodic structure on the electronic states are well known [Bloch28] from the theory of conventional crystal structures exhibiting a periodic potential. The so-called *Bloch states* occupy certain intervals in the energy spectrum, the *bands*, while other energy values are forbidden. The states are characterized by a quasimomentum $\hbar\mathbf{k}$ and a band index ν. Bloch demonstrated that a wave packet created by a superposition of momentum space states centered around some quasimomentum $\hbar\mathbf{k}$ moves with a group velocity given by the gradient of the energy with respect to the quasimomentum $\hbar\mathbf{k}$. If an electric field is applied the Bloch vector of the electron becomes time-dependent according to the acceleration theorem

$$\hbar\frac{d\mathbf{k}}{dt} = e\mathbf{E}$$

where $-e$ is the electron charge and the electric field $\mathbf{E}$ points into the direction in which electrons are accelerated (opposite to the usual definition). In a repeated zone scheme the quasimomentum of the electron moves uniformly through the Brillouin zone within one band if a homogeneous and static electric field is applied. Neglecting interband tunneling and scattering processes, the electron returns repeatedly to its original position in momentum space, causing a periodic motion both in momentum and real space, the *Bloch oscillation*.

This effect leads to a reduction and ultimately to the disappearance of transport for increasing electric fields. However, this counterintuitive effect could never be observed for crystals with a lattice period a of atomic distances. The electric field necessary to drive the electrons once or even several times through the Brillouin zone, before a scattering event changes the quasimomentum, cannot be sustained by the crystals.

This restriction can be circumvented in superlattices. The periodicity length d is much larger than the crystal lattice constant a leading to a reduction of the

size of the Brillouin zone by the factor d/a. The width of the allowed regions in energy space will be much smaller as well, hence the bands are called minibands. It is now possible for the electrons to cross the Brillouin zone at attainable fields. The field necessary to drive the electrons through the Brillouin zone before they are scattered is called the critical field E_c. Increasing the field strength further the electrons start to oscillate at the *Bloch frequency* with the transport being reduced, resulting in a negative differential conductivity (NDC). This property could "lead to new ultra-high-speed devices", as Esaki and Tsu put it, which makes the system interesting for technical applications. The electrons oscillate at typical frequencies of several Terahertz, a frequency region where a room temperature solid state radiation source is still lacking. But more than thirty years after the proposition no device emitting radiation in the Terahertz regime has been designed, despite ongoing research activities. One of the main problems is the instability of the superlattices in the NDC regime.

It is not possible to apply a homogeneous electric field in an NDC material since density fluctuations inside the material tend to grow with time, destroying homogeneity. Depletion layers, accumulation layers, or a combination of both, the so-called dipole domains, form inside the superlattice or at the boundaries. The importance of inhomogeneities and boundaries for the behavior in NDC materials was recognized already in the late 1960's when Kroemer and others investigated the Gunn effect in GaAs [Kro68]. Depending on the boundary conditions the charged layers can be static or they travel through the superlattice. If they are created at the cathode and annihilated at the anode after traveling through the material, oscillating behavior with a fixed frequency is observed. This mechanism is used in a conventional Gunn oscillators and was also used in superlattices to create radiation up to frequencies of more than one hundred Gigahertz [Sch99a, Sch99b]. Yet, it is questionable whether it is possible to enter the Terahertz regime with this mechanism.

In contrast to the Gunn-like oscillations where the inhomogeneities are desirable for the creation of microwave radiation, a homogeneous or almost homogeneous situation is required to use the Bloch oscillations directly for microwave generation. It was shown shortly after the proposal by Esaki and Tsu that high-frequency gain up to the Bloch frequency can be found in materials exhibiting Bloch oscillations [Kti72]. In this treatment and many of the following investigations the authors rely on the assumption of a homogeneous electric field inside the superlattice without a clear conception of how this can be achieved in reality due to the problem of inhomogeneities. Several mechanisms have recently been proposed to avoid the undesirable inhomogeneities in the superlattices, like reducing the dimensionality of the system [Fei04], reducing the superlattice length [Sav04], irradiating with high-frequency radiation [Kro00a], or injecting hot electrons into the superlattice [Ryn03]. In all cases the authors "have not touched at all on what is possibly the most severe unsolved problem, the contact boundary prob-

lem", as one of the authors concludes [Kro00a]. The only theoretical treatments known to me which include the boundaries in their considerations rely on the drift-diffusion-model [Sch02b, Bon03], the applicability of which is questionable for high-frequency simulations.

In this thesis I study semiclassical equations to model the transport in semiconductor superlattices including the boundary regions.

Chapter 1 reviews basic properties of semiconductor superlattices and introduces concepts that were invented in the late 1960's when a lot of research was done to understand the Gunn effect. Already back then Kroemer pointed out that the boundary conditions are crucial for the behavior of the devices. Some of the results are summarized here since they also apply to the semiconductor superlattices. One new mechanism to suppress domains, proposed by Kroemer, is reviewed and a connection to an old proposal for Gunn diodes established.

In **Chapter 2** the semiclassical Boltzmann equation is put into a form which is suitable for numerical treatment. The boundary conditions can be formulated easily for this equation. It can be further simplified under certain conditions to end up with the moment-balance equations and finally with the drift-diffusion model. Smooth and abrupt transitions from the bulk material to the superlattice are considered and boundary conditions derived. For the abrupt transitions tunneling processes are also considered. Finally models for the current circuit and a surrounding cavity are developed.

Chapter 3 presents results of the calculations. The chapter is split into two parts: First, the boundaries are neglected and a system with periodic boundary conditions is investigated to see which effects can be observed without the additional features introduced by the boundaries. This model is already an extension of the usual homogeneous models since the formation of domains is possible. The numerical results of the different semiclassical approaches developed in Chapter 2 are compared and the behavior under external radiation is analyzed with the Boltzmann equation. In the second part, the boundaries are included in the description. Measured current-voltage characteristics are compared with the calculated curves and the high-frequency properties are investigated. While some features of the measurements can be explained with the developed model, it turns out that the inclusion of the surrounding of the superlattice into the simulation procedure would be necessary to fully explain the measurements.

The thesis closes with a **Summary** and an **Outlook**.

Chapter 1

Semiconductor superlattices and Gunn diodes

This chapter is a short introduction into the physics of semiconductor superlattices and the transport properties of Gunn diodes. I will focus on the miniband description of superlattice transport which is a valid description for wide minibands. A broader coverage on superlattices can be found e. g. in the book by Bastard [Bas96] or the review by Wacker [Wac02]. An overview over Gunn diode physics is given in the book by Shur [Shu86].

1.1 Miniband structure in semiconductor superlattices

In this thesis superlattices will be considered which are designed as periodic structures with periodicity constant d built by the deposition of alternating layers of two materials with similar lattice constants, like Galliumarsenide (GaAs) and Aluminumarsenide (AlAs) (Fig. 1.1a). The structures are assumed to be translationally invariant within the x- and y-directions perpendicular to the growth direction.

In the growth direction the electrons experience alternating layers of different semiconductor material. The conduction band edge has a steplike structure in this direction (Fig. 1.1b). The conduction band edge in the GaAs layers lies 1.06 eV lower than in the AlAs layers, therefore the GaAs layers form wells, while the AlAs layers form barriers. I start the discussion of the electronic properties with a short review of the Kronig-Penney model [Kro31].

Kronig and Penney assumed a particle subject to a one-dimensional potential as shown in Fig. 1.2 which can be considered as an infinite sequence of barriers and wells. Given a particle energy ε such that $0 < \varepsilon < V_b$ one can make an ansatz of

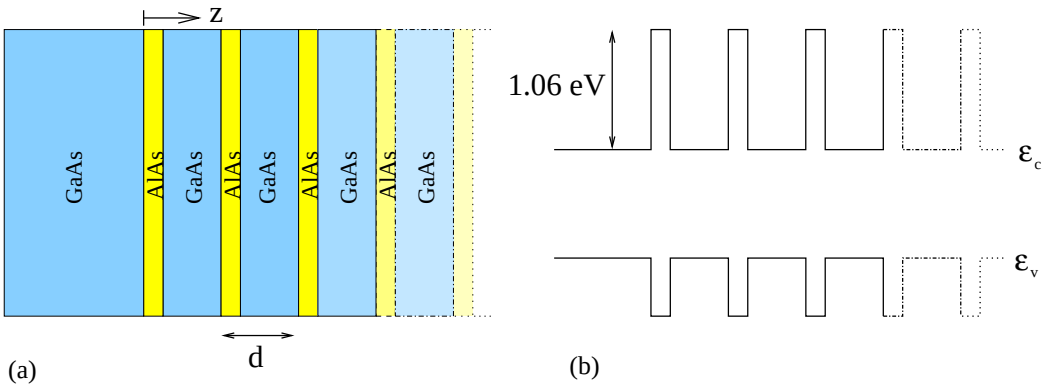

Fig. 1.1: *(a) Alternating layers of semiconductor material are deposited, building an artificial periodic structure with periodicity d. The number of periods ranges from 15 to 150 in the experiments. (b) The conduction band edge (ε_c) and the valence band edge (ε_v) have a steplike spatial dependence inside the superlattice.*

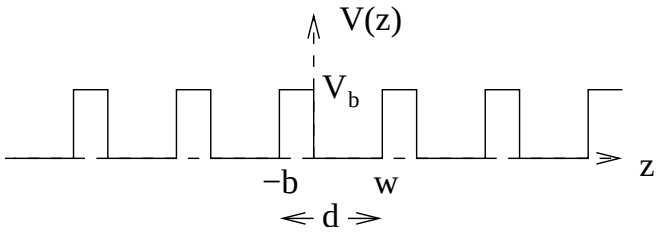

Fig. 1.2: *The potential profile investigated by Kronig and Penney [Kro31].*

plane waves inside the wells ($0 < z < w$)

$$\psi(z) = A\exp(ik_w z) + B\exp(-ik_w z) \quad \text{with} \quad \varepsilon = \frac{\hbar^2 k_w^2}{2m_w^\star} \tag{1.1}$$

and decaying wave functions in the barriers ($-b < z < 0$)

$$\psi(z) = C\exp(\kappa_b z) + D\exp(-\kappa_b z) \quad \text{with} \quad V_b - \varepsilon = \frac{\hbar^2 \kappa_b^2}{2m_b^\star} \tag{1.2}$$

with equal effective masses in the well and the barrier. It was shown by Bloch [Bloch28] short before the paper by Zener that solutions to the problem of a particle in a periodic potential of extension L (being much larger than the periodicity length) must be of the form $\psi(z) = u(z)exp(ikz)$ ($k = 2\pi n/L$) where $u(z)$ is a periodic function in z with the same periodicity d as the potential and n is any integer. The constants A, B, C, and D have to be chosen such that the function ψ at the boundaries between well and barrier obeys the connection rules

$$\psi(z)|_{z\to 0^-} = \psi(z)|_{z\to 0^+}, \quad \psi'(z)|_{z\to 0^-} = \psi'(z)|_{z\to 0^+} \tag{1.3}$$

and

$$\psi(z)|_{z\to w^-} = e^{ikd}\psi(z)|_{z\to -b^+}, \quad \psi'(z)|_{z\to w^-} = e^{ikd}\,\psi'(z)|_{z\to -b^+}\ . \tag{1.4}$$

Nontrivial solutions for A, B, C, and D can be found, if

$$\cos(kd) = \cosh(\kappa_b b)\cos(k_w w) + \frac{1}{2}\left(\xi - \frac{1}{\xi}\right)\sinh(\kappa_b b)\sin(k_w w) \tag{1.5}$$

with the parameter

$$\xi = \frac{\kappa_b}{k_w}\ . \tag{1.6}$$

If the absolute value of the right-hand side of Eq. (1.5) is larger than one the corresponding electron energy is forbidden. These gaps separate regions of allowed energy values, the minibands.

In contrast to the original paper where free particles were considered, the approach must be slightly generalized for semiconductor heterostructures. Using the envelope function method [Bas96], the model for the heterostructures can be reduced to a Kronig-Penney model where the effective masses in the well m_w^* and in the barrier m_b^* are different. The boundary conditions at the interfaces for the derivative of ψ are generalized to

$$\frac{1}{m_b^*}\,\psi'(z)|_{z\to 0^-} = \frac{1}{m_w^*}\,\psi'(z)|_{z\to 0^+}\,, \quad \frac{1}{m_b^*}\,\psi'(z)|_{z\to b^-} = e^{ikd}\frac{1}{m_w^*}\,\psi'(z)|_{z\to w^+}\ . \tag{1.7}$$

Eq. (1.5) is still valid [Ivc97, Bas96], but ξ is replaced by

$$\tilde{\xi} = \frac{\kappa_b m_w^*}{k_w m_b^*} = \sqrt{\frac{(V_b-\varepsilon)m_w^*}{\varepsilon m_b^*}} \tag{1.8}$$

which differs from the definition of ξ above by the mass term ratio introduced by the condition for the derivation[1]. Equation (1.5) can be solved numerically for the dispersion relation in the miniband. As a concrete example a GaAs/AlAs superlattice is now considered (Tab. 1.1). The dispersion relation of the lowest two minibands are shown as solid lines in Fig. 1.3a and b. In GaAs and AlAs the effective masses $m_w^\star = 0.067\ m_e$ and $m_b^\star = 0.11\ m_e$ were chosen.

Denoting the right-hand side of Eq. (1.5) as $f(\varepsilon)$ and expanding it around the energy eigenvalue ε_j of an isolated well (which is allowed for narrow minibands) the equation becomes

$$\cos(kd) = f(\varepsilon_j) + f'(\varepsilon_j)(\varepsilon - \varepsilon_j) \tag{1.9}$$

[1] Note the different signs in [Bas96] in Eq.(89), page 21, and Eq.(79), page 90, which is due to a redefinition of $\tilde{\xi}$, that is not explicitly stated.

	material	width	band-gap	band offset	doping	length
well	GaAs	4 nm	1.52 eV	1.06 eV	$8 \times 10^{16}\mathrm{cm}^{-3}$	100 d
barrier	AlAs	1 nm	3.13 eV			

Tab. 1.1: *Parameters for a GaAs/AlAs superlattice typical for the superlattices used in [Sch98b]. The material parameters are taken from [Wac02].*

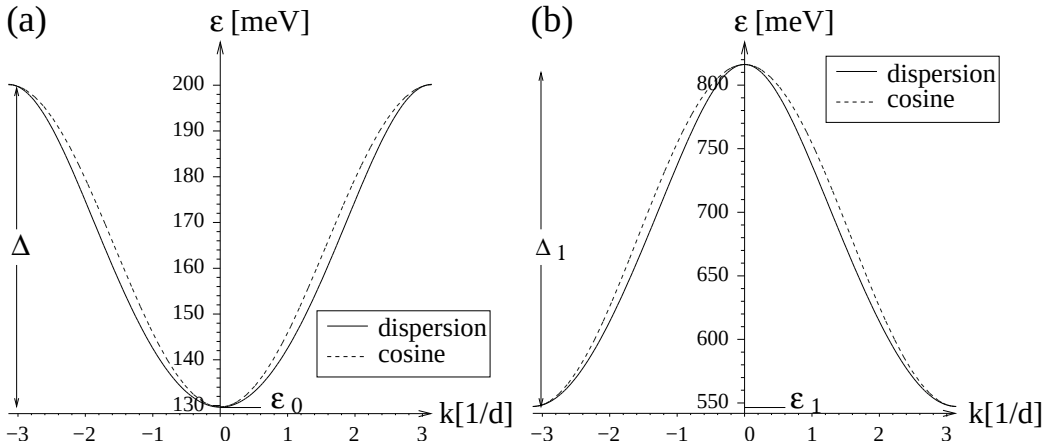

Fig. 1.3: *The miniband dispersion relation for the lowest (a) and the second miniband (b) that follow from Eq. (1.5) (solid lines) for the superlattice parameters of Tab. 1.1. For comparison a cosine function with the same bandwidth (Δ and Δ_1 resp.) and band edge (ε and ε_1 resp.) is shown in both graphs (dashed lines).*

which can be solved for ε

$$\varepsilon = \varepsilon_j - f(\varepsilon_j)/f'(\varepsilon_j) + 1/f'(\varepsilon_j)\cos(kd) \; . \tag{1.10}$$

This shows that a cosine dispersion is a good approximation for narrow minibands. For typical superlattices the approximation of the dispersion by a cosine is also a good approximation for rather wide minibands as a comparison with cosine functions with the same bandwidth and band edge (Figs. 1.3a and b) shows. Very often the miniband dispersions are therefore approximated by a cosine function with the bandwidth Δ and band edge ε_0 that can be derived from the dispersion relation obtained from Eq. (1.5). For the lowest miniband write

$$\varepsilon(k) \approx \varepsilon_0 - \frac{\Delta}{2}\left(1 - \cos(kd)\right) \; . \tag{1.11}$$

Up to now only the growth direction has been taken into account. If the variation of the superlattice perpendicular to the growth direction can be neglected, a complete set of eigenstates can be constructed by products of plane waves $e^{i\mathbf{k}_\perp \cdot \mathbf{r}_\perp}/2\pi$

and a z-dependent function $\psi(z)$. The total energy of the electron is then given by

$$\varepsilon_{tot}(\mathbf{k}) \approx \varepsilon_0 - \frac{\Delta}{2}\left(1 - \cos(kd)\right) + \frac{\hbar^2 k_\perp^2}{2m_w^*} \,. \tag{1.12}$$

Here the effective mass of the well m_w^* is used for the dispersion in the perpendicular direction since the absolute value of the wave function will be larger in the wells. In the next section the implications of a cosine dispersion in a material with scattering time large enough so that a crossing of the Brillouin zone is possible will be explored.

1.2 Esaki-Tsu model

To get a first idea about the behavior of electrons in superlattices it is useful to go back to the model used by Esaki and Tsu [Esa70]. They considered one electron with a cosine dispersion relation that moves under the influence of an electric field E in z-direction. According to Bloch [Bloch28] the quasimomentum changes as

$$\hbar\frac{dk}{dt} = eE \tag{1.13}$$

where k is the quasimomentum in this direction. This can be integrated to give

$$k(t) = \frac{eEt}{\hbar} \tag{1.14}$$

for a constant electric field E. The velocity for an electron that starts at the Brillouin zone center at time $t = 0$ follows from Eq. (1.11)

$$v(t) = \frac{1}{\hbar}\frac{\partial\varepsilon}{\partial k} = \frac{\Delta d}{2\hbar}\sin(kd) =: v_0\sin(\omega_B t) \tag{1.15}$$

where the Bloch frequency

$$\omega_B = \frac{eEd}{\hbar} \tag{1.16}$$

has been introduced. Assuming that the probability that the electron travels a time t without scattering is $p(t) = exp(-t/\tau)$, where τ is the average scattering time, the average velocity of the electron is

$$v_d(E) = \frac{1}{\tau}\int_0^\infty p(t')v(t')dt' = v_0\frac{E/E_c}{1 + (E/E_c)^2} \tag{1.17}$$

where the critical field $E_c = \hbar/ed\tau = \hbar\nu/ed$ has been introduced. For simplicity in this model each scattering event scatters the electron back to the Brillouin zone center. In Fig. 1.4 the resulting v_d-E curve is depicted with an intuitive

explanation for different field strengths. For small electric fields $E < E_c$ the electrons never leave the parabolic part of the dispersion relation resulting in a linear drift velocity versus field relation. For fields $E \geq E_c$ the electron enters a region where the velocity starts to drop. The v_d-E curve passes a maximum. Increasing the field further the electron reaches a region with negative velocity, reducing the drift velocity, until for very large fields the electron spends an equal amount of time in regions with positive and negative velocities and the drift velocity drops to zero for $E \to \infty$.

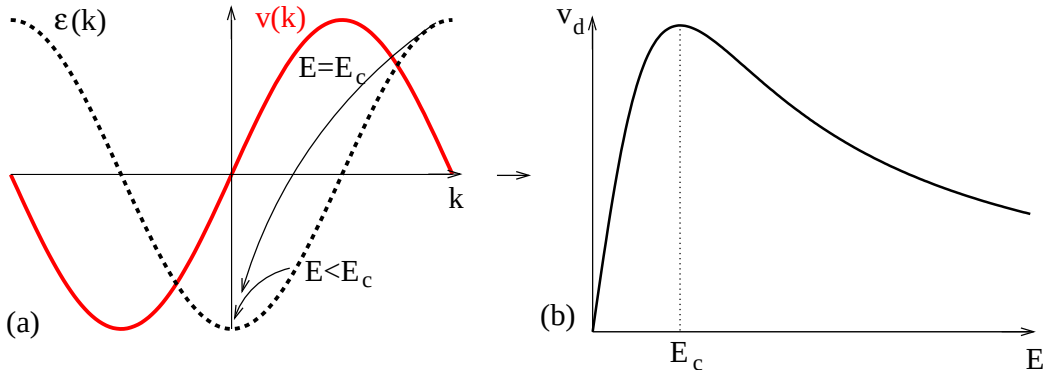

Fig. 1.4: *The cosine dispersion and the velocity of an electron in the lowest miniband (a) and the resulting drift velocity v_d as a function of E (b). For $E < E_c$ the electron is scattered to the Brillouin zone center before it leaves the parabolic part of the dispersion. The v_d-E characteristic is linear in this regime. For $E \geq E_c$ the electron reaches a Brillouin zone region where the velocity becomes smaller before it is scattered. The v_d-E curve passes a maximum. For electric fields $E > E_c$ the electron enters the region with negative velocity reducing the average velocity.*

Before that happens interband transitions will of course start to be important rendering the model invalid in this limiting case. In the next section the simple Esaki-Tsu model will be extended to the case of an electron ensemble.

1.3 Ktitorov model

There are two restrictions in the Esaki-Tsu model: every time the electron is scattered it returns to the Brillouin zone center and no elastic scattering events are included. Both restrictions can be lifted if one uses the equation

$$\frac{\partial f}{\partial t} + \frac{eE}{\hbar}\frac{\partial f}{\partial k} = -\frac{1}{\tau_\varepsilon}\left(f(k) - f_0(k)\right) - \frac{1}{\tau_{el}}\frac{1}{2}\left(f(k) - f(-k)\right) \tag{1.18}$$

which describes the time evolution of an electron distribution $f(k,t)$ in k-space. The equation is derived in Appendix B from the Boltzmann equation. The first term on the right-hand side describes the relaxation towards an equilibrium distribution f_0, while the second describes elastic scattering events. This model for superlattice transport was first introduced in 1972 by Ktitorov *et al.* [Kti72] and has been used extensively subsequently [Ign76, Ign83, Ign91, Ign95]. It extends the Esaki-Tsu model to the case of an electron ensemble $f(k)$ instead of one electron and includes elastic scattering events. If one used $f_0(k) \propto \delta(k)$, the electrons would scatter to the Brillouin zone center at each scattering event and neglecting additionally the elastic scattering one would return to the Esaki-Tsu model. It will be shown that the results of the last section for the drift velocity versus field relation are qualitatively the same with this model.

1.3.1 Static conductivity

To obtain the results of Ktitorov *et al.* I will use the moment-balance equation approach, obtaining the same results for static and high-frequency conductivity that the authors obtained using a Green function method. We define the averages

$$\langle v\rangle = \frac{1}{n}\int f(k)v(k)dk \quad \text{and} \quad \langle \varepsilon\rangle = \frac{1}{n}\int f(k)\tilde{\varepsilon}(k)dk \tag{1.19}$$

where $\tilde{\varepsilon} = \varepsilon - \Delta/2$ is the energy measured from the middle of the miniband. With those definitions we find the following moment-balance equations from Eq. (1.18)

$$\frac{\partial\langle v\rangle}{\partial t} + \frac{eEd^2}{\hbar^2}\langle\varepsilon\rangle = -\underbrace{(\nu_{el}+\nu_\varepsilon)}_{\nu_v}\langle v\rangle \tag{1.20}$$

$$\frac{\partial\langle v\rangle}{\partial t} - eEv_d = -\nu_\varepsilon(\langle\varepsilon\rangle - \varepsilon_T) \tag{1.21}$$

where the scattering frequencies $\nu_{el} = 1/\tau_{el}$ and $\nu_\varepsilon = 1/\tau_\varepsilon$ have been introduced.

$$\varepsilon_T = \frac{1}{n}\int f_0(k)\tilde{\varepsilon}(k)dk = -\frac{\Delta}{2}\frac{\mathcal{I}_1}{\mathcal{I}_0} \tag{1.22}$$

is the average energy of the equilibrium distribution, which is always negative measured from the middle of the miniband and we define $\mathcal{I}_n := \int \cos(nkd)f_0(k)dk$.

We denote the average velocity and energy for static applied field by v_d and ε_d in the following. The Eqs. (1.20) can then be solved to give

$$v_d = v_0\delta^{1/2}\frac{\mathcal{I}_1}{\mathcal{I}_0}\frac{E/E_c^{ET}}{1+(E/E_c^{ET})^2} \tag{1.23}$$

where $E_c^{ET} = \hbar\sqrt{\nu_\varepsilon \nu_v}/ed$ generalizes the definition from the last section and $\delta = \nu_\varepsilon/\nu_v$. If $f_0(k) \propto \delta(k)$ then $\mathcal{I}_1 = \mathcal{I}_0$ and assuming additionally $\nu_{el} = 0$, one recovers equation (1.17) from the Esaki-Tsu model, as could be expected. While the shape of the v_d-E relation stays the same as in Fig. 1.4b one can separate the effects of the distribution function and the elastic scattering. The term $\mathcal{I}_1/\mathcal{I}_0$ originates in the equilibrium distribution function and has a maximum of one for the δ-distribution considered before. For any other distribution the average velocity will be suppressed, e. g. for a Maxwellian distribution $f_0(k) \propto \exp(\beta\Delta/2\cos(kd))$ one gets $\mathcal{I}_1/\mathcal{I}_0 = I_1/I_0$, where I_m are the modified Bessel functions with argument[2] $\beta\Delta/2 = \Delta/2k_BT$.

Since $\delta < 1$, the elastic scattering also reduces the average velocity. This can be understood by the fact that elastic scattering events tend to distribute the electrons homogeneously in k-space and a homogeneous distribution in k-space carries no current. The peak velocity $v_p = \frac{v_0}{2}\delta^{1/2}\frac{\mathcal{I}_1}{\mathcal{I}_0}$ is reached if the electric field $E = E_c^{ET}$. Since $v_p \propto \sqrt{\nu_\varepsilon/\nu_v}$ and $E_c^{ET} \propto \sqrt{\nu_\varepsilon \nu_v}$ are accessible in the experiment, one can determine ν_v and ν_ε by a measurement of both quantities [Sch98b], assuming that Eq. (1.18) describes the superlattices correctly.

1.3.2 High-frequency conductivity

In addition, Ktitorov *et al.* have investigated the high-frequency conductivity with Eq. (1.18). Again the moment-balance equations will be used to derive the result. We consider the case of a small high-frequency electric field that is applied in addition to the static field

$$E_{tot} = E_0 + E_1 e^{-i\omega t} \,. \tag{1.24}$$

The average velocity and energy will have small components added to the static values oscillating with this frequency

$$v_{tot} = v_d + v_\omega e^{-i\omega t} \quad \text{and} \quad \varepsilon_{tot} = \varepsilon_d + \varepsilon_\omega e^{-i\omega t} \,. \tag{1.25}$$

Inserting these equations into Eqs. (1.20,1.21) and neglecting products of the small oscillating quantities we get

$$v_\omega = \frac{1 - i\omega\tau_\varepsilon - (E_0/E_c^{ET})^2}{(1 - i\omega\tau_v)(1 - i\omega\tau_\varepsilon) + (E_0/E_c^{ET})^2} \frac{v_d}{E_0} E_1 \,. \tag{1.26}$$

From this equation the high-frequency conductivity

$$\sigma_\omega = \frac{1 - i\omega\tau_\varepsilon - (E_0/E_c^{ET})^2}{(1 - i\omega\tau_v)(1 - i\omega\tau_\varepsilon) + (E_0/E_c^{ET})^2} \sigma_0 \tag{1.27}$$

[2] In the following the argument of the modified Bessel functions I_m will always be $\beta\Delta/2 = \Delta/2k_BT$

can be calculated, where the static conductivity $\sigma_0 = j_d/E_0 = env_d/E_0$ has been defined. The real part of the high-frequency conductivity is depicted in Fig. 1.5 for $E_0/E_c^{ET} = \omega_B\sqrt{\tau_v\tau_\varepsilon} = 2$ and $\tau_v = \nu_v^{-1} = \tau_\varepsilon$.

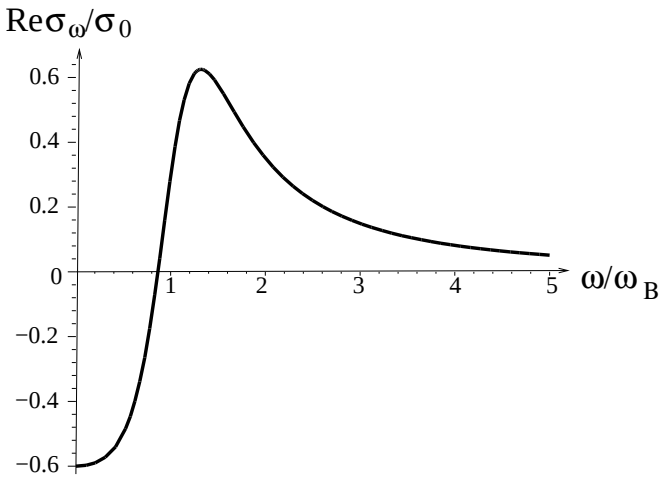

Fig. 1.5: *The real part of the high-frequency conductivity measured in units of $\sigma_0 = j_d/E_0$ as a function of the applied frequency ω in units of the Bloch frequency $\omega_B = eEd/\hbar$ for a static applied field $E_0 = 2E_c^{ET}$ and $\tau_v = \tau_\varepsilon$. It is negative almost up to the Bloch frequency.*

In the limit $\omega \to 0$ we get

$$\sigma_\omega \to \sigma_d = \frac{\partial j_d(E_0)}{\partial E_0} = \sigma_0 \frac{1-(E_0/E_c^{ET})^2}{1+(E_0/E_c^{ET})^2}\,. \tag{1.28}$$

For $E_0 > E_c^{ET}$ the static differential conductivity ($\omega \to 0$) is negative as has already been explained in section 1.2, and the low-frequency differential conductivity is also negative. This can be easily explained by the following considerations. For increasing field the current decreases and for decreasing field the current increases and therefore an applied low-frequency field will be enhanced. The main question is up to which frequency this gain will survive, i. e. up to which frequency ω the relation $\mathrm{Re}(\sigma_\omega) < 0$ holds. From equation (1.27) one can find the frequency where the real part of the differential conductivity crosses zero as

$$\omega_{\sigma_\omega=0} = \sqrt{\frac{(E_0/E_c^{ET})^4-1}{(E_0/E_c^{ET})^2\tau_v\tau_\varepsilon+\tau_\varepsilon^2}} \approx \omega_B\sqrt{\frac{1}{1+\frac{1}{\omega_B^2\tau_v^2}}} \tag{1.29}$$

where the last approximation is valid for $E_0 > E_c^{ET}$. The high-frequency differential conductivity stays negative nearly up to the Bloch frequency ω_B in this case. Radiation up to the Bloch frequency will therefore be enhanced. This is usually referred to as *Bloch gain*. Kroemer [Kro00b] has explained this phenomenon via

the creation of bunches of electrons in k-space. If the superlattice is put into a resonator, the device will start to oscillate if the losses through dissipation are smaller than the gain through the negative high-frequency conductivity at the resonator frequency.

Even more than thirty years after the insight that gain up to the Bloch frequency, which is in the Terahertz regime in usual superlattices, exists in superlattices nobody has succeeded in making a device that really emits radiation in this regime, despite ongoing effort all over the world. The reason are instabilities in the superlattices which tend to destroy the homogeneity that was assumed to subsist in all the derivations up to now. The next section will deal with those instabilities.

1.4 Instabilities in negative differential conductivity (NDC) materials

One can see from Eq. (1.23) and Fig. (1.4)b that the differential conductivity $\sigma_d = \partial j_d / \partial E_0$ is negative above some critical field value E_c. B. F. Ridley predicted in 1963 that an instability should occur in a semiconductor sample with voltage-controlled negative differential conductivity [Rid63]. It was realized already shortly before, that the velocity in n-type GaAs and some other compounds should decrease with electric field if the electric field exceeds a critical value inducing the intervalley transition from the high mobility Γ-valley to higher minima with higher effective mass and scattering rate [Rid61, Hil62]. And indeed, J. B. Gunn discovered in 1963 spontaneous current oscillations in GaAs when the applied electric field E was greater than some critical value E_c [Gun63]. Kroemer pointed out that all important features of the Gunn effect are consistent with the model of instabilities originating in the negative differential conductivity [Kro64].

An abundance of phenomena was discovered in the semiconductor compounds exhibiting NDC afterwards, and many theoretical investigations followed to explain the observations. All phenomena can be traced back to the NDC characteristic which is also present in the semiconductor superlattices. In the following I will review the results of the investigations on the Gunn effect which can be carried over with minor modifications to the superlattices.

1.4.1 Bulk instabilities

Spatially homogeneous states with a negative differential conductivity cannot be stable under experimental conditions. The system goes over to a strongly

inhomogeneous state. This can be understood by noting that a spatially homogeneous system is meaningful only as a time-average: instantaneous values of the carrier density and other physical quantities undergo fluctuations. Under thermodynamic equilibrium conditions these fluctuations are rapidly damped out. However, in the falling branch of the drift velocity versus field relation the differential conductivity σ_d as well as the damping constant change their signs, and small fluctuations may grow instead of decaying. Before the situation is analyzed mathematically in more detail the principle of the growth of inhomogeneities will be described.

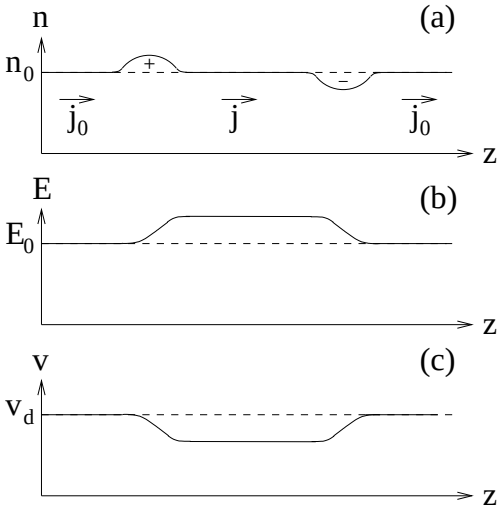

Fig. 1.6: *A small fluctuation of the electric field E (b) and charge density n (a) in a homogeneous sample with negative differential conductivity, leading to a lower drift velocity v_d inside the fluctuation (c). The current density j inside the fluctuation will be smaller than the current density j_0 outside, increasing the charge accumulation and depletion.*

In Fig. 1.6a a fluctuation of the density n along the z-axis is depicted. According to the Poisson equation the distribution of the electric field E will be of the form schematically shown in Fig. 1.6b. Since the differential conductivity is negative, the relative increase of the field inside the fluctuation results in a decrease of the drift velocity v_d (Fig. 1.6c). Thus the current j flowing out of the region with high charge density is less than the current flowing into this region and the accumulation grows and the depletion also grows due to an analogous argument. This process is limited by diffusion which tries to level out the inhomogeneities.

To describe the process on a more mathematical level first extend Eq. (1.18) to the case of spatial dependence

$$\frac{\partial f}{\partial t} + v(k)\frac{\partial f}{\partial z} + \frac{eE}{\hbar}\frac{\partial f}{\partial k} = -\nu\left(f(k) - \frac{n}{n_0}f_0(k)\right) . \tag{1.30}$$

$f(z,k,t)$ is now a function of space also and the ratio of the particle density n and the doping density n_0 has the effect that the distribution relaxes at every point in space to an equilibrium distribution with the local particle density. This ratio also ensures conservation of the particle number since $\int(f(k) - n/n_0 \cdot f_0(k))dk = 0$. As

was shown in the last section the insertion of elastic scattering changes the results only quantitatively and is therefore neglected here. It is shown in Appendix C how one can derive the drift-diffusion model

$$nv = nv_d - D\frac{\partial n}{\partial z} \tag{1.31}$$

from the moment-balance equations which one can get from Eq. (1.30). This derivation is done under the assumption of slow variations in space and time. The diffusion coefficient is assumed to obey the Einstein relation $D/\mu = k_b T/e$ in the following which is a good approximation for slow spatial and temporal changes as is shown in Appendix C.

From this model one can get a first impression of how the instabilities evolve. The evolution of the density given the local particle current nv_d is given by the continuity equation

$$\frac{\partial n}{\partial t} = -\frac{\partial n v_d}{\partial z} \ . \tag{1.32}$$

The electric field which accompanies the inhomogeneities is described by the one-dimensional Poisson equation since the system is still assumed to be homogeneous perpendicular to the z-direction

$$\frac{\partial E}{\partial z} = \frac{e}{\epsilon\epsilon_0}(n - n_0) \ . \tag{1.33}$$

The electric field changes if the electron density n deviates from the positive background charge density n_0 of the ionized donors. Now we make a space-charge wave analysis introducing fluctuations around the stationary solution $n = n_0 + n_k \exp(i(kz - \omega t))$. The electric field is then given by $E = E_0 + E_k \exp(i(kz - \omega t))$ with $ikE_k = \frac{e}{\epsilon\epsilon_0} n_k$ using Eq. (1.33), and the drift velocity is given by $v_d = v_d(E_0) + v_k \exp(i(kz - \omega t))$ with $v_k = \frac{\partial v_d}{\partial E} E_k$. Together with Eqs. (1.32) and (1.31) we get the dispersion relation

$$\omega = k v_d(E_0) - i(Dk^2 + \omega_c) \tag{1.34}$$

where $\omega_c = \sigma_d/\epsilon\epsilon_0$ with the differential conductivity $\sigma_d = \partial j_d/\partial E_0$. This equation describes a convective space-charge wave which propagates with a phase velocity exactly identical to the carrier drift velocity v_d and has an imaginary frequency component $i\omega_2 = -i\,(\omega_c + Dk^2)$ at small wave vector. The equation indicates that when the differential conductivity σ_d is negative then $-\omega_c$ is positive and the waves with long wavelength ($k \to 0$) will grow with time. The shorter the wavelength, i. e. the larger the wavevector k, the stronger the diffusion acts against the growth of the fluctuations. If the system was infinite, it would always be unstable since arbitrary small wavevectors would be possible. The minimum value of k is governed by the length of the sample $k \propto 1/L$, where L is the size

of the sample. For this reason the growth of small fluctuations may not occur in short samples even in the presence of a negative differential conductivity, if $|\omega_c| < Dk^2$. This condition can be written as nL^2-criterion

$$n_0 L^2 < \frac{\epsilon\epsilon_0}{e}\frac{D}{|\mu_d|} \tag{1.35}$$

where $\mu_d = \partial v_d/\partial E_0$ is the differential mobility. In the superlattice from Tab. 1.1 we get $n_0 L^2 = 2\times10^{10}/\mathrm{m}$, while the right-hand side equals $\epsilon\epsilon_0 k_B T/e^2 \approx 2\times10^7/\mathrm{m}$ using the Einstein relation.

But even if the fluctuations grow with time ($|\omega_c| > Dk^2$), the system can be stable if the fluctuations leave the sample before they grow considerably. This is the case if the time to traverse the sample L/v_d is smaller than the differential relaxation time $\tau_c = \omega_c^{-1}$. This equation leads to the so-called *Kroemer criterion*

$$n_0 L < \frac{\epsilon\epsilon_0}{e}\left|\frac{v_d}{\mu_d}\right| . \tag{1.36}$$

A more thorough analysis produces a prefactor of 2.09 on the right-hand side of this equation [Shu86, McC66]. The ratio v_d/μ_d can be calculated for a drift velocity given by Eq. (1.17) and one gets

$$\frac{v_d}{\mu_d} = E_c\frac{E/E_c(1+(E/E_c)^2)}{(1-(E/E_c)^2)} \leq -3.33E_c \quad \text{for} \quad E > E_c . \tag{1.37}$$

Combining Eqs. (1.36,1.37) with the prefactor of 2.09 in Eq. (1.36) we get no domain formation for $n_0 L <\approx 7\epsilon\epsilon_0 E_c/e$. Again we look at the standard superlattice from Tab. 1.1 and get $n_0 L = 4\times10^{17}/\mathrm{m}^2$, while $7\epsilon\epsilon_0 E_c/e \approx 6\times10^{15}/\mathrm{m}^2$. A typical superlattice is therefore not stable, but one can try to match the Kroemer criterion by making the superlattice short or reducing the doping. Indeed in [Sav04] the authors tried to avoid the formation of domains tailoring their superlattices according to this criterion. They did this by reducing the number of periods and the doping by roughly an order of magnitude compared to the standard superlattice. Since the superlattices have to be very short then (≈ 15 periods), they grew a super-superlattice, i. e. they grew many short superlattices interrupted by highly doped buffer regions.

Another approach to avoid the domain formation is to consider two-dimensional systems, i. e. to restrict the free motion to only one direction perpendicular to the growth direction which is possible using the cleaved edge overgrowth method [Pfe90]. We have shown [Fei04] that in this case the growth rate ω_c is reduced by the product of the width of the superlattice in the restricted direction x_0 and the wave vector k

$$\omega_c^{2d} = \omega_c x_0 k \quad \text{with} \quad x_0 k \geq \pi x_0/L . \tag{1.38}$$

In typical samples one has $\pi x_0/L \simeq 0.01$, which means that domain formation is suppressed considerably.

1.4.2 Boundary effects

Even though the finite size of the sample was crucial for the Kroemer criterion to suppress domains, the exact boundary conditions do not play a role for the behavior in the model up to now, one simply assumes that the domains are annihilated at the anode when they reach it. All the domains originated in small fluctuations inside the superlattice that grew due to the negative differential conductivity. But it was already realized in the 1960's, after the observation of negative differential conductivity in GaAs, that very often the boundaries are the nucleation points of the domains.

Injecting cathode - accumulation layers

To make the effect of the boundary conditions apparent I will first describe a model which was used shortly after the discovery of the Gunn effect to understand the observed oscillations [Kro66]. The model is depicted in Fig. 1.7. Between a highly doped cathode and anode the material exhibiting negative differential conductivity (NDC) is located. Fig. 1.7a shows the shape of the Esaki-Tsu drift velocity versus field relation that was already discussed earlier. The doping profile n_0 is shown (Fig. 3.6b). Including diffusion effects some of carriers of the highly doped contacts would diffuse into the low doped region, but this effect is neglected. Applying a bias voltage one needs to specify the boundary conditions for the electric field E.

The electric field is assumed to stay small inside the highly doped cathode. It will be discussed in the next paragraph what happens if that condition is changed. For a static configuration the current j has to be constant so that $en\mu E$ has to be constant. For low bias voltages $U < E_c L$ the mobility μ is constant so that the product nE has to be spatially constant which leads to the density profile n_1 in Fig. 1.7b and electric field E_1 in Fig. 1.7c.

The situation changes dramatically as soon as the bias voltage is high enough so that the electric field E crosses the critical field value E_c. If the state was still stationary, the density profile n_2 and field profile E_2 depicted in Fig. 1.7b and c respectively would result. In Fig. 1.8a the formation process of the accumulation layer, which sets in for $U = U_2 > U_c$, is schematically shown in detail. Diffusion effects will be neglected in this consideration, only a qualitative description of the process is attempted. In the left column the static situation before the electric field crosses the critical field value E_c is depicted. A small increase of the voltage leads to a supercritical field and a small charge accumulation will form where the field value crosses the critical field. This can be seen from the current which drops at the point where the electric field becomes supercritical. The relation $\partial n/\partial t = -\partial nv/\partial x$ shows that the density will rise where $\partial nv/\partial x < 0$ and

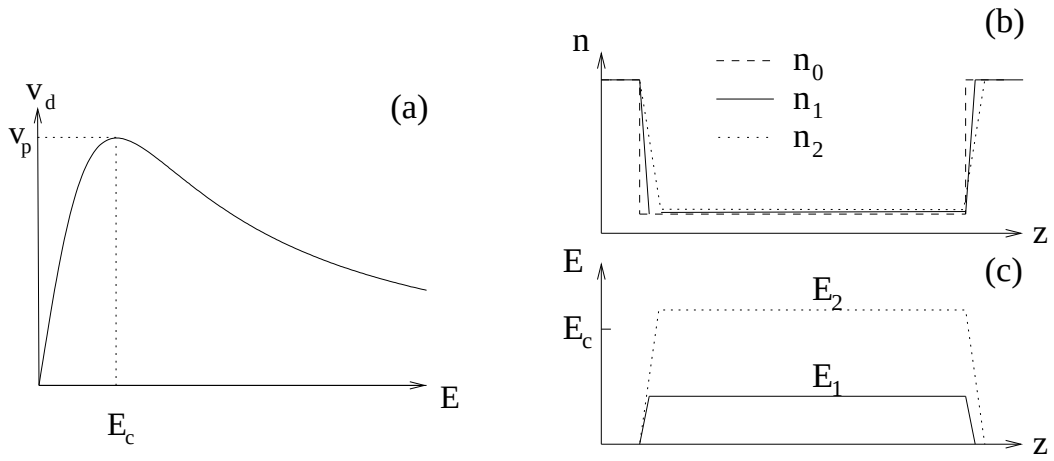

Fig. 1.7: *The drift velocity versus field characteristic inside the superlattice region (a) and the doping profile n_0 and densities (b) and corresponding field distributions (c) for different applied voltages. Assuming a low electric field value in the highly doped contact region, one can easily draw the schematic densities n_1 and n_2 for different applied voltages U_1 and U_2 where diffusion effects are neglected. The corresponding field distributions E_1 and E_2 are shown (c). For $U = U_2$ the situation is unstable as will be shown in Fig. 1.8.*

decrease otherwise, indicated by the small arrows. The charge accumulation will start to travel since the current nv goes through a maximum which leads to a decrease of the density on the left side of the accumulation and to an increase of the density at the right side of the accumulation.

The accumulation layer detaches from the cathode and moves towards the anode (Fig. 1.8b). The electric field value E_a ahead of the layer is supercritical and the field value E_b behind the layer stays subcritical. Since the applied voltage is constant, E_a grows with time and E_b drops with time. This means that the accumulation layer has to grow while it is traveling through the superlattice. Therefore the velocity behind the superlattice $v(E_b)$ has to be a little higher than ahead of the superlattice $v(E_a)$. The processes at the anode, when the accumulation reaches it, are described in detail in a separate paragraph on anode domains below. It will be shown that if the drift velocity versus field relation does not increase for high fields often a static anode domain is formed.

There are some features of the pure accumulation mode that suggested that in the Gunn diode experiments some other mechanism is responsible for the microwave emission [Kro66]. In our numerical calculations for the superlattices it was also difficult to produce oscillations with the pure accumulation mode. Kroemer proposed several mechanisms for Gunn diodes that lead to a breakup

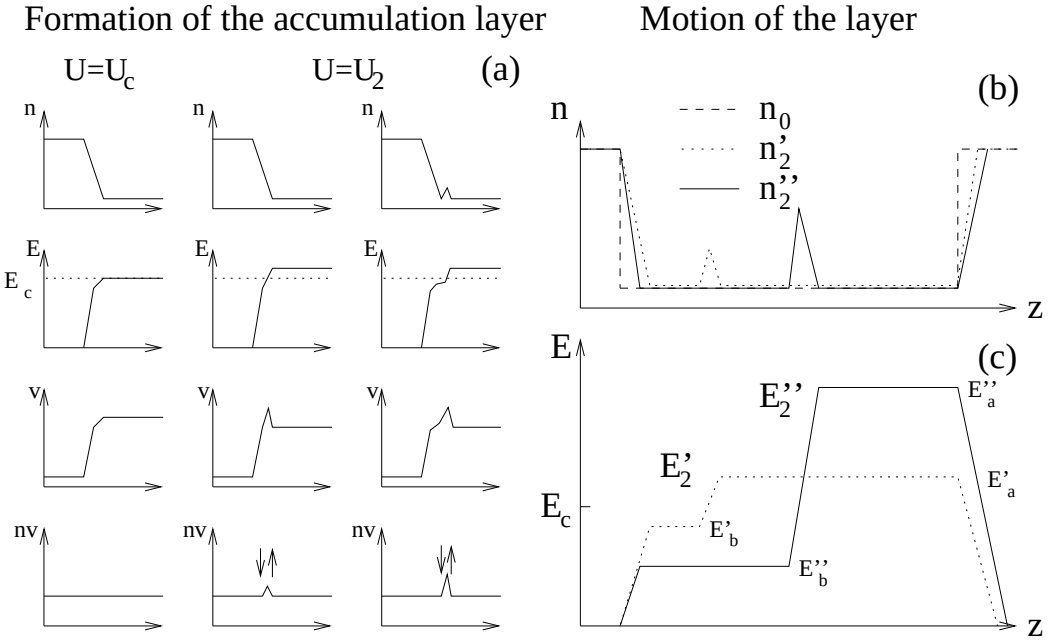

Fig. 1.8: *(a) The details of the formation of the accumulation layer at the cathode contact when the field in the superlattice becomes slightly larger than E_c. (b,c) The resulting overall density and field evolution in the superlattice after the formation. The left pictures show the processes only at the cathode contact. If the voltage is increased so that the field inside the superlattice becomes larger than the critical field E_c, the static situation (left column, $U = U_c$) changes into a non-stationary state (middle and right column, $U = U_2$). The resulting current nv is not spatially constant and the density starts to change indicated by small arrows. Two different density profiles n_2' and n_2'' for the moving layer and the corresponding field values E_2' and E_2'' are shown. E_a and E_b denote the fields ahead of and behind the accumulation layer.*

of the pure accumulation layer mode and resulted in dipole domain behavior. If depletion layers are created via noise or doping fluctuations or at the interfaces, they will merge with the primary accumulation layer to form dipole domains and the results agreed better with the experimental findings.

I will first describe the creation of dipole domains via fluctuations. Many secondary accumulation and depletion layers emerge in the sample in addition to the primary accumulation layer ahead of the accumulation layer since the field E_a is supercritical there. As the strongest of these secondary space-charge layers build up the fields on either side of them move out of the negative mobility range, and any weaker space-charge layer in those regions either collapses or merges with the stronger layer. Depending on the time constant which determines the growth and the drift velocity one depletion layer will survive and merge with the pri-

mary accumulation layer. When the resulting dipole domain reaches the anode the field inside the NDC region rises again and new domains may be formed. On the other hand a static domain can form.

The formation of a new domain is more probable if the electric field at the cathode is high. In addition to the fluctuations Kroemer therefore also proposed another way to produce dipole domains in the models, that is the usage of a limiting cathode which is accompanied by a high cathode field and will be discussed in the next section.

Limiting cathode - depletion layers

In some of the experiments carried out with the Gunn oscillators a behavior was found that could not be explained by the previous model. In those experiments prior to the onset of Gunn oscillations the crystals developed a stationary high-field domain ahead of the cathode for increasing applied voltage. The fields in the cathode fall region were substantially larger than the threshold field E_c. Kroemer [Kro68] developed a model that was perfectly suitable to explain the experiments, even though the microscopic origin of the model is not that clear.

Kroemer abandoned the assumption of a *well-behaved cathode* and introduced the *imperfect cathode* in which a transition to the high field value takes place outside the NDC region. While the control characteristic concept introduced by Kroemer is a little cumbersome to explain, the behavior of the model can be explained by just assuming that the electric field at the cathode is fixed to a value $E_{cath} > E_c$. Fig. 1.9a shows the static situation in the cathode contact region for two different applied voltages. To get a consistent picture it is assumed that the contact region is a low mobility material so that one gets small velocities even for high applied voltages. This is one possibility to achieve the high cathode field E_{cath}. It will become clear in the next chapter that the band-offset can also be responsible for a high contact field.

In contrast to the accumulation layer that develops for a low cathode field a depletion layer develops now and the situation can be static even if the electric field value crosses the critical field value E_c. While for the accumulation layer both the density n and the drift velocity v have a maximum so that nv_d cannot be constant, for a depletion layer the maximum of the drift velocity v_d and the minimum of the density can cancel to get a constant product nv_d as shown in both columns for different applied voltages. The higher the overall bias voltage is the wider to the right the density minimum has to move to accommodate the high overall voltage (Fig. 1.9b). The density between the cathode and the depletion layer gets closer and closer to the equilibrium value n_0 in this process. The part to the left of the depletion layer is in the NDC regime and is unstable

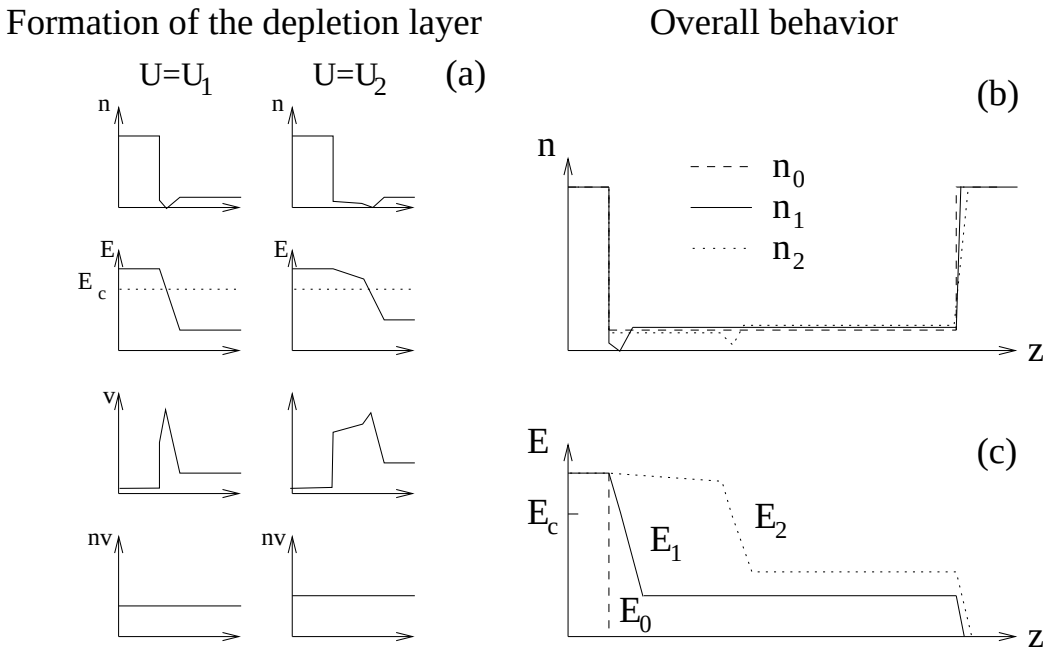

Fig. 1.9: *The formation of the depletion layer for a limiting cathode with rising voltage (a) and the corresponding density (b) and field profiles (c). In contrast to the accumulation layer case there exist static solutions for increasing voltages even when the field is supercritical in a part of the superlattice. For increasing applied voltages U_1 and U_2 the depletion region moves into the superlattice and a larger and larger part of the superlattice is supercritical. As long as the electric field is strictly monotonically decreasing in the supercritical region, i. e. fluctuations are not large enough so that in a small part of the supercritical region the density n is larger than the doping n_0, the situation is stable.*

(Fig. 1.9c). Small depletions will not have a large effect since they drift into the already existing large depletion.

The density is below the doping density so that fluctuations cannot produce regions with accumulations, i. e. $n > n_0$, but for large bias the density is only slightly smaller than the doping density. Accumulations can form if a fluctuation has already grown enough on its way from the origin to the depletion layer so that the additional density is larger than the difference to the doping density. The electric field is then an increasing function of the z-coordinate at that point. It is shown in Fig. 1.10 that an accumulation layer forms if the electric field is not a strictly monotonically decreasing function in the supercritical field region, and the situation ceases to be static.

It is also apparent from the described mechanism that the behavior depends on

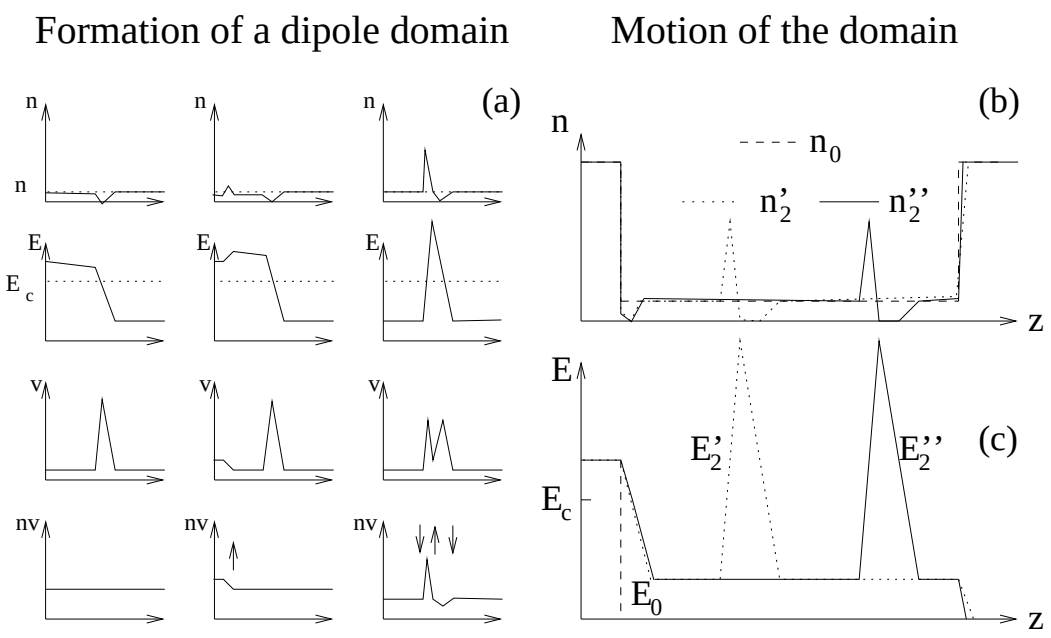

Fig. 1.10: *The formation of a dipole domain from the static depletion layer (a), the electron densities (b) and the field profiles (c) for a moving dipole domain for constant applied voltage. Only the small part of the superlattice where the depletion of Fig. 1.9 is located is shown. In the middle column a fluctuation is inserted which is associated with an increasing field and also increasing density, indicated by the small arrow. The fluctuation grows and it travels towards the depletion where a dipole domain forms (right column). The dipole starts traveling through the superlattice resulting in the density profiles n_2' and n_2'' and corresponding field profiles E_2' and E_2''.*

the size of fluctuations. The mechanism also explains a feature of the simulation results that was a little puzzling when it first appeared. It turned out that the behavior of the device, especially the onset of the oscillating behavior with increasing voltage, depended crucially on the speed of the voltage increase. For certain voltages it was possible to produce oscillating modes if the voltage was suddenly switched on and static situations if the voltage was slowly increased. From the above description it is clear that the static situation, that is in principle possible for some fixed voltage, becomes unstable by the fluctuations introduced due to the sudden voltage switching.

Fig. 1.10a shows the process around the depletion region that starts as soon as a small accumulation layer forms between the depletion and the cathode. The accumulation layer starts to grow and as soon as the electric field value between the accumulation and the cathode becomes subcritical it moves towards the depletion. It merges with the depletion layer and can now travel as a dipole

domain through the crystal at constant voltage. Two different density profiles n_2' and n_2'' and the corresponding field profiles E_2' and E_2'' are shown (Fig. 1.10b and Fig. 1.10c). If the overall bias voltage is not large enough to sustain the fully developed dipole layer $U < U_d + U_D$, where U_D is the voltage drop across a fully developed dipole domain and U_d is the voltage drop at the cathode, the dipole layer collapses on its way to the anode and a new dipole layer is formed. At some bias voltage $U > U_d + U_D$ the dipole domain will finally travel all the way to the anode where first the depletion layer disappears and then the accumulation runs into the anode and the process is repeated.

Up to now the process at the anode has not been discussed. The next section describes this process in more detail and shows that either a standing anode domain or periodic behavior can be observed under suitable conditions.

Anode domains

The standing anode domain was first discovered by Thim *et al.* [Thi67] and he also provided an explanation of the dynamics of the disappearance of charged layers in the anode [Thi71]. Analytical [Gue71] and numerical treatments [Lev79, Kir84] followed, but they only elaborated on the simple mechanism which will be described in the following.

It is not obvious at all that the accumulation layer should move into the anode contact under any circumstances. Let us consider the dashed v_d-E characteristic in Fig. 1.11a which does not increase for large electric field values. It will be shown in the second chapter that indeed for typical superlattice parameters the Zener tunneling probability becomes relevant at field values that are so high that in all practical cases Zener tunneling can be neglected (apart from the superlattice boundaries). In this case the accumulation layer either disappears at the anode or it becomes stationary, depending on the time it takes to readjust. When the accumulation layer starts to travel into the anode the voltage drop over the accumulation starts to drop since only part of the high-field region is left in the superlattice region. Since the total voltage is constant, the field upstream of the accumulation E_a starts to rise. Two different scenarios are now conceivable.

If the process of charge redistribution in the accumulation is too slow, the accumulation will continue moving into the anode, the upstream field E_a rises to E_c leading to the nucleation of a new accumulation. In the presence of this new accumulation layer the upstream velocity of the preceding one is decreasing since the electric field between the two accumulations E_b is supercritical and increasing. Thus not enough electrons move into the old layer to maintain its shape as it moves into the anode and, as a result, it disappears.

A distinctly different phenomenon appears if the charge redistribution process is

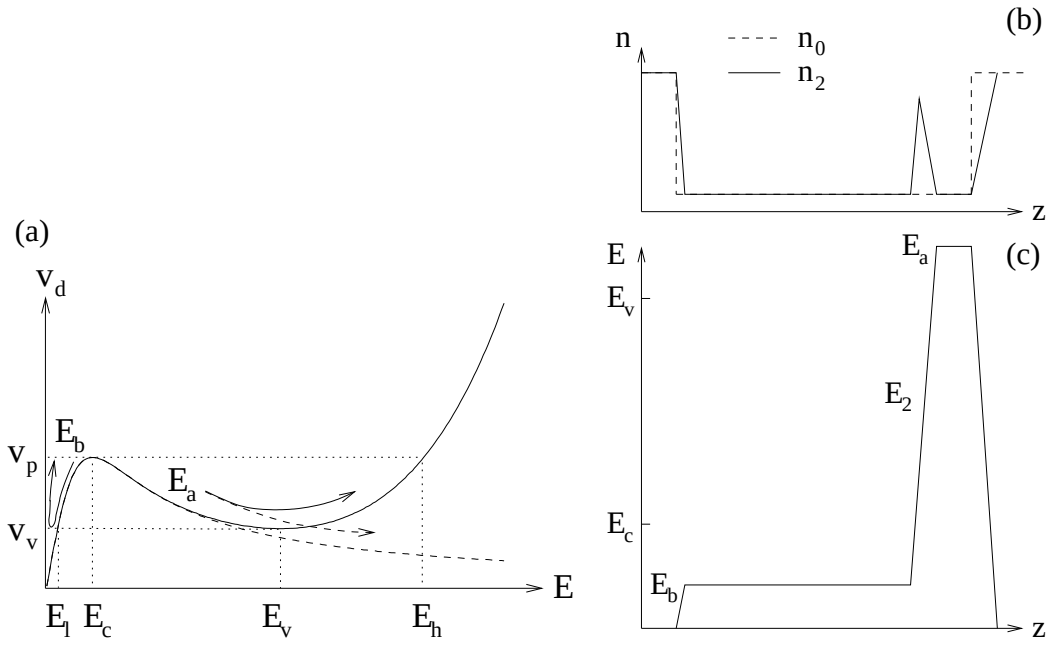

Fig. 1.11: *(a) The drift velocity versus field characteristic and evolution of the electric field value ahead of an accumulation layer (E_a) and behind the accumulation layer (E_b). The Esaki-Tsu characteristic is plotted (dashed line). If one includes a mechanism, e. g. Zener tunneling, that enhances the velocity beyond some field value E_v, the velocity goes through a minimum v_v (solid line). The evolution of E_a depends crucially on whether some process leads to an increase of the drift velocity for high fields. (b,c) The density and field profiles if the accumulation comes close to the anode.*

faster than the accumulation moves into the anode. The rising upstream field E_b pumps more and more electrons into the accumulation. As a consequence of this the accumulation layer approaching the anode does not disappear. Its thickness is determined by diffusion and is assumed to be of the order of several (perhaps two) Debye lengths $l_D = \sqrt{D/\omega_c}$. A mathematical condition for the stationary solution is obtained if the time of readjustment is approximated by the dielectric relaxation time and it is smaller than the time it takes the accumulation to travel into the anode

$$|\omega_c|^{-1} < \frac{2\sqrt{D}}{\sqrt{|\omega_c|}v_d} \tag{1.39}$$

which can be rewritten as $|\omega_c| > v_d^2/4D$ and was found also in an analytical investigation of Eq. (1.34) [Gue71]. For a superlattice with scattering time $\tau = 10^{-13}$s we get a critical density of $n_{cr} = 10^{17}/\mathrm{cm}^3$ using Eq. (1.37). Since in many experiments the doping is on the same order of magnitude, this rough estimate is not sufficient to decide whether the anode domains will be stable in superlattices.

Another mechanism was also proposed which leads to oscillatory behavior. Let us consider the solid v_d-E curve in Fig. 1.11 which rises above some field E_v. As described in the paragraph on accumulation layers the field E_a ahead of the anode rises while the accumulation layer moves through the crystal. The current density $j \propto nv_d$ will go through a minimum for $E = E_v$ and then starts to rise again. The field between the cathode and the layer E_b will first drop to the value E_l and then start to rise again, while the field ahead of the layer E_a only rises so that the current density ahead of and behind the cathode have nearly the same value. As soon as E_b rises to E_c a new accumulation layer is formed at the cathode. The field between the new and the old accumulation layer enters the negative differential mobility section of the v_d-E characteristic, causing the velocity to drop in this range. As a consequence, fewer electrons stream into the old accumulation layer and out of the new accumulation layer. The process continues until the old accumulation layer has vanished and the new accumulation travels through the lattice.

In the numerical simulations Zener tunneling processes were included, but the fields that were necessary for a finite probability of the process was never reached in the calculations. The mechanism relying on the rising current voltage characteristic therefore did not work. The second mechanism of fast moving layers that cannot readjust also did not work. It was therefore only possible to create new dipole domains when the electrical field at the cathode was supercritical. This will be described in detail in Chapter 3.

1.5 Influence of a cavity

Up to now only an applied DC bias voltage has been considered. The influence of a cavity in which the superlattice is situated will be investigated in this section. To get a first impression of the effect of the cavity the influence is simply modeled by an additional AC component of the applied voltage

$$U(t) = U_0 + U_1 \exp(i\omega t) \; . \tag{1.40}$$

In contrast to section 1.4.2 the oscillating component U_1 is now not small compared to the DC component U_0. The n_0L-product of the superlattice is assumed to be large enough so that domains will form (see Eq. (1.36)). Depending on the time of domain transit t_{tr} and domain formation t_f compared to the oscillation period T of the applied voltage one can separate different regimes. t_f depends on the boundary conditions and the superlattice parameters. Here it is just some empirical time.

1.5.1 Delayed and quenched domains

I will first consider only resonance frequencies of the cavity of the order of the inverse transit time $\nu_{tr} \propto 1/t_{tr}$ which will be small compared to the domain formation frequencies $\nu_f \propto 1/t_f$ and which lead to delayed and quenched domain modes. Fig. 1.12 shows the sum of the DC and AC voltage applied to the superlattice structure as a function of time t where the sum of both voltages is sufficient to start domains. Above some voltage U_s an accumulation layer or dipole domain will start traveling towards the anode as was shown in section 1.4.2. If the voltage falls below some voltage U_e the traveling inhomogeneity will decay. Both processes will happen during each cycle of the AC field.

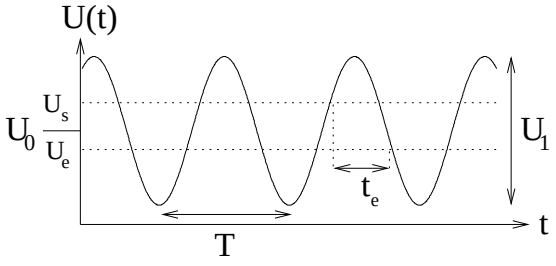

Fig. 1.12: *The sum of the AC and DC voltage according to equation (1.37). The voltage is assumed to rise above the voltage necessary for domain formation U_s and drop below the voltage where the domain disappears U_e during each cycle.*

I will start with small resonance frequencies and continue with larger and larger frequencies. If the time from the start of the domain to its decay t_e, is larger than the domain transit time the domain will reach the anode during the high-field part of the total voltage and disappear, but a new domain will not be started before the voltage grows above U_s again. This is the case of delayed domains and the oscillations in the superlattice will have a slightly lower frequency than without the cavity.

If the time t_e is a little smaller than the transit time t_{tr}, the domain will decay before it reaches the anode as soon as the voltage drops below U_e. This is the case of quenched domains and the oscillations in the superlattice will have slightly higher frequency than without the cavity. The frequency of the oscillations in Gunn oscillators can be tuned by the resonance frequency of the cavity, from 0.5 to about 1.5 times the frequency of the pure oscillations. Reducing the time constant T further one can hope to avoid the formation of domains if t_e becomes smaller than the time of domain formation. This will be analyzed in the following.

1.5.2 Limited space-charge accumulation (LSA) mode

The LSA mode was first predicted theoretically for Gunn oscillators by J. A. Copeland [Cop66, Cop67a]. The idea is to avoid the domains which were responsible

for microwave emission up to now. If this can be achieved one can use the negative differential conductivity directly to enhance radiation (see section 1.3). I will assume first that the velocity v_d in the crystal follows the field in the crystal instantaneously. This is true if the frequency of the oscillating field is smaller than $\nu/2\pi \approx 1.6$ THz, where ν is the scattering frequency which is on the order of $10^{13}/\mathrm{s} = 10$ THz.

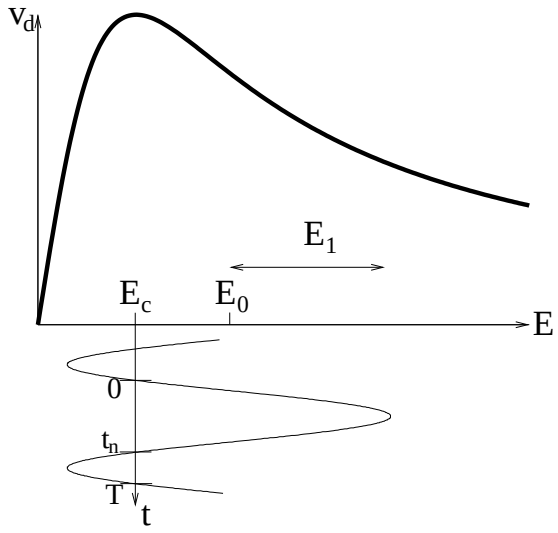

Fig. 1.13: *The figure depicts the working principle of the LSA mode. The superlattice is assumed to be homogeneous so that the field* $E(t) = E_0 + E_1\cos(\omega t)$ *can be deduced directly from the voltage* $U(t) = U_0 + U_1\cos(\omega t)$ *by the relation* $E = U/L$*. In addition to a constant supercritical voltage* $U_0 = E_0 L > E_c L$ *an AC voltage is applied so that the field drops below the critical field during each cycle. While the field* $E(t)$ *is larger than the critical field* E_c *(*$0 < t < t_n$*) inhomogeneities will grow due to the negative differential conductivity, while they will decay for* $E(t) < E_c$ *(*$t_n < t < T$*). If the decay factor is larger than the growth factor, the assumption of homogeneity is justified a posteriori.*

The applied high-frequency field E will be homogeneous in the crystal if one can avoid the domains and it is simply given by $E(t) = U(t)/L$ so that one can write $E(t) = E_0 + E_1\cos(\omega t)$ with equation (1.40). The current-voltage relation will have the same form as the v_d-E relation. The high-frequency velocity v_ω will have opposite phase to the high-frequency field E_1 in the NDC region at least for small amplitudes E_1, and the integral $\int v_\omega(t)E_1(t)dt$ is negative, indicating that the radiation is amplified.

To avoid inhomogeneities in the sample it is not sufficient to make the time constant T of the applied field shorter than the time of domain formation t_f. Fig. 1.13 shows schematically the situation for the LSA mode. Even if during

the high-field portion of one cycle ($0 < t < t_n$) a mature domain is not formed, a macroscopic inhomogeneity can be formed over many cycles if the inhomogeneity does not disappear during the low-field portion ($t_n < t < T$) of one cycle. The assumption of a homogeneous sample then cannot be used anymore. For a more quantitative analysis I go back to the space-charge wave analysis of section 1.4.1. For the small signal growth of space-charge the diffusion can be neglected and it is described by

$$n_k = n_k^0 \exp(-\omega_c t) \tag{1.41}$$

with $\omega_c = \sigma_d/\epsilon\epsilon_0$. Below the threshold ($t_n < t < T$) σ_d is positive so that the space-charge decays exponentially, but above threshold ($0 < t < t_n$) it is negative so that exponential space-charge growth occurs. For a time-dependent field the space-charge existing after time T is the infinite product of infinitesimal amounts of growth or decay with varying rates. Because of the exponential form this simplifies to

$$n_k = n_k^0 \exp\left(-\int_0^T \omega_c(t')dt'\right) \ . \tag{1.42}$$

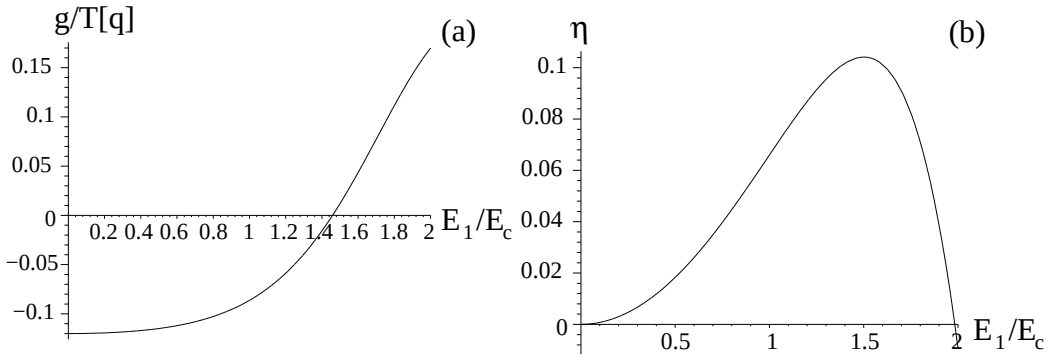

Fig. 1.14: *The growth factor g/T (a) in units of $q = \frac{env_0}{\epsilon\epsilon_0 E_c}$ and the efficiency η (b) for the LSA mode as function of the AC field E_1. In both cases the applied DC voltage $U = 2\ U_c$ results in an electric field $E = 2\ E_c$. The sign of the growth factor g determines whether inhomogeneities will grow with time and the LSA mode is stable. Assuming homogeneity the efficiency η which is the ratio of the power emitted at the applied frequency and the power absorbed at the applied DC voltage can be calculated. If the growth factor is positive and the efficiency η positive, the homogeneous state is stable and incident microwave radiation is enhanced.*

If the integral $g := \int_0^T \omega_c(t')dt'$ in the exponent is positive, space-charges will decay with time. Fig. 1.14a shows the integral for an applied voltage of $E_0 = 2$ E_c and different applied amplitudes E_1. For the velocity-field relation Eq. (1.17)

we get for the integrand

$$\omega_c = \underbrace{\frac{env_0}{\epsilon\epsilon_0 E_c}}_{q} \frac{1-(E/E_c)^2}{\left(1+(E/E_c)^2\right)^2} \; . \tag{1.43}$$

It might be surprising that the average of the derivative can be positive since the applied voltage is most of the time in the region with negative slope. This can be explained by the fact that the curve passes the region with largest negative slope very fast and spends much time in regions with high positive and small negative slopes. The amplitude E_1 has to be nearly equal to the DC field so that the field goes down below the critical field E_c and stays long enough in the region with positive mobility.

Of course it is not clear that for voltages with those large amplitudes there still exists gain since in our early considerations indicating gain the amplitudes were small. To see whether gain exists one needs to compute the quantity $\int_0^T E_1 \cos(\omega t') v_d(t') dt'$ which can easily be done if one assumes that the velocity follows the field instantaneously. If this quantity is negative, there is gain at the applied frequency ω. A convenient measure for devices is the efficiency which is defined by

$$\eta = -\frac{\int_0^T E_1 \cos(\omega t') v_d(t') dt'}{\int_0^T E_0 v_d(t') dt'} \; . \tag{1.44}$$

It is the ratio of the power emitted at the applied frequency and the power absorbed at the applied DC voltage. Fig. 1.14b shows the efficiency for $E_0 = 2$ E_c and different applied amplitudes E_1. It can become as large as 10 per cent, but at that value of E_1 the integrated mobility just starts to be positive. In fact, the region where there is gain and space-charges decay is rather small and goes from approximately $E_1 = 1.5$ E_c to $E_1 = 2$ E_c.

One more point needs to be addressed. The space-charges not only have to decay over one cycle, they are also not allowed to grow so large during one cycle that homogeneity is destroyed since the whole derivation rested on this assumption. The maximum growth factor g_m in the exponential of Eq. (1.44) over one period is

$$g_m = \int_0^{t_n} -\omega_c(t') dt' \leq T \frac{en}{\epsilon\epsilon_0} (-\mu_d)_{max} \leq nT \frac{e}{\epsilon\epsilon_0} \frac{v_d}{8E_c} \; . \tag{1.45}$$

One has $g_m \leq 1$ if $nT < 3{\times}10^5 \mathrm{s/cm^3}$ or $T < 3{\times}10^{-12}\mathrm{s}$ for a doping $n = 10^{17}/\mathrm{cm^3}$.

After the prediction of the LSA mode in Gunn diodes some groups believed to see experimental signs of it [Ken67, Iko69], but later Kroemer maintained that the energy relaxation times are too long in GaAs to really suppress the domains [Kro78]. Taking into account earlier calculations by Jones and Rees [Jon73] he

made an estimation that the LSA mode is not possible for frequencies higher than 20 GHz. He explained the high-frequency oscillations with the fast creation and annihilation of accumulation layers. Subsequent publications on high-frequency Gunn diodes suggested a somewhat higher frequency limit of 60 GHz for the LSA mode [Fri83], but in all later publications the oscillations were attributed to running accumulation layers or dipole domains [Suc98, Dun03]. If the LSA mode was ever realized, it was only observed in early experiments and at low frequencies, but all technologically relevant Gunn emitters today work with running domains [Eis04].

Despite the fact that it was probably never really achieved in the experiment I treated the LSA mode in detail because Kroemer suggested an operation mode in superlattices that reminds very much of the LSA mode [Kro00a] and which extends earlier considerations by Ignatov *et al.* [Ign93]. The model that Kroemer uses is more general than the LSA mode and the result reduces to the LSA behavior in the limit of small frequencies. While the long energy relaxation times inhibit the LSA mode in homogeneous GaAs, for the mechanism in superlattices proposed by Kroemer he uses a model which explicitly includes energy and momentum relaxation effects. For the drift velocity the result for an applied field $E = E_0 + E_1 \cos(\omega t)$ is

$$v = \sum_{m=-\infty}^{\infty} J_m^2 \left(\frac{E_1/E_c}{\omega\tau} \right) v_d(E_0 - m\omega\tau E_c) \tag{1.46}$$

where the function v_d is given by Eq. (1.23) with $\delta = 1$ since elastic scattering is ignored. The maximum of the curve is $v_p = v_0/4$ due to the choice of f_0 so that $\mathcal{I}_1/\mathcal{I}_0 = 1/2$. The velocity is given as a sum of DC velocity curves shifted by a field for which the potential drop across one superlattice period is equal to the photon energy at the drive frequency ω. Due to that Kroemer uses the term photon replicas for the $m \neq 0$ members of the sum. For small applied frequencies $z := \frac{E_1/E_c}{\omega\tau} > 1$ many terms will contribute to the sum and using a Bessel function identity from [Kov04] the expression can be simplified to

$$v = \frac{1}{2\pi} \int_0^{2\pi} v_d(E_0 + E_1 \cos u) du \tag{1.47}$$

which is just the average velocity that results if the drift velocity follows the oscillating field instantaneously. That is the model by Kroemer includes the LSA picture as a limiting case, a fact that was either not mentioned or overseen by Kroemer. Of course in this limit one recovers for the stability consideration the factor g found in the LSA calculations. Because of the fact that the Kroemer model includes the LSA mode I will call this operation mode *extended LSA mode* subsequently.

The second important requirement for the LSA operation was the high-frequency gain. The formula for the high-frequency differential mobility calculated by Kroemer

$$\mu_\omega = -\frac{2}{\omega\tau E_c} z^2 \sum_{m=-\infty}^{\infty} m J_m^2(z) \cdot v_d(E_0 - m\omega\tau E_c) \tag{1.48}$$

reduces using again Bessel function identities to

$$\mu_\omega = -\frac{1}{E_1}\frac{1}{\pi}\int_0^{2\pi} \cos u \cdot v_d(E_0 + E_1 \cos u) du \; . \tag{1.49}$$

The integral extracts the high-frequency component of the overall velocity from the drift velocity that follows the applied field instantaneously. Again this is the picture that was used in the LSA considerations, i. e. again one recovers the LSA result as a limiting case for small applied frequencies. For high-frequency irradiation $\omega\tau = 10$ the range around $E_0 = 10\ E_c$ is dominated by the $m = 1$ term in the sum, the $m = 0$ term does not contribute at all. Due to the minus-sign the differential mobility is negative in the region $E_0 > 10\ E_c$.

The main lesson that can be learned from the model by Kroemer is that the LSA mode for which the condition $\omega < 1/\tau$ is necessary can be extended to the high-frequency regime. One can find photon resonances then and if the photon energy and applied field are adjusted one can make use of these resonances to reach large high-frequency gain values, while the DC conductivity is positive. Of course an adverse point is that one needs strictly homogeneous samples to be inside the resonance range in the whole superlattice. This will be difficult to achieve if one includes boundaries. Another problem is that one needs to apply an electric field with a magnitude several times the critical field value E_c which will be difficult in the experiment. Still another problem is the construction of a resonator with frequencies in the Terahertz regime since cavities cannot be miniaturized arbitrarily. For example, a frequency of 16 THz would correspond to the case $\omega\tau = 10$ for a typical relaxation time $\tau = 100$ fs. Operation of quantum cascade lasers was already shown in that frequency regime and one would have to resort to the cavity designs developed there instead of the simple metallic cavities considered in this thesis if operation in that regime is the goal. In Chapter 3 the results of the extended LSA mode will be compared to numerical simulations with and without boundaries.

In the next chapter the derivation of a suitable transport model for the superlattice structures is carried out.

Chapter 2

Transport models for the superlattice structures

In this chapter the derivation of a suitable transport model for the superlattice structures is attempted. It was shown in the last chapter that the boundary conditions are crucial for the behavior of the device not only quantitatively, but also qualitatively. One of the possibilities that were discussed was an oscillating state with strong inhomogeneities in space and time. Analytical solutions can only be found for very simple homogeneous models which are not capable of reproducing this behavior. But also for numerical approaches one needs a rather simple model to allow for an inclusion of the boundaries and the spatial and temporal evolution. In the first section of this chapter different transport models are introduced and their potential as well as their limitations are discussed.

2.1 Hierarchy of the approaches for semiconductor transport

At the top of the hierarchy there are the approaches based on a quantum description of transport. A corresponding theory can be based on density matrices [Kuh98] or nonequilibrium Green functions [Hau96, Wac02]. This area is still the subject of much research. In both cases one needs simplifications to make the problem accessible to solutions. While the density matrix formalism is particularly useful for systems with long phase-relaxation times since the coherent temporal evolution can be directly obtained from a coupled set of differential equations, the Green function approach can efficiently deal with dissipative transport processes. From both approaches the Boltzmann equation for the semiclassical distribution in phase space $f(\mathbf{r}, \mathbf{k}, t)$ can be obtained

$$\frac{\partial f}{\partial t} + \frac{1}{\hbar}\frac{\partial \varepsilon}{\partial \mathbf{k}} \cdot \nabla_{\mathbf{r}} f + e\mathbf{E} \cdot \nabla_{\mathbf{k}} f = \left.\frac{\partial f}{\partial t}\right|_{coll} . \tag{2.1}$$

$\varepsilon(k)$ is the one-particle dispersion relation and E is the electric field. The left-hand side of Eq. (2.1) describes the dynamics of particles without interaction. In Appendix A it is shown how this equation has to be modified for the case of a spatially varying periodic potential. This can be derived starting from the nonequilibrium Green functions formalism. The result will be used in section 2.2 when the boundary regions will be included in the description, but for now I will stick to the homogeneous problem. Scattering processes of the particles or of particles with impurities or phonons will give rise to a change of the distribution function $\partial f/\partial t|_{coll}$. The solution of the Boltzmann equation in general requires numerical methods.

The most popular numerical approach to the problem has been the Monte Carlo method [Jac83]. For a homogeneous system one simply models the motion of one particle as free motion, where the velocity is given by $\partial\varepsilon/\partial\mathbf{k}$ and the quasi-momentum $\mathbf{k}$ changes according to the semiclassical equation $\hbar\frac{\partial\mathbf{k}}{\partial t} = e\mathbf{E}$. The probabilities for the different scattering events summarized in $\partial f/\partial t|_{coll}$ can be calculated with Fermi's golden rule and the electron is scattered in the simulation process according to these probabilities. Assuming ergodicity the behavior of the electron ensemble in the device can be obtained if one waits long enough so that the electron has traced out the phase space. The Monte Carlo method has been used to treat the homogeneous transport problem in superlattices [Sch03]. If the system is not homogeneous, as is the case for the oscillating modes, one has to use an ensemble of electrons and couple the evolution of the ensemble to the Poisson equation. The computational effort for this simulation procedure can become very large and I am not aware of any Monte Carlo simulations for inhomogeneous superlattice transport.

The collision term involves the distribution function, and the Boltzmann equation is therefore a rather complicated integro-differential equation for $f(\mathbf{r}, \mathbf{k}, t)$. The most frequently used approximation for the collision term is the relaxation time approximation

$$\left.\frac{\partial f}{\partial t}\right|_{coll} = -\frac{1}{\tau_\varepsilon}\left(f(\mathbf{k}) - \frac{n}{n_0}f_0(\mathbf{k})\right) - \frac{1}{\tau_{el}}\frac{1}{2}\left(f(\mathbf{k}) - f(-\mathbf{k})\right) \tag{2.2}$$

which is a crude description of the relaxation kinetics towards equilibrium. Phonon scattering is assumed to restore the equilibrium distribution f_0 with the density adjusted to the local value if the distribution f deviates from the local equilibrium distribution. This term conserves the particle number. The second term describes elastic scattering processes which scatter electrons between degenerate states. It is assumed here that only the state at -$\mathbf{k}$ is degenerate to the state at $\mathbf{k}$ which is true only in one-dimensional systems, but is used here also as an approximation. If one reduces the problem also to one dimension, assuming homogeneity of the sample perpendicular to the transport direction, it is shown in

Appendix B that the Boltzmann equation can be simplified to

$$\frac{\partial f}{\partial t} + v_p \frac{\partial f}{\partial z} + \frac{eE}{\hbar}\frac{\partial f}{\partial k} = -\frac{1}{\tau_\varepsilon}\left(f(k) - \frac{n}{n_0} f_0(k)\right) - \frac{1}{\tau_{el}}\frac{1}{2}\left(f(k) - f(-k)\right) \quad (2.3)$$

which is the Ktitorov model used earlier extended to spatially inhomogeneous problems. While it is questionable whether a quantitative description is possible with this approximation, the goal of a qualitative description should be achievable. Due to the numerical effort necessary for the full Boltzmann equation I chose this approximation as one of the models for my simulations. It was shown that the elastic scattering term changes the results quantitatively, but not qualitatively [Ger93], and therefore most of the calculations were done without elastic scattering.

A further simplification is possible when the various transport variables are represented through average densities that are obtained as moments $\langle a \rangle$ of the distribution function which are defined by

$$\langle a \rangle = \frac{1}{n}\int a(k) f(k,x,t) dk. \quad (2.4)$$

In Appendix C it is shown how balance equations for the momentum and energy density are obtained from Eq. (2.3). Neglecting contributions which are small for $\Delta/k_B T \ll 1$ and assuming that $\tau_{el} = 0$, these can be written as

$$\frac{\partial(n\langle v\rangle)}{\partial t} + \frac{v_0^2}{2}\frac{\partial n}{\partial x} + \frac{ed^2}{\hbar^2} n\langle\varepsilon\rangle E = -\nu n\langle v\rangle \quad (2.5)$$

$$\frac{\partial(n\langle\varepsilon\rangle)}{\partial t} - en\langle v\rangle E = -\nu n(\langle\varepsilon\rangle - \varepsilon_T)\,. \quad (2.6)$$

Here $\nu = 1/\tau_\varepsilon$ is the inelastic scattering frequency. Together with the continuity equation one has a coupled set of differential equations which can be solved numerically. This is the second set of equations that were investigated doing a numerical analysis.

Under the assumption of slow variations in space and time, i. e. momentum and energy relaxation occur faster than all other processes, the moment-balance equations (2.5,2.6) can be further simplified to the drift-diffusion model (Appendix C). The drift-diffusion current

$$J = env = env_d - eD\frac{\partial n}{\partial x} \quad (2.7)$$

is composed of a drift term $J_d \propto v_d = \mu E = v_0 \frac{I_1}{I_0}\frac{E/E_c}{1+(E/E_c)^2}$ and a diffusion term $J_D = -eD\frac{\partial n}{\partial x}$. It is shown in Appendix C that the diffusion coefficient D is approximately given by the Einstein relation $D = \mu k_B T/e$, which was used in the numerical simulations.

At this point it should be stressed that with the last step in the progress towards simpler and simpler simulation equations one has given up the possibility to describe processes that happen faster than energy and momentum relaxation. Let us assume for the moment a relaxation time of 100 fs, which is realistic for the momentum relaxation. Any process happening with a frequency around $f = \omega/2\pi \approx 1$ THz or above will be out of reach for this model. Unfortunately this is the frequency with which domain creation is happening in the system (see Chapter 3). Apart from that it is also interesting to apply external high-frequency radiation to the system to see whether one can create higher harmonics or change the transport mode as suggested in section 1.5.2. The drift-diffusion model was used to describe domain motion and the response to external high-frequency radiation in semiconductor superlattices [Sch02b], but from the considerations above it is clear that the results have to be treated with care. An extension of the drift-diffusion model to include retardation effects is possible [Bon03].

In section 3.1 the numerical results of the homogeneous problem are compared for three different models: the Boltzmann transport equation in the form of Eq. (2.3), the moment-balance equations in the form of Eqs. (2.5,2.6) and the drift-diffusion model in the form of Eq. (2.7). Different schemes had to be introduced to tackle the differential equations of the three models. The Boltzmann equation and the drift-diffusion equation were discretized using an upwind differencing method, while this procedure did not work for the moment-balance equations. The most stable scheme which was found there was a simple central difference approach. Unfortunately the upwind differencing scheme introduces additional diffusion effects. An advantage of the upwind procedure is its stability when applied to the Boltzmann equation which made it possible to choose the time-steps for the Boltzmann equation one order of magnitude larger than for the moment-balance equations. In effect the computational effort for the calculations was nearly the same for the Boltzmann and the moment-balance equation, while the effort was considerably smaller for the drift-diffusion model.

While it is interesting to see how the results change when simplifying the equations step by step one needs to include the boundaries in the different models since it was shown in Chapter 1 that the behavior depends crucially on the boundary conditions. This is the purpose of the next section.

2.2 Boundary conditions

It was recognized early that the creation of periodic behavior in the simulations is nontrivial. In many of the numerical treatments on the Gunn effect a so-called “notch” [McC66, Suc98] is introduced which is a short region with smaller doping density close to the cathode. The notch is actually a source of both

an accumulation and a depletion layer and for a large notch the accumulation layer can take over the role of the primary accumulation layer which develops at the cathode when the field ahead of the cathode is never permitted to exceed threshold. The accumulation layer will merge with the depletion layer introduced by the notch and the dipole domain propagates to the anode and the process is repeated.

The attitude towards the boundary conditions in the drift-diffusion simulations in superlattices that were done up to now can be exemplified by the statement: "we have chosen bias and boundary conditions so that dipole mediated current oscillations occur" [Bon03]. This position was already adopted in [Kro68] where the Gunn effect in GaAs was treated. Without giving a microscopic justification for the boundary conditions that he used Kroemer rather made some general assumptions about the contact region. As described in section 1.4.2 especially the assumption of high electric fields in the highly doped GaAs contact region, which at first sight seems counterintuitive, produced behavior that was in good agreement with the experimental observations and the situation is similar in the superlattice simulations. Only if the field in the contact region is high which coincides with the case of limiting contacts described in section 1.4.2 one can observe oscillating modes. Of course it should be possible to find afterwards a justification for the boundary conditions employed (see e. g. [Sch02b]) since using totally arbitrary conditions to produce some determined behavior is not satisfactory.

A different approach is to start with a realistic microscopic model and derive boundary conditions from that. This was one of the goals of this work. If the resulting model does not produce the observed experimental observations, one is tempted to modify the model until the result coincides with the experiment and in the end the difference to the previous approach may be small. But one has still a microscopic model at hand which may coincide with the real system and describe its behavior in new parameter regimes.

It was shown in Chapter 1 that the boundary conditions, especially the electric field value at the transition from the bulk material to the superlattice, is crucial for the behavior of the device. Even in the absence of an applied voltage there will be contact voltages between the two regions if the Fermi energies of the regions are different which will be the usual case. The Fermi energy will depend both on the difference in electron affinity and the doping density. Assuming a linear drift velocity versus field relation in the highly doped contact material, the main parameter in the drift-diffusion model is the mobility μ which has to be chosen small in the contact region to produce oscillating behavior. A better starting point is then the Boltzmann equation, with which the distribution in k-space is fully described. The derivation of boundary conditions for the Boltzmann equation will be done in the following sections for two different microscopic models

of the boundary.

2.2.1 Discontinuous transition

Fig. 2.1 shows the boundary conditions that were used in the case of a discontinuous transition. Only electrons from the bulk GaAs material whose energy matches the energy of the lowest miniband enter the superlattice and electrons with other energy values are reflected. Even without applied voltage there is an electron flow from the region with higher density to the region with lower density. Since the particle density at the same energy value is determining this, the flow can be opposite to the flow that would result from the doping gradient. The process continues until the drift current resulting from the electric field that builds up balances this diffusion current. This continues until the Fermi energies deep inside the material are at the same level on both sides of the boundary.

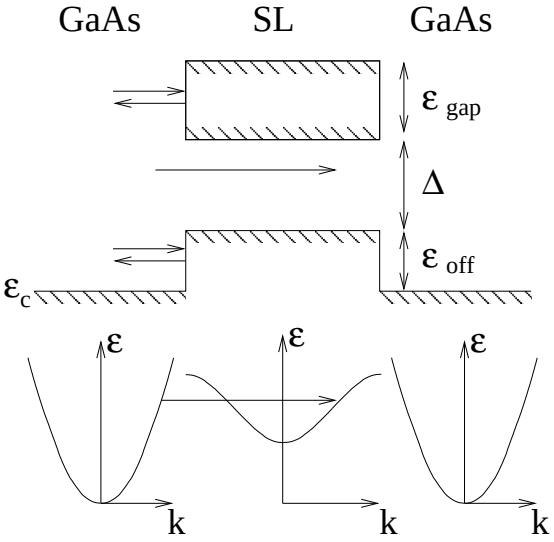

Fig. 2.1: *The superlattice including the boundaries with shaded forbidden regions (upper part) and the schematical dispersions in the GaAs boundaries and the superlattice region (lower part). Electrons enter the superlattice if the energy ε is within the superlattice miniband ($\varepsilon_{off} < \varepsilon < \varepsilon_{off} + \Delta$) and are otherwise reflected.*

On the level of the Boltzmann equation one needs the one-dimensional distribution function f' integrated over the perpendicular degrees of freedom. The equilibrium distribution is given by

$$f'_{(0)}(z,k) = \frac{L^2}{2\pi^2}\int f_0(k_x,k_y,k_z)dk_xdk_y = \frac{L^2}{2\pi}\frac{2m^*}{\beta\hbar^2}ln(1+e^{-\beta(\epsilon(k)-\mu)}) \qquad (2.8)$$

the derivation of which is shown in Appendix B. ε is the energy in the transport direction and μ has to be determined self-consistently from the condition $d/(2\pi)\int_{k_z} f'_{(0)}(z,k_z)dk_z = n_0(z)$. To get an impression of a typical situation in superlattices we determined the chemical potential μ for the standard superlattice from Tab. 1.1. The top left graph of Fig. 2.2 shows the conduction band edge

ε_c (solid line) and the chemical potential μ (dotted line) before the electrons are allowed to relax.

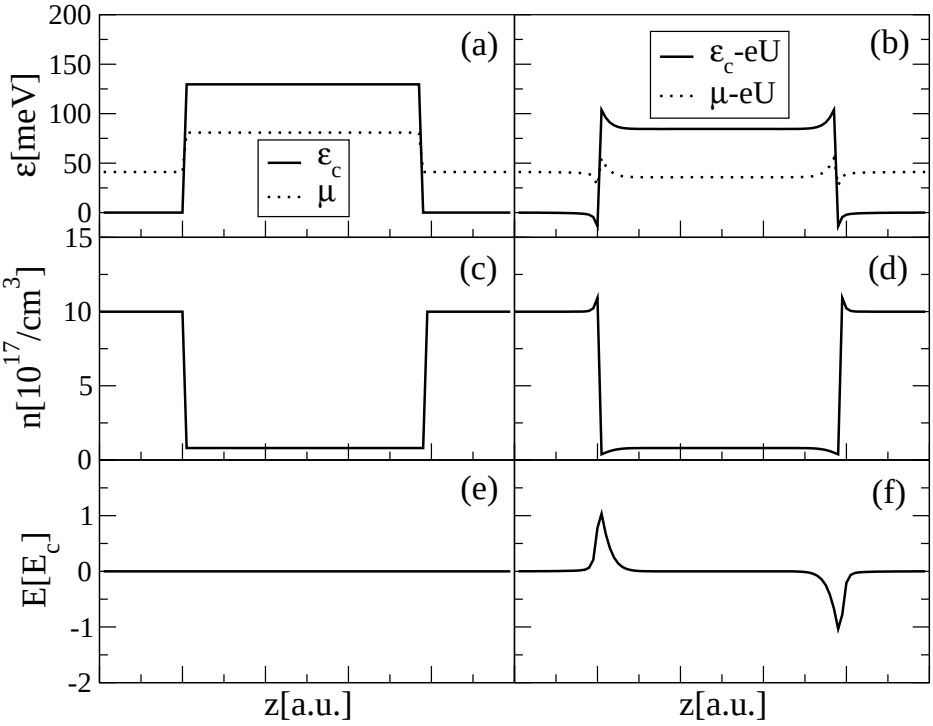

Fig. 2.2: *The conduction band edge, carrier density and electric field before (a,c,e) and after the relaxation (b,d,f) of the carriers at the interface between the superlattice and the contact region for the standard superlattice (Tab. 1.1). One can see that the chemical potential μ is higher in the superlattice region than in the contact region. This means that electrons will flow from the superlattice region into the contact region (d). The excess and defect electrons bend the conduction band edge ε_c until the chemical potentials are aligned. The electric field at the cathode contact is supercritical for zero applied voltage.*

One can see in Fig. 2.2 that GaAs is already degenerate ($\mu > \varepsilon_c$), while the electron gas in the superlattice is still non-degenerate ($\mu < \varepsilon_c$). Even though the density is much higher in the highly doped GaAs contact, the chemical potential is higher in the superlattice region due to the band offset $\varepsilon_{off} \approx 130$ meV. This means that electrons will flow from the low doped superlattice region into the highly doped contact region since the electron density is higher at the same energy in the superlattice. The density increases in the contact region and decreases in the superlattice region. This will continue until the chemical potentials inside the superlattice and in the contact region are aligned.

Fig. 2.2b shows the chemical potential and the conduction band edge including

the electric potential that originates in the excess electrons in the contact and defect electrons in the superlattice, $\mu - eU$ and $\varepsilon_c - eU$, respectively. The chemical potential which is ill-defined in the contact region, where the electron gas is not in equilibrium, has the same value deep inside the superlattice and outside. In the calculation due to the discretization the values are not exactly identical, but for increasing spatial resolution the two values approach each other.

Fig. 2.2f shows that the electric field at the contact is supercritical already for zero applied voltage. This justifies in hindsight the assumption in Chapter 1 that the electric field at the cathode contact is higher than the critical field value E_c. Depending on the doping density in the superlattice and contact region and the band offset the contact field can have different values. It is questionable whether our crude approximation of a discontinuous change of the dispersion relation can give a reliable result for the contact field, but at least the correct sign of the field should be reproduced since this depends on the chemical potentials in the respective materials which are determined by the doping.

The assumption that electrons always enter the superlattice if their energy is within the miniband energy is an approximation. The transmission and reflection probability for electrons approaching the superlattice can be calculated for example with a tight-binding model. Let us assume that the Hamiltonian is given by

$$\begin{aligned} H &= \sum_{n\leq -1} \left(\varepsilon_b b_n^\dagger b_n - \Delta_b/4 (b_{n-1}^\dagger b_n + b_n^\dagger b_{n-1}) \right) + \\ &\quad + \sum_{n\geq 1} \left(\varepsilon_0 a_n^\dagger a_n - \Delta/4 (a_{n+1}^\dagger a_n + a_n^\dagger a_{n+1}) \right) + \\ &\quad + t_0/4 (a_1^\dagger b_{-1} + b_{-1}^\dagger a_1) \end{aligned} \tag{2.9}$$

with band width $\Delta_b > \Delta$ so that the left side ($n \leq -1$) represents the boundary with a wide band and the right side ($n \geq 1$) represents the miniband. With a Fourier transform the dispersion relations

$$\varepsilon_b(k) = \varepsilon_b - \Delta_b/2 \cos(k_b d_b) \quad \text{and} \quad \varepsilon(k) = \varepsilon_0 - \Delta/2 \cos(kd) \tag{2.10}$$

can be obtained in the two regions. For $t_0 = \sqrt{\Delta \Delta_b}$ and equal lattice constants $d_b = d$ one obtains for the reflection probability of plane wave states

$$R = \frac{1 - \cos\left((k - k_b)d\right)}{1 - \cos\left((k + k_b)d\right)} \,. \tag{2.11}$$

In Fig. 2.3 the reflection probability is plotted as a function of the electron energy in the miniband region for a bandwidth in the boundary twice as large as in the superlattice $\Delta_b = 2\Delta$. For aligned miniband centers, i. e. $\varepsilon_0 = \varepsilon_b$, the reflection

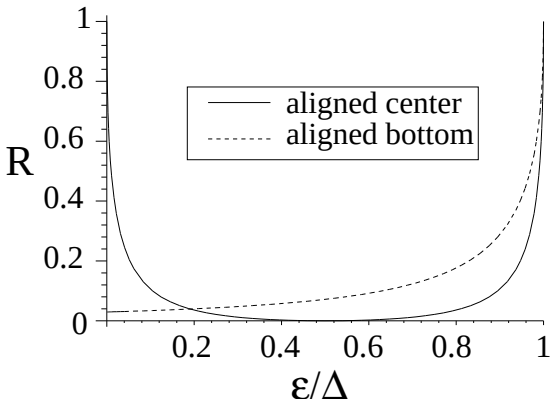

Fig. 2.3: *The reflection probability R of equation (2.11) for $\Delta_b = 2\Delta$ for aligned band centers and aligned band bottoms as function of the miniband energy.*

probability approaches 1 at the edges and is zero in the center (solid line). For aligned miniband bottoms the reflection probability is nearly zero at the lower edge and approaches 1 at the upper edge (dashed line). Altogether one observes that the reflection probability is nearly zero apart from the miniband edges and it was therefore neglected in the numerical calculations. The reflection at the upper edge plays no role anyway since the miniband width Δ is on the order of 100 meV $\approx 4\ k_BT$ so that the number of electrons is negligible there. For the reflection at the lower edge the band bending by the electric field is crucial and will be treated in the following.

In Fig. 2.2b one can see that a triangular barrier forms at the superlattice-contact interface even without applied voltage. Applying a voltage in forward direction, where forward direction means lowering the band edge of the right contact, so that electrons travel to the right, the triangular barrier will be even more peaked. Fig. 2.4 shows the situation schematically for a constant applied electric field E. There will be a finite tunneling probability into the superlattice for electrons whose energy is only by a small amount $\delta\varepsilon$ below the peak of the triangular barrier. Assuming a constant electric field value over the narrow tunneling region, the tunneling probability through the triangular barrier can be deduced from a simple WKB integration and one gets (see Appendix D)

$$P = \exp\left(-\frac{4}{3eE}\frac{\sqrt{2m_l^\star}}{\hbar}\delta\varepsilon^{3/2}\right) . \tag{2.12}$$

At the other side of the superlattice there will also be a finite tunneling probability out of the superlattice which was found in Appendix D to be

$$P = \exp\left(-\frac{\sqrt{2V_Qe\bar{E}}dm_l^\star}{\pi}\frac{4}{3}y^{3/2}\right) . \tag{2.13}$$

Here y is the distance from the superlattice end. Keeping y fixed, the triangular barrier increases with increasing field and the tunneling probability is reduced

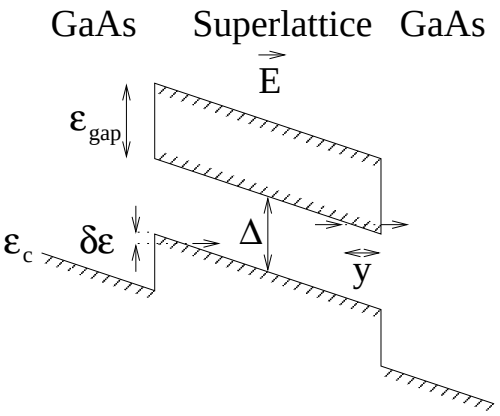

Fig. 2.4: *For finite applied voltage the miniband is tilted and triangular barriers are formed at both ends of the superlattice. The tunneling probability into the superlattice of electrons with energy being $\delta\varepsilon$ lower than the band edge is given by Eq. (2.12), while the probability of tunneling out of the superlattice from distance y from the superlattice end is given by Eq. (2.13).*

in contrast to the probability of tunneling into the superlattice which rises with increasing field E for a fixed energy. Of course the two tunneling processes are principally symmetric. However, for the simulation one needs the tunneling probability as a function of the energy deficit $\delta\varepsilon$ at the left side and as a function of the distance from the miniband end y at the right side.

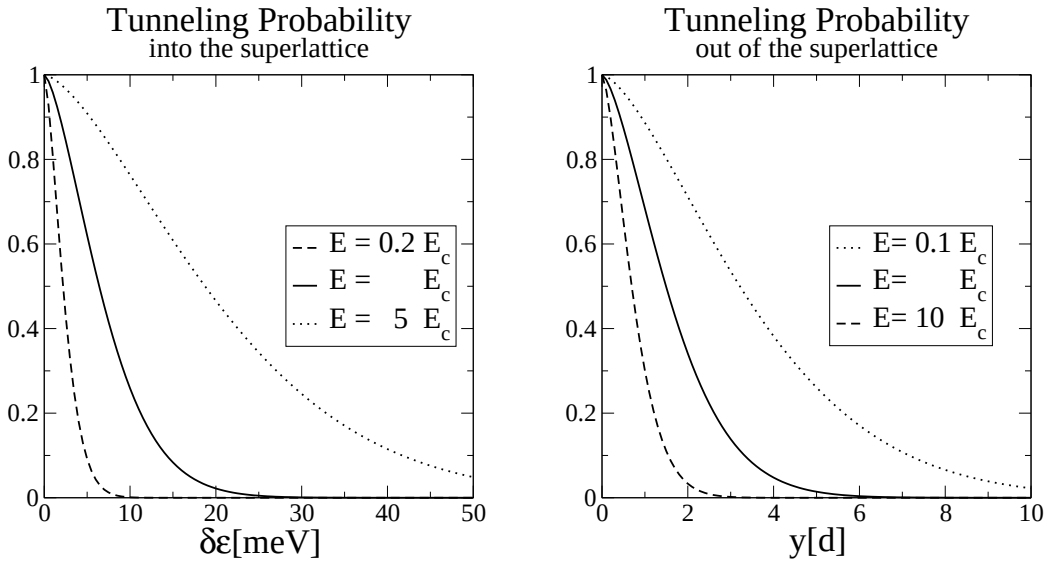

Fig. 2.5: *The tunneling probabilities into the superlattice and out of the superlattice as a function of the energy that the electrons are below the band edge $\delta\varepsilon$ and distance from the superlattice end y respectively.*

Both tunneling probabilities are shown in Fig. 2.5 for the standard superlattice (Tab. 1.1) as a function of the energy difference to the miniband edge $\delta\varepsilon$ and distance from the superlattice end y for different electric fields E. The barrier is effectively lowered for electrons approaching the superlattice from the left. Since

already without applied voltage the electric field value at the boundary is on the order of E_c (see Fig. 2.2f), the barrier is lowered by several meV and even more if the field is increased. The electric field value at the left contact does not increase very much for finite voltage since the current rises strongly if the voltage is increased due to the high doping level in the GaAs contact. The electric field at the cathode contact is somewhat reduced if one introduces the finite tunneling probability.

The probability for tunneling out of the superlattice becomes only relevant for $E > E_c$ since otherwise only few electrons reach the upper edge of the miniband. For our standard superlattice the tunneling probability is relevant only within a few superlattice constants d of the right contact. It turns out that this tunneling process is crucial for the annihilation of the anode domains. Without this term, standing anode domains form at lower overall voltages than with this term since the high field value associated with the standing domain quenches the transport into the contact region and the accumulation layer does not leave the superlattice. The tunneling supports the motion of the accumulated electrons through the triangular barrier into the contact region.

The assumption that the miniband dispersion starts immediately with the superlattice is a rather crude approximation since the dispersion relation is only valid for infinite superlattices. The finite size was only taken into account by incorporating the tunneling probabilities at both ends of the superlattice through the triangular barriers which are generated by a finite applied voltage. A totally different approach to the discontinuous transition considered up to now is to assume that the transition is smooth in the sense that one goes from the bulk material to the superlattice by slowly increasing the barrier width from zero to the value in the superlattice region. This will be considered in the next section.

2.2.2 Continuous transition

There are two reasons to consider a slow transition from the bulk material to the superlattice region. On the one hand it is a complementary approach to the discontinuous transition in the last subsection that can be treated exactly or at least the effects on the Boltzmann equation can be determined precisely, as will be shown. On the other hand it was tried by some groups to improve the injection of electrons into the superlattice region by growing a sequence of layers with slowly changing widths.

The question is now how to describe transport of electrons in this structure. In Appendix A the driving term in the Boltzmann equation is calculated for a periodic structure with slowly varying potential strength where a local dispersion $\varepsilon(k, z)$ can be defined. Here one obtains for the Boltzmann equation, neglecting

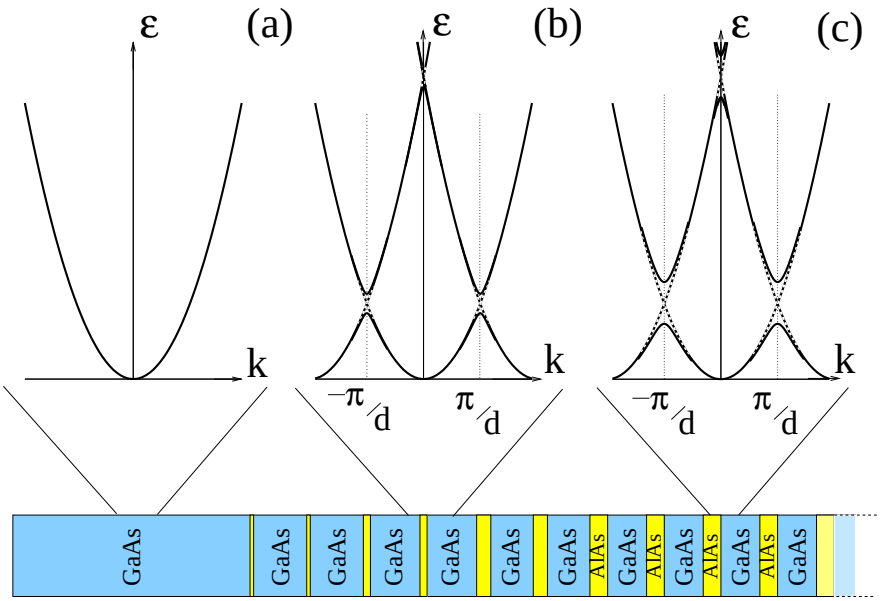

Fig. 2.6: *For a slowly changing periodic potential with constant lattice spacing d a local dispersion relations $\varepsilon(k,z)$ can be defined. The free parabola (a) is modified only at the Brillouin zone boundary for a weak periodic potential (b). The stronger the periodic potential becomes the wider is the gap that opens up (c).*

scattering processes for the moment (see Eq. (A.49)),

$$\frac{\partial f}{\partial t}+\frac{\partial \varepsilon(k,z)}{\partial k}\frac{\partial f}{\partial z}-\frac{\partial \varepsilon(k,z)}{\partial z}\frac{\partial f}{\partial k}+eE\frac{\partial f}{\partial k}=0\,. \tag{2.14}$$

Comparing this with the driving term in Eq. (2.3) there is an additional term coming from the spatial dependence of the dispersion relation. The origin of this term can be understood using the following argument. The total energy $\varepsilon_{tot} = \varepsilon(k,z) - eU$ of a particle traveling through the superlattice where $U = \int E dz$ is the local potential is conserved if

$$\frac{d\varepsilon_{tot}}{dt}=\frac{\partial \varepsilon}{\partial k}|_z\frac{dk}{dt}+\frac{\partial \varepsilon}{\partial z}|_k\frac{dz}{dt}-eE\frac{dz}{dt}=\left(\frac{dk}{dt}+\frac{\partial \varepsilon}{\partial z}-eE\right)v_k=0 \tag{2.15}$$

which holds if

$$\frac{dk}{dt}=eE-\frac{\partial \varepsilon}{\partial z}\,. \tag{2.16}$$

Inserting this into the total derivative of f equation (2.14) is obtained. The additional term in the Boltzmann equation that arises from the slowly varying potential can therefore also be derived by the condition that the electrons travel at a constant energy which is what one would expect from a semiclassical theory. Having this in mind one can transform the driving term of the Boltzmann

equation. Introducing the function $\tilde{f}(z, \varepsilon(k), t) = f(z, k, t)$ the spatial term can be rewritten as

$$\frac{\partial \varepsilon}{\partial k}|_z \frac{\partial f}{\partial z}|_k = \frac{\partial \varepsilon}{\partial k}|_z \left(\frac{\partial \tilde{f}}{\partial z}|_\varepsilon + \frac{\partial \tilde{f}}{\partial \varepsilon}|_z \frac{\partial \varepsilon}{\partial z}|_k \right) =$$

$$= \frac{\partial \varepsilon}{\partial k}|_z \left(\frac{\partial \tilde{f}}{\partial z}|_\varepsilon + \frac{\partial f}{\partial k}|_z \frac{\partial k}{\partial \varepsilon}|_z \left. \frac{\partial \varepsilon}{\partial z} \right|_k \right) = \frac{\partial \varepsilon}{\partial k}|_z \frac{\partial \tilde{f}}{\partial z}|_\varepsilon + \frac{\partial \varepsilon}{\partial z}|_k \frac{\partial f}{\partial k}|_z \, . \tag{2.17}$$

The last term cancels with the additional term in Eq. 2.14 to get

$$\frac{\partial \tilde{f}}{\partial t} + \frac{\partial \varepsilon}{\partial k} \frac{\partial \tilde{f}}{\partial z} + eE \frac{\partial \tilde{f}}{\partial \varepsilon} \frac{\partial \varepsilon}{\partial k} = 0 \, . \tag{2.18}$$

In the simulation the spatial derivatives are therefore calculated under a constant energy condition. When the equation is discretized for the numerical integration procedure this derivative at constant energy ε has to be handled with care. The upwind procedure which was used to discretize equation (2.14) and its extension to equation (2.18) are illustrated in detail in Appendix E.

In the last section the discontinuous transition was described by the assumption that the electrons enter the superlattice with constant energy and for that one calculates the densities in the neighboring k-points with the same energy in the contact region and the superlattices region. In the case of a continuous transition the discretization procedure ends in just the same instruction: calculate the k-value at which electrons in the neighboring point have the same energy. Reducing the number of steps over which the transition from the bulk dispersion to the superlattice dispersion happens to only one step, the continuous model actually goes over to the discontinuous model if the reflection processes are neglected.

Fig. 2.7 shows the situation before and after the relaxation of carriers at the boundary between the superlattice region and the contact region for the standard superlattice from Tab. 1.1. The width of the contact region is one fifth of the superlattice length, which amounts to 20 periods of the lattice. In the experiments the actual length of the smooth transition region is shorter on the order of five periods, but it is extended here to illustrate the behavior. It is assumed that the doping density n_0 changes linearly between the two regions (c), the conduction band edge ε_c is assumed to increase quadratically between the regions. The rearrangement of the charge carriers happens mainly within the transition region so that the density is hardly changed in the contact and superlattice region after the relaxation (d). The Fermi levels are nearly aligned after the relaxation (b), but now in contrast to the discontinuous transition no triangular barriers are formed. The Fermi levels are not exactly aligned due to the discretization, but for increasing number of grid-points in k-space the Fermi levels are finally aligned. The electric field peak is a little wider and the maximum a little lower than for the discontinuous transition (f).

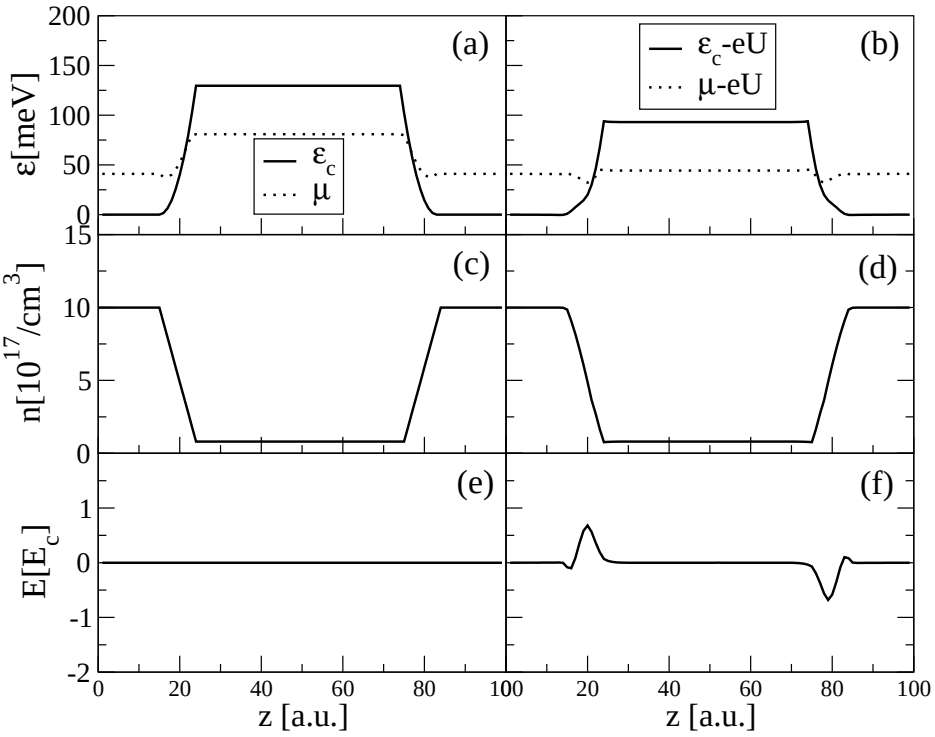

Fig. 2.7: *The conduction band edge ε_c, carrier density n and electric field E before (a,c,e) and after the relaxation (b,d,f) of the carriers at a smooth transition region from the superlattice region to the contact region for the standard superlattice (Tab. 1.1). The carriers redistribute themselves mainly in the contact region which has a width of one fifth of the lattice length. After the relaxation process the chemical potentials are aligned. The electric field peak at the cathode contact is a little wider and not as high as the field peak that arises in the discontinuous transition (Fig. 2.2).*

The field peak becomes higher again when the width of the transition region is decreased. In fact in the experiments the transition region is on the order of five superlattice constants which can only be resolved for higher resolution since this corresponds to only $2 \sim 3$ lattice points for the used resolution. Applying an electric field a triangular barrier will form again, but it is difficult now to calculate the tunneling probabilities since the shape of the barriers depends on the charge distribution inside the transition region. To limit the computation time most of the simulations in Chapter 3 were carried out with the discontinuous model.

In principle it is possible, at least for the discontinuous model, to derive boundary conditions for the moment-balance equations or the drift-diffusion model from the boundary conditions of the Boltzmann equation. These will depend on the distribution in k-space. Since the Boltzmann equation is numerically not more

expensive than the other models and more reliable in the high-frequency regime, this was not attempted. Instead of deriving the boundary conditions for the hydrodynamic equations or drift-diffusion equation from a microscopic model, it is probably better to test different boundary conditions for the models and choose those which produce the experimentally observed behavior. This approach was used in earlier drift-diffusion simulations [Sch02b, Bon03]. In the only simulations know to me which use a hydrodynamic model a "notch", which is a short low doped region in which the electric field will be high, was introduced to produce oscillating behavior [Cao99].

The model for the superlattice is now complete. It is well known from the experiments that the behavior of the device depends also on the surrounding in the experiment. It is attempted in the next section to set up a suitably detailed but still tractable model for the environment.

2.3 Influence of the surrounding

It is observed in the experiments that the surrounding has a large influence on the behavior of the superlattice devices. The treatment of the surrounding is split here into two parts: first a model for the current circuit is developed and then the proper description of a surrounding cavity is described.

2.3.1 Current circuit

Apart from any additional features of the surroundings the superlattice device is part of a current circuit. Fig. 2.8 shows a schematical drawing of the circuit. Since we model the internal dynamics and the capacitive effects of the boundary regions, we did not include a capacity parallel to the superlattice like other authors do [Sch02b]. To be more specific, the model which was described in section 1.4.2 describes the buildup and disappearance of charges at the boundary between contact and superlattice. Since this is the largest capacitance in the circuit, one does not need to include an extra capacitance. The wires and other circuit parts act as inductances which are summed in the inductance L. Additionally there can be resistive parts in the circuit modeled by an overall resistance R.

The capacitance of the superlattice is given by $C = \varepsilon\varepsilon_0 A/d$ which is $C = 23$ fF for a typical mesa area of 10 μm$\times$10 μm. In the calculations the voltage that is caused by the inductance $U_L = L\dot{I}$ is needed as a function of the current density $U_L = L\dot{j}A$. The antenna which couples the current oscillations to the electromagnetic field is a piece of wire of length 1 mm and diameter 0.03 mm and has an approximate inductance of $L \approx 1$ nH. A typical cavity with length scales on the order of 1 mm has also an approximate inductance of 1 nH.

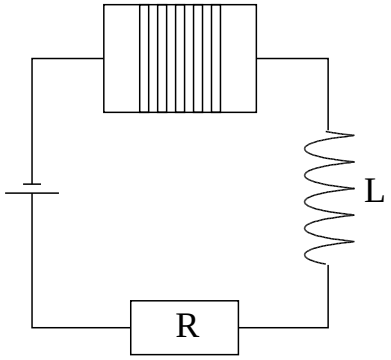

Fig. 2.8: *The current circuit in which the superlattice is situated. The superlattice acts as a capacitance, other capacitive effects of the circuit are neglected. The resistance R represents contact resistances between the semiconductor and the metal wires and of the metal wires itself.*

The frequency of the resonance circuit that is formed by the inductance L and the superlattice capacitance C is given by $f = \left(2\pi\sqrt{LC}\right)^{-1} \approx 30$ GHz. If the resonance frequency and the frequency of the free oscillations are of the same order of magnitude, both will interact, but in the simulations it was only possible to get results for rather small inductances on the order of 200 pH since for larger inductances growing oscillations lead to divergences. Especially in the voltage region where free oscillations were observed the calculations diverged for reasonable values of the circuit inductance. In a model developed in [Sch02a] an inductance with a much smaller value (3 pH) was used, but it is not clear how this small value can be justified.

2.3.2 Cavity

The next step towards a realistic description of the superlattice behavior is to include a resonator in which the superlattice may be situated. A model for a cavity is presented in Appendix F which is taken from [Ung89]. The ratio of the voltage across the superlattice U and the current through the cavity I can be considered as entrance impedance of the cavity $Z = U/I$. It is the sum $Z = \sum_n Z_n$ of impedances from each eigenmode of the cavity

$$Z_n = -i\omega_n l_n \left[\left(\frac{\omega_n}{\omega} - \frac{\omega}{\omega_n}\right) - \frac{1+i}{Q_n}\right]^{-1} \tag{2.19}$$

where ω_n are the eigenfrequencies of the cavity and Q_n introduces damping. l_n and Q_n are defined by the magnetic field $\mathbf{H}_n$ of the eigenmodes of the cavity

$$l_n := \mu_0^2 \left| \int_A \mathbf{H}_n d\mathbf{f} \right|^2 , \quad Q_n := \frac{\omega_n}{R_A \int df |\mathbf{H}_n|^2} . \tag{2.20}$$

For Eq. (2.19) one can find an equivalent circuit description. Each impedance coming from the different modes corresponds to the impedance of a resonance

circuit coupled inductively to the line. To show that let us consider a circuit as shown in Fig. 2.9. Each element consists of a parallel circuit of a capacitance C_n, a resistance R_n and a coil with inductance $L_{2,n}$. The coupling to the line occurs by another coil with inductance $L_{1,n}$. Both coils are linked by the mutual inductance $L_{12,n}$. For the latter we assume $L_{12,n}^2 = L_{1,n}L_{2,n}$ which holds if the same flux is going through both coils.

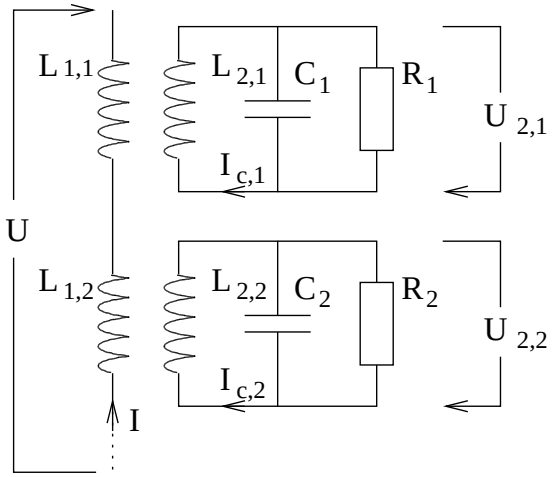

Fig. 2.9: *The influence of the cavity can be described by the depicted equivalent circuit. For each eigenmode of the cavity a parallel resonance circuit is coupled inductively to the line. The eigenfrequency of the equivalent circuit* $(L_{2,n}C_n)^{-1/2}$ *has to match the eigenfrequency* ω_n *of the eigenmode.* R *represents the dissipative effects caused by the surface resistance in the cavity.*

Let us call the current going through the line I, the voltage drop at the nth element $U_{1,n}$ and the current through the circuit $I_{c,n}$. $U_{2,n}$ is the voltage induced by the circuit inductance which equals the voltage drop over the capacitance and the resistance. Then we have for each element (dropping the index n for the moment)

$$U_1 = -i\omega L_1 I - i\omega L_{12} I_c \tag{2.21}$$

$$U_2 = i\omega L_2 I_c + i\omega L_{12} I \ . \tag{2.22}$$

For the current going through the parallel circuit we obtain

$$I_c = Y U_2, \quad Y = -i\omega C + \frac{1}{R} \ . \tag{2.23}$$

Eliminating U_2 and I_c from these equations we obtain

$$\frac{U_1}{I} = \frac{L_1}{L_2}\left[\frac{1}{-i\omega L_2} - i\omega C + \frac{1}{R}\right]^{-1} \tag{2.24}$$

which gives the impedance of the nth element

$$Z_n = \frac{L_{1,n}}{L_{2,n}}\left[\frac{1}{-i\omega L_{2,n}} - i\omega C_n + \frac{1}{R_n}\right]^{-1} \ . \tag{2.25}$$

Comparing the two expressions Z_n in Eqs. (2.19,2.25) we find the identifications

$$\omega_n = 1/\sqrt{L_{2,n}C_n}, \quad Q_n^{-1} = R_n^{-1}\sqrt{L_{2,n}/C_n} \quad \text{and} \quad l_n = L_{1,n} \; . \tag{2.26}$$

Here we have suppressed the small frequency shift produced by $1/Q_n$ for the resonance mode ω_n. Note that in an ideal situation the ratio L_1/L_2 is the ratio of the winding numbers of the two coils. The inductance of the coil in the line is given by $L_{1,n} = l_n$. This quantity defined in Eq. (2.20) has the dimension of an inductance due to the imposed normalization of the fields of the eigenmodes.

Since the eigenmodes of a cavity with given geometry can be calculated, one can use the equations above in differential form to model the influence of the cavity on the behavior of the superlattice device numerically. The inclusion of only an inductance was difficult for realistic values of the circuit inductance and more investigations would be necessary to get a conclusive picture of the effects of the cavity. Qualitatively one expects of course a strong interaction of the resonance circuit with the superlattice oscillations if the eigenfrequency of one eigenmode and the frequency of the current oscillations have nearly the same value.

In the experiments one observes voltage intervals in which the frequency stays constant which can be interpreted as regions where the frequency of the current oscillations is locked to an eigenfrequency of the cavity. An inclusion of the cavity seems to be necessary therefore to reproduce the experimentally measured current-voltage curves.

Chapter 3

Results of the numerical transport treatment

In the last chapter it was shown how one can derive different transport models for the description of carrier transport in semiconductor superlattices and now the numerical results are presented.

3.1 Comparison of different models for a homogeneous system

First the results are compared for an infinite system. This is achieved by imposing periodic boundary conditions on the simulation. If the results are either homogeneous or the resulting inhomogeneities are shorter than the periodicity length one can draw conclusions for the transport in real devices. It should be pointed out that even though the homogeneous problem is considered, the treatment is a crucial step towards a realistic device model compared to the homogeneous transport models used in most treatments of superlattice transport. Inhomogeneities which will arise because of the negative differential conductivity can develop and travel through the superlattice. The question of domain formation and annihilation is deferred to section 3.2 where boundaries are introduced.

3.1.1 DC transport

Before going into details I would like to discuss which questions one can reasonably try to answer with the presented models. It is of course tempting to try to reproduce the frequencies found in the experiments as was done e. g. in [Bon03]. In this case an extended drift-diffusion model was used, and to get the oscillation frequencies one needs to know the elastic and inelastic scattering frequencies ν_{el} and ν_{ε}. While the inelastic frequency may be similar to that of bulk GaAs, the

elastic frequency will depend on the surface roughness of the superlattice structure and is therefore unknown. It was shown in section 1.3 that it is possible to deduce the scattering frequencies from the critical field $E_c \propto \sqrt{\nu_\varepsilon \cdot (\nu_\varepsilon + \nu_{el})}$ and the peak velocity $v_p \propto \sqrt{\nu_\varepsilon/(\nu_\varepsilon + \nu_{el})}$. This is true only under the assumption that the three dimensional form of the elastic scattering is really given by the simple approximation presented in equation (2.3). It is shown in [Ger93] that the results of the full three-dimensional scattering agree only qualitatively, not quantitatively. In addition to that the determination of v_p involves the area of the superlattice mesa since the current I is measured and has to be divided by A to get the current density j. Summing up these uncertainties the scattering frequencies which were determined in [Sch98b] give only approximate values of the real scattering frequencies. Taking this into account it is futile to attempt to reproduce the measured frequencies with the existing models.

While the absolute frequency will not be accessible with the presented models, the qualitative behavior of the frequency when the applied voltage is changed can be investigated. If one assumes that the current oscillations originate in traveling domains, the time it takes for the dipole domain to traverse the sample $t_0 = L/v_{dom}$ where v_{dom} is the domain velocity and L is the superlattice length will set the time scale for the current oscillations. The domain velocity and particularly the evolution of the velocity when the voltage is changed can be calculated with cyclic boundary conditions. Before that the different domain profiles of the three models are shown.

Fig. 3.1 shows the density and field distribution for the dipole domains that develop as soon as the field becomes larger than the critical field E_c which is in the homogeneous model equivalent to $U = U_c = E_c L$. The shape of the dipole domain can be calculated for the drift-diffusion model analytically and was reproduced numerically in [Bon03, Sch02b]. The result of the drift-diffusion model differs only slightly from the moment-balance model, while the Boltzmann equation results in a larger diffusion which spreads the dipole domain over a wider region. With rising voltage the accumulation layer increases its height, while the depletion layer becomes wider since the density cannot drop below zero. I will not discuss the shape of the domains any further since it is experimentally difficult to observe, but rather continue with a discussion of the velocities with which the domains travel through the superlattice.

If the motion of the domains is really responsible for the current oscillations and therefore for the microwave emission, the velocity of the domains is an important parameter. It determines, apart from the creation and annihilation processes which are deferred until the next chapter the frequency of the oscillations. Instead of presenting the velocities, the frequencies that would result from the domain velocities in a sample of length L will be presented. If the creation and annihilation processes are not very strongly voltage dependent the trend should also be

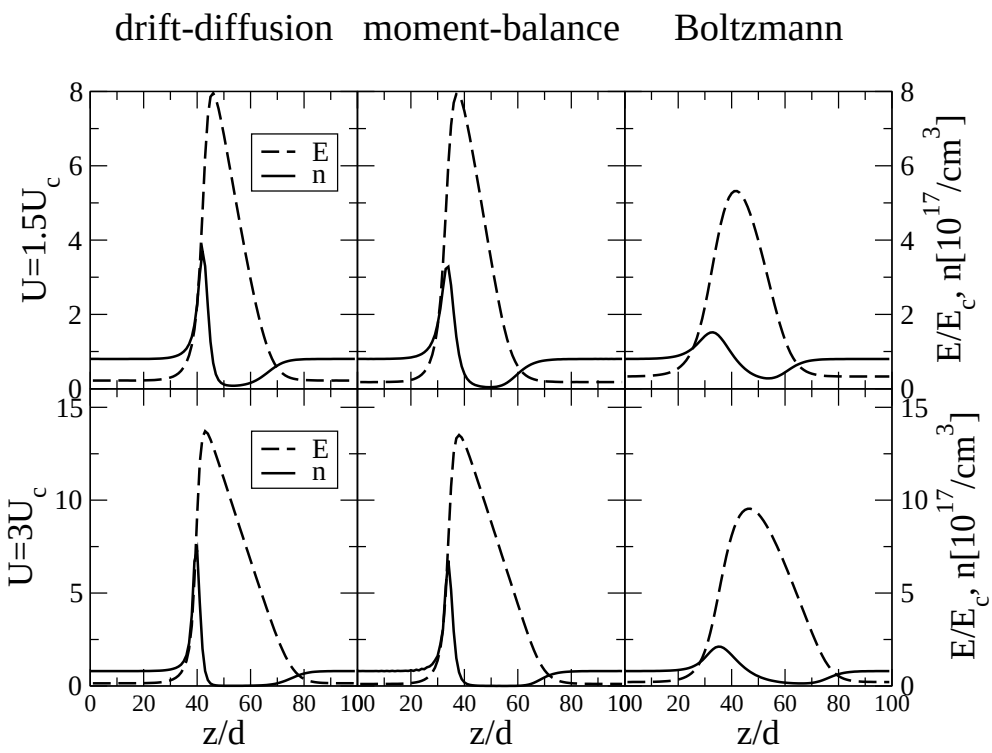

Fig. 3.1: *The density profile n and the electric field profile E measured in units of the critical field E_c for the three different models that were investigated. In all cases as soon as the voltage becomes supercritical, i. e. $U_c = E_c L$, a dipole domain develops that travels through the superlattice. The curves are shown for an applied voltage $U = 1.5\ U_c$ and $U = 3\ U_c$. There is hardly any difference between the result of the drift-diffusion and the moment-balance equations. The Boltzmann equation has stronger diffusion effects and broadens the dipole domain.*

found in the experiments.

Fig. 3.2 shows the frequencies for the three different models as a function of the applied voltage. To see the qualitative effect of the elastic scattering term elastic scattering was also included with a frequency of $\nu_{el} = \nu_\varepsilon = 10$ THz (dashed lines). The strong dependence of the frequency from the voltage stems from the observation that the field inside the domain is growing with growing voltage. Since the drift velocity inside the domain drops with increasing field, the velocity of the domain also drops. This effect is weaker in the Boltzmann case, but is still pronounced enough that it should be visible in the experiments. It is not fully clear why the moment-balance equation leads to a smaller velocity than the other two models.

It should be noted that the integrating procedure has an influence on the do-

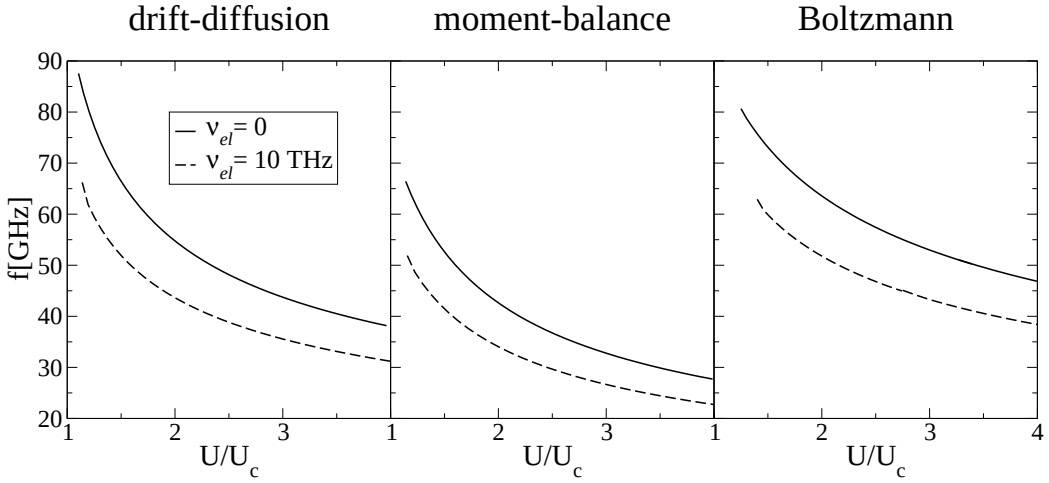

Fig. 3.2: *The frequencies that would result from the drift velocity $f = v_{dom}/L$ for the three different investigated models with (solid lines) and without elastic scattering (dashed line). The frequencies are strongly voltage dependent.*

main velocity. For the drift-diffusion model instead of the upwind scheme (see Appendix E) also a central difference scheme was stable and tested. It turned out that the velocity is smaller, being close to the values that resulted from the moment-balance equations. However, it was already pointed out that the absolute value of the frequencies is not the goal of this investigations since the microscopic scattering times are unknown. In [Bon03] the authors took the same scattering times as we did ($\nu_{el} = \nu_\varepsilon = 10$ THz) and by adjusting the voltage they were successful in reproducing the measured frequencies. Looking at Fig. 3.2 it is not surprising that it is possible to reproduce the measured frequencies by adjusting the voltage since one covers a wide frequency range by changing the applied voltage.

The influence of the elastic scattering term was tested in all three models. The result can most easily be explained in the drift-diffusion model. For $\nu_{el} = \nu_\varepsilon =$ 10 THz the peak velocity $v_p \propto \sqrt{\nu_\varepsilon/(\nu_\varepsilon + \nu_{el})}$ is suppressed by a factor $1/\sqrt{2}$, but the frequency is reduced by a smaller amount since the field that accompanies the dipole domain is smaller measured in units of the new critical field $E_c' = \sqrt{2}E_c$. The drift velocity suppression is therefore smaller. In the other models the influence is not that transparent, but the effect is very similar.

Already at this point one can draw conclusions for the behavior of the device. I will first concentrate on the drift-diffusion model. For the boundary conditions that are normally used for the solution of the device, the creation and annihilation processes consume only a fraction of the total period (this will be elaborated on in section 3.2). Since the domain extends only over a fraction of the length, the velocity will be largely equal to that in the periodic system. Especially for voltages

that are only a little larger than the critical voltage the frequency calculated with the model is a rapidly varying function of the applied voltage. Let us therefore look for the moment at higher voltages where the change is less dramatic and compare the frequencies for U=1.5 U_c and U=2 U_c. In our model the frequency changes on the order of 20 per cent. In earlier publications using the drift-diffusion model [Bon03, Sch02b] this strong dependence of the frequency on the voltage was not mentioned, even though it is a general feature of the simulations [Per04] and in striking contrast to the experimental observations.

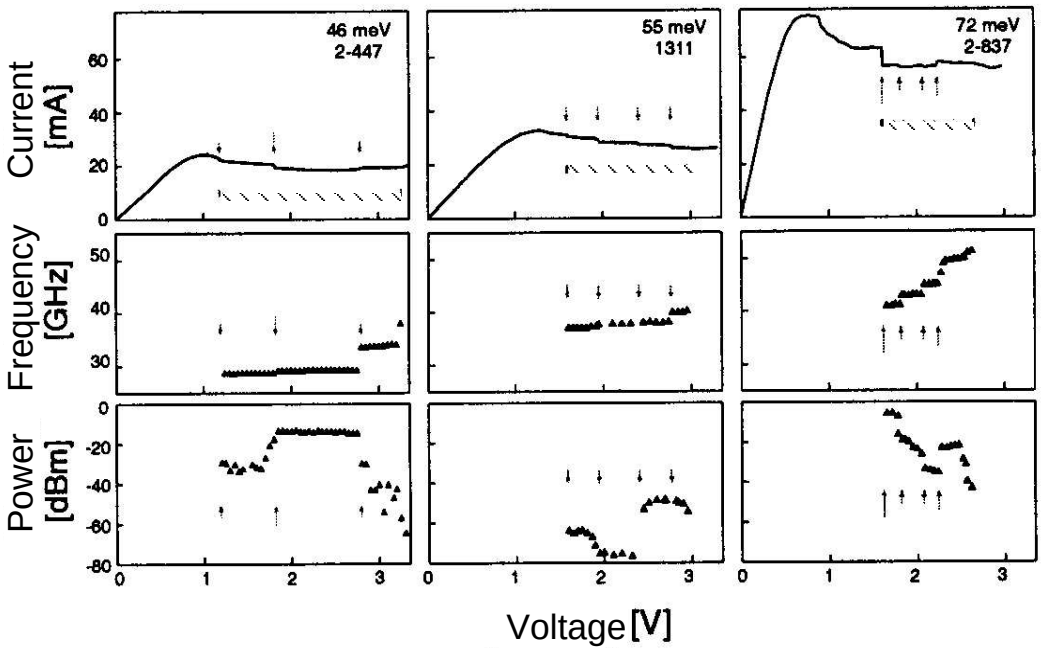

Fig. 3.3: *Measured current, frequency and power for three different superlattices with parameters given in table 3.1 taken from [Gre98]. In the shaded regions microwave radiation was observed. A sudden change in the observed current, microwave frequency and power occur at certain points which are indicated by small grey arrows. Between these points the frequency is nearly constant.*

Fig. 3.3 shows some measurements for real superlattices with parameters given in Tab. 3.1. While a discussion of the current and the produced power is postponed until the boundaries are added to the model, a discussion of the voltage dependence of the frequency follows. In all cases the frequency stays constant over some voltage region and then suddenly jumps to a different value at the points indicated by small grey arrows. The constance of the frequency is usually attributed to the coupling of the device to some external circuit which offers eigenfrequencies to which the frequency of the device locks. Of course according

probe	well width nm	barrier width nm	length μm	doping $10^{17}\mathrm{cm}^{-3}$	Δ_{exp} meV	Δ_{th} meV
2-447	4.80	0.90	0.57	0.8	46	57
1311	4.00	1.00	0.50	0.8	55	70
2-837	3.64	0.93	0.64	1.0	72	95

Tab. 3.1: *Parameters for the GaAs/AlAs superlattices of Fig. 3.3 from [Gre98]. The author used a different model for the miniband width which leads to a difference between the bandwidths Δ_{exp} in [Gre98] and the bandwidths Δ_{th} calculated with the model from Chapter 1. The second superlattice coincides with the standard parameters that were used throughout this thesis.*

to the simulations the frequency should jump to lower and lower values when the voltage is increased since the domain velocity becomes smaller and smaller, but the opposite is the case in the experiment. Only if the creation and annihilation processes become faster so that the decrease of the velocity is more than compensated, an increase of the frequency would result. Otherwise one should, especially for voltages which are only slightly supercritical, observe a rapidly decreasing frequency.

While the dipole domain motion is accepted by many authors [Bon03, Sch02b] as the origin of the microwave emission, the explanation of increasing frequency with increasing voltage remains an open problem. Some process in the experiment which is responsible for the growth of the frequency is not reproduced by the models introduced up to now. It should be noted that for Gunn diode simulations the frequency also drops with increasing voltage [Dun03] and the microwave frequency of the Gunn diodes tends to drop with increasing applied voltage.

To get a better understanding of the device one needs a realistic model of the boundaries as those can determine the overall behavior. In section 3.2 the results for two different approaches to that problem are presented. Before that the transport properties in an AC field are studied.

3.1.2 Behavior under external radiation

The AC voltage can be applied alone or in addition to a DC voltage. In the first case the nonlinear current-voltage characteristic will lead to the creation of higher harmonics. This will be even more pronounced if the amplitude of the field is large enough to enter the NDC regime. If the applied frequency is small enough so that the field is supercritical for a sufficient time, inhomogeneities can build up in the sample. Applying additionally a DC voltage one can separate two regimes: If the applied voltage is subcritical the behavior in the superlattice

will be periodic in the NDC regime for high enough AC voltage. In that case inhomogeneities will periodically build up if the applied frequency is small. If the applied DC voltage is already supercritical traveling dipole domains will form without AC voltage. It may however be possible to suppress the formation of domains with an applied AC voltage by the LSA mode operation of section 1.4.2. The buildup times of the domains and the domain suppression will of course be strongly influenced by the presence of the boundaries. Here we want to discuss only the basic principles of the behavior which is already rather complex before the boundaries are included in section 3.2.

Unbiased superlattices - frequency multiplication

Since an unbiased superlattice has ohmic behavior around zero applied voltage, it is necessary to apply radiation with rather high intensity to observe interesting phenomena. The first thing that always happens when applying high-frequency voltage to a nonlinear device is the creation of higher harmonics. For an antisymmetric current-voltage relation only odd harmonics will show up. For small applied frequencies one can simply use the static drift velocity versus field relation which for simplicity is assumed here to obey the Esaki-Tsu relation (1.17)

$$v_d(E) = v_0 \frac{E/E_c}{1+(E/E_c)^2} \ . \tag{3.1}$$

If the drift velocity follows the applied voltage $E = E_1 \sin(\omega t)$ instantaneously the amplitude of the third harmonic of the drift velocity $v_{3\omega}$ can be calculated easily. It is depicted in Fig. 3.4.

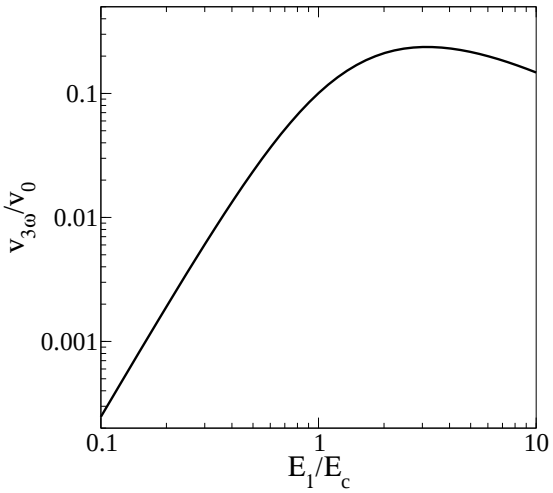

Fig. 3.4: *The third harmonic of the drift velocity $v_{3\omega}$ as a function of the amplitude of the driving field E_1. It increases cubically for small amplitudes and has a maximum of $v_{3\omega} \approx 0.25$.*

For small amplitudes it increases as E_1^3 since, defining $E'_{(1)} = E_{(1)}/E_c$, one gets

$$v_d\left(E(t)\right) \approx v_0 \cdot (E' - E'^3 + E'^5 - \cdots) = \tag{3.2}$$

$$= \quad v_0 \left[\left(E_1' - \frac{3E_1'^3}{4} \right) \sin(\omega t) + \left(\frac{E_1'^3}{4} - \frac{5E_1'^5}{16} \right) \sin(3\omega t) + \cdots \right] .$$

To get the current density one needs to take into account some additional factors. Since the distribution in k-space leads to a factor $\frac{\mathcal{I}_1}{\mathcal{I}_0}$ in the Esaki-Tsu relation, this factor and the density need to be accounted for if one wants to calculate the current density $j \propto nv_d$. In Fig. 3.5 the third harmonic numerical result of the current density using the Boltzmann equation is presented (solid line). The parameters used are the standard parameters from table 1.1 (a) and the parameters from table 3.2 (b). Constant doping density and periodic boundary conditions were assumed. The dotted line shows the curve from the static drift velocity versus field relation (Fig. 3.4), but the maximum value is normalized to the value of the numerically calculated curve to account for the factors of doping and k-space distribution.

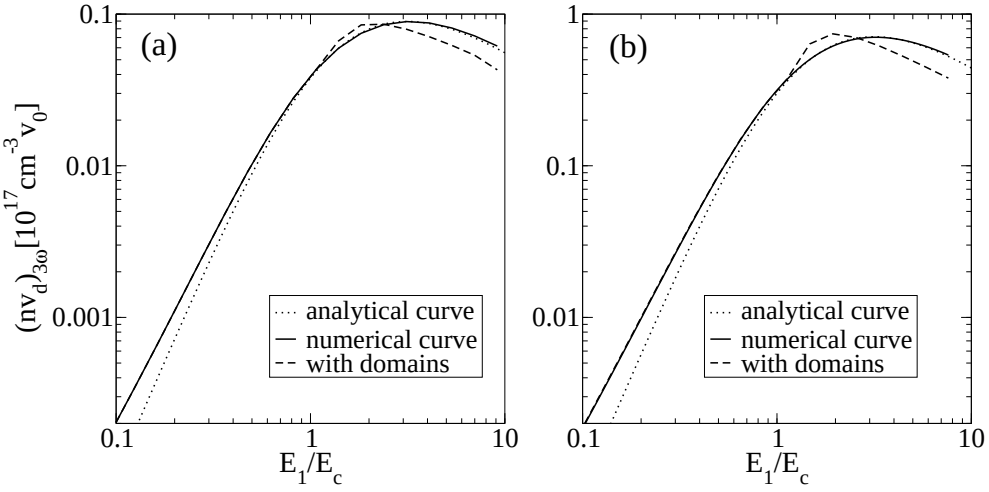

Fig. 3.5: *The third harmonics of the particle current density nv_d as a function of the amplitude of the driving field E_1 for the standard superlattice of table 1.1 (a) and the highly doped superlattice of table 3.2 (b) without boundaries. The solid lines show the numerical result of the Boltzmann equation calculation and the dotted line is the curve following from the static drift velocity field relation of Fig. 3.4 renormalized to the maximum of the numerical curve. If small fluctuations are added to the system dipole domains form as soon as the electric field exceeds the critical field (dashed lines). The applied frequency was $f = 10$ GHz (a) and $f = 50$ GHz (b).*

Considering a superlattice with doping fluctuations one has the additional possibility of dipole domain formation as soon as $E_1 > E_c$. The effect of this on the third harmonic of the current is shown in Fig. 3.5 (dashed line) where the applied frequency was $f = 10$ GHz for the standard superlattice and $f = 50$ GHz

	material	width	band-gap	band offset	doping	length
well	GaAs	5.1 nm	1.52 eV	1.06 eV	$2 \times 10^{18}\text{cm}^{-3}$	18 d
barrier	AlAs	1.1 nm	3.13 eV			

Tab. 3.2: *Parameters for a superlattice that was used in high-frequency multiplication experiments [Kla04a].*

for the highly doped superlattice since the domain formation happens faster in the second case. For larger frequencies the dipole domains did not form since the supercritical field periods were too short. For subcritical field values the two curves merge, the superlattice is always homogeneous then.

In both cases the amplitude of the third harmonic increases slightly as soon as domain formation in the superlattice is possible. In the experiment an increase of the emitted intensity by an order of magnitude is observed at some irradiation intensity [Kla04a] and is attributed to the onset of domain formation. The result for the highly doped superlattice without boundaries indicates that an increase of the third harmonic is to be expected as soon as domain formation sets in. Since the emitted power changes quadratically with the amplitude of the third harmonic, a strong increase is to be expected, but an increase by an order of magnitude cannot be fully explained.

If boundaries are taken into account, there will already be inhomogeneities for subcritically biased superlattices. After the introduction of the boundary treatment in section 3.2 the changes in the amplitude of the third harmonic will be presented.

Biased superlattices - current peak shift

If one applies high-frequency radiation to biased superlattices one is usually not interested in the creation of higher harmonics. Other questions are addressed by this process: the time of domain formation can be indirectly extracted from the measurement of the current. In principle it would also be possible to extract the time of domain formation from the unbiased case, but one needs rather high intensities to have supercritical fields $E_1 > E_c$ at frequencies of several hundred Gigahertz which is usually not easily accessible. In contrast to that one can also apply a slightly subcritical DC field, and with the addition of the high-frequency field the field is periodically supercritical.

The dielectric relaxation time is given by the inverse of ω_c (see Eq. (1.34))

$$\tau_c = \frac{\epsilon\epsilon_0}{\sigma_d} \tag{3.3}$$

where $\sigma_d = \partial j_d/\partial E$. It is the time constant for the growth of fluctuations in the NDC region. For the standard superlattice we get $\tau_c \approx 1$ ps for $E_0 = 1.3$ E_c. It takes several time constants τ_c to build up the dipole domain from the nearly homogeneous initial case. Assuming additionally that only for a fraction of one period the field is supercritical this should be possible only for frequencies below 100 GHz. This is indeed the case in the simulations, where the period during which the field is supercritical is long enough for domain formation only for frequencies below 100 GHz.

Fig. 3.6a shows the current density as a function of the applied electric field for small amplitude of the applied high-frequency field. The dotted line shows the current for homogeneous field, i. e. the superlattice is artificially kept in the homogeneous situation. For the non-irradiated case $E_1 = 0$ the curve is shown that results if the domains are allowed to form (grey curve). Above the critical field the current suddenly drops as soon as a domain is formed. When the high-frequency field is applied one can separate two frequency regimes: for large applied frequencies above 200 GHz domains cannot form in the short supercritical period and the current deviates only slightly from the curve without radiation (dashed curve). For frequencies below 100 GHz domains can form during the supercritical period and the current drops already for lower static field since with domains the current is suppressed (solid curve).

When the amplitude of the high-frequency field becomes larger already the homogeneous current density deviates from the current density without irradiation (Fig. 3.6b, dotted curve). If domains are allowed to form it is again crucial whether the frequency lies above or below 100 GHz. For frequencies around 200 GHz and above the current density drops as soon as the differential conductivity becomes sufficiently negative (dashed line). For 100 GHz (solid line) or 50 GHz (dash-dotted line) the domains form already for lower static voltage since then the supercritical period is again long enough for domains to form.

The current peak is shifted to the left and becomes smaller for small applied frequencies and this is caused by the formation of domains. On the other hand one can see from the dotted and dashed curve in Fig. 3.6b that the peak moves to the right if no domains are created and the superlattice is homogeneous or the frequency is so high that the supercritical part of one cycle does not suffice to produce a domain. In this way it was attempted to determine the time for domain formation in the superlattices since this time limits the maximum frequency that would be attainable in a device by the domain mode [Kla04]. The frequency limit that was determined this way was around several THz and thus much larger than the frequency limit determined by this simulation.

Of course the results change drastically if one includes the boundaries in the description. There will be rather large inhomogeneities already for subcritical voltage and therefore it will take less time for the domains to form and the fre-

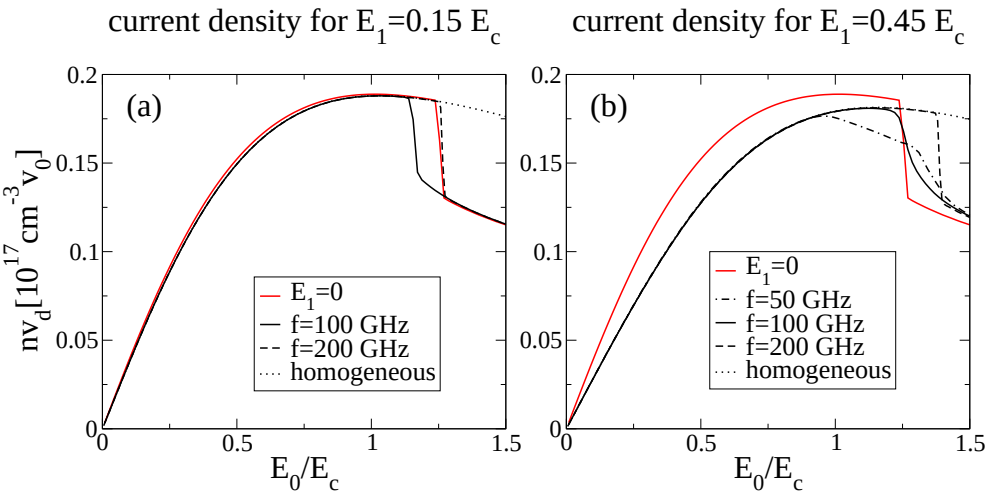

Fig. 3.6: *The current density for two different applied AC voltages when domain formation sets in compared to the homogeneous situation (dotted curves). The grey curve shows the situation for a superlattice without irradiation, but including domain formation. For large applied frequencies domain formation does not set in until the DC field E_0 is supercritical (dashed curves) since the domain formation is too slow. For small applied frequencies the domain formation suppresses the current already for lower voltages (solid curves).*

quency limit below which domains can form during the high-field part of the cycle will be much higher. As will be shown in the section on transport with boundaries there is unfortunately a rather large voltage region between the voltage peak and the onset of oscillations. This is not the case in the experiment where the oscillations start as soon as the current peak is reached. Our calculations indicate the the surrounding is crucial to create this behavior and our model does not incorporate these effects. To determine whether the maximum shifts to the right or to the left is thus not possible with the existing model since it does not capture the experimental processes around the current maximum which would be necessary to reproduce the experimental curves. A description of the processes with boundaries will therefore not be presented.

Supercritically biased superlattices - domain suppression

In section 1.5.2 the LSA mode was described which was first proposed for Gunn diodes to make use of the high-frequency negative differential conductivity while the homogeneous state is stabilized at the same time by the interaction with the generated high-frequency field. Kroemer has shown that one can go beyond the drift-diffusion model and then one can see photon resonances in the DC and AC

conductivities [Kro00a] which also result in high-frequency gain while inhomogeneities are suppressed. I have shown that the results obtained by Kroemer reduce to the results of the LSA mode calculations and therefore I introduced the term extended LSA mode. While the LSA description is only valid for frequencies below $\nu/2\pi \approx 1.6$ THz, the model developed by Kroemer is valid for large frequencies also. In this section I will first display the results of Kroemers description in a convenient way to see the effect of the phonon replicas and describe how Kroemer intended to take advantage of these. The same parameter range is then investigated with the numerical model used throughout this thesis.

At this point one might ask if it is reasonable to reproduce analytically obtained results via a numerical method. There are several points which justify such a procedure. First it is not clear from the outset what will happen if the differential DC conductivity is negative. Inhomogeneities will start to build, but it is not clear what the final state of this process will be. On the other hand one can start with a dipole domain and enter a region with positive DC conductivity. It is not clear whether the domain will decay since the positive DC conductivity was only calculated for the homogeneous situation. It will turn out that the region with positive conductivity and the regions which were homogeneous in the simulations overlap rather well which encourages one to repeat the calculations including the boundaries. Already Kroemer pointed out in his paper that a crucial factor for the question whether this mode will really be realizable in a device is the influence of the boundary region. The results for superlattices with boundaries will be presented in section 3.2.

In Fig. 3.7 the results of [Kro00a] are shown in a convenient way. Fixing the applied DC field E_0 to a certain value one can investigate the efficiency η (see Eq. (1.44)) which is the ratio of the of the power emitted at the applied frequency and the power absorbed at the applied DC voltage. It is plotted as a function of irradiation frequency f and amplitude E_1. The result is only shown if the efficiency is positive. For $E_0 = 2\ E_c$ the gain ($\eta > 0$) simply disappears if the frequency approaches $E_0/E_c \times 1.6$ THz. For increasing E_0 a resonance structure becomes apparent. In Chapter 1 it was shown that gain is obtained for $\omega\tau < E_0/E_c$ which results in $f < 8$ THz for $E_0 = 5\ E_c$ and $f < 16$ THz for $E_0 = 10\ E_c$. If this frequency criterion is fulfilled, there is only a small parameter region between the resonance peaks in which no gain is observed (in Fig. 3.7 these regions are hidden behind the peaks). In the limit of small frequencies the results of the LSA mode are obtained, for which the efficiency in the case $E = 2\ E_c$ was displayed in Fig. 1.14b.

The other important question is in which parameter regions the growth factor which is the integrated differential mobility is positive. Fig. 3.8 shows the derivative of the DC current with respect to the DC field E_0 as a function of frequency f and AC amplitude E_1. For small applied frequencies one retains the growth

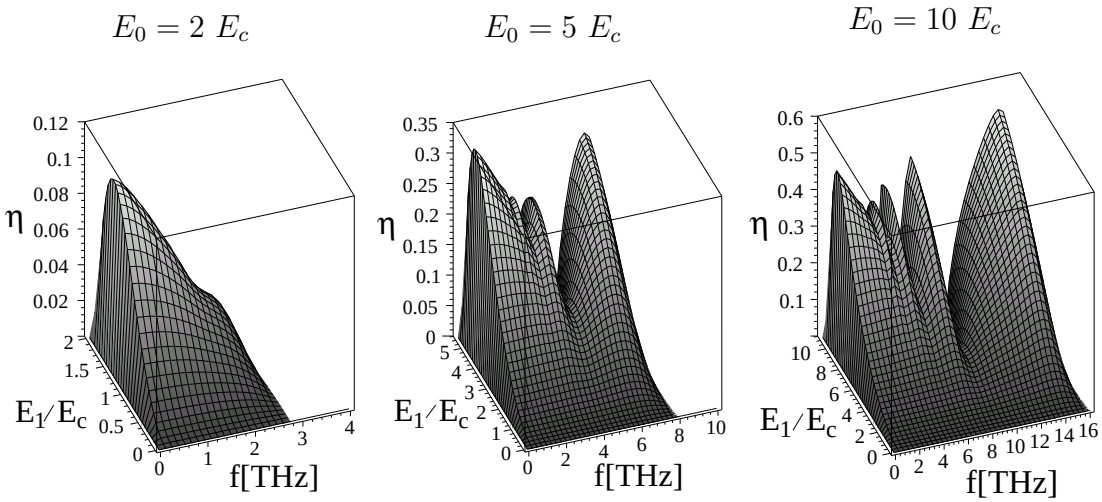

Fig. 3.7: *The efficiency η as a function of the applied frequency f and amplitude E_1 for three different DC fields for the model introduced by Kroemer [Kro00a]. In all cases the efficiency is positive for nearly all amplitudes as long as $f < 1.6\ THz \times E_0/E_c$. For high DC fields one observes photon resonances just below the frequency limit.*

factor $g/T[p]$ of the LSA mode. For the original LSA mode operation the amplitude of the AC field needs to be at least as large as $E_0 - E_c$ so that the field enters the region with positive mobility during each cycle. In this limit one needs rather large amplitudes E_1 for large applied DC amplitudes E_0.

For large applied frequencies the photon resonance gives large positive growth factor if $\omega\tau = E_0/E_c$ which is in the region around $f = 1.6$ THz$\times E_0/E_c$. These resonances can be clearly observed in Fig. 3.8 for $E_0 = 5\ E_c$ and $E_0 = 10\ E_c$ where the corresponding frequencies are $f = 8$ THz and $f = 16$ THz. One can also see multiphoton resonances at integer fractions of this frequency since the emission of several photons of a fraction of this frequency costs an equal amount of energy as one photon of the original frequency.

Summing up the results one sees that as long as one is below the cutoff frequency $f = E_0/E_c \times 1.6$ THz gain is usually observed, but the problem will be the homogeneity of the sample. It is rather difficult to test whether a system is stable for a given parameter set since even if the system becomes unstable with respect to long-range fluctuations it is not clear how long it will take for them to build up to a detectable size. The procedure that I chose for the simulations with periodic boundary conditions is the following: for each applied frequency f amplitude E_1 is increased very slowly within several nanoseconds to the maximum value. The relative change $r = \frac{E_{max}-E_{min}}{E_{average}}$ of the electric field inside the superlattice, with

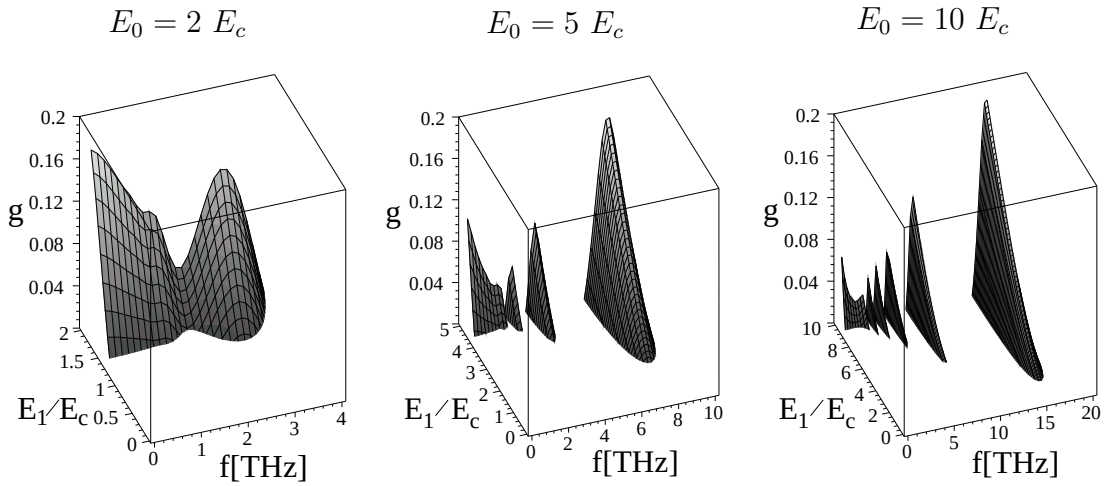

Fig. 3.8: *The growth factor g in units of* $qT = \frac{env_0}{\epsilon\epsilon_0 E_c}T$ *(see Eq. (1.43)) as a function of the applied frequency f and amplitude* E_1 *for three different applied DC fields* E_0*. It is positive for* $E_1 > E_0 - E_c$ *for small applied frequencies. For frequencies* $f = 1.6$ *THz* $\times E_0/E_c$ *one can observe resonance peaks. The amplitudes* E_1 *that are necessary for a positive growth factor are much smaller in that case.*

obvious definitions, is calculated several times in each interval.

Fig. 3.9 shows the result of that procedure for the different DC fields. Only the regions in which $r < 0.1$ are plotted. The parameter r is either close to zero indicating that the system is homogeneous or it is larger than 1 indicating that a domain travels through the system. The transition region between the region with and without domains is very small. For $E = 2\ E_c$ in the region 1.5 $E_c < E_1 < 2\ E_c$ and $f < 4$ THz, where the differential mobility in Fig. 3.8 was positive, no domains are observed in the simulations. For $E = 5\ E_c$ apart from this classical LSA region one can also see the resonance suppression of the domains around $f = 8$ THz, but the minimum field necessary is around $E_1 = 4$ E_c and is larger than in Fig. 3.8. Around $f = 4$ THz one can also see a slight suppression caused by the two-photon resonance. For $E = 10\ E_c$ one can see a domain suppression around $f = 16$ THz and a suppression for the two- and three-photon resonances around $f = 8$ THz and $f = 5.3$ THz. As pointed out above it is not clear from the outset that a numerical treatment reproduces the analytical results. The analytical treatment relies on the fact that the system is homogeneous and with domains already being in the system the behavior could be rather different.

Around the resonance frequencies the analytical results suggest that a rather small AC amplitude is sufficient to suppress the domains and this is preserved

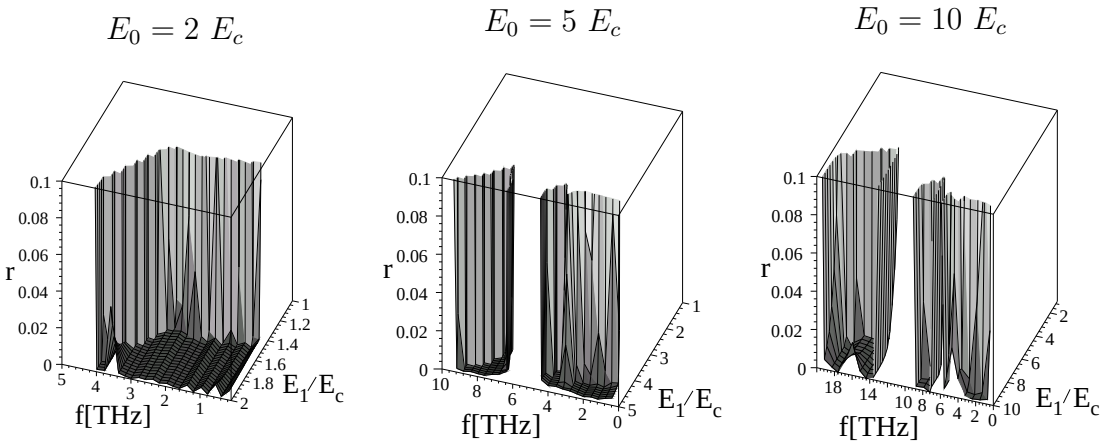

Fig. 3.9: *The relative change r of the electric field inside the superlattice if it is smaller than 0.1. It is plotted as a function of the applied frequency f and AC amplitude E_1 for three different DC fields E_0. The graphs are rotated with respect to Fig. 3.8 to improve the visibility of the regions where $r \approx 0$. For small frequencies one can see the domain suppression due to the LSA mode. For frequencies around $f = 1.6$ THz $\times E_0/E_c$ one can see the suppression of the domains via photon resonances.*

in the numerical results. Since it is numerically rather costly to wait for the possible formation of domains at each parameter point, the resolution is worse and fewer multiphoton resonances are observed. The interesting question that can be treated with the numerical model now is how the inclusion of boundaries modifies the results. It was already pointed out by Kroemer that it may be problematic to take advantage of the photon resonances, if the situation ceases to be homogeneous through the boundary effects. This question will be treated after the inclusion of the boundary model in section 3.2.

3.2 Inclusion of the boundaries

In this section the results for a superlattice with boundaries are presented. Two different models were introduced in Chapter 2 for the boundary region, but in this section mainly results for the discontinuous transition from the bulk material to the superlattice region are presented. The transition region extends usually only over several superlattice constants. In the simulation this region corresponds only to several points, and a finer grid in the transition region would be necessary to resolve the region. It is also questionable whether the assumption of a smooth transition is justified then. For the continuous transition it is also necessary

to introduce additional parameters like the doping profile and the band edge behavior in the transition region. These parameters are difficult to determine. The continuous model was therefore only used for the short superlattices with which higher harmonics are created (see table 3.2). As in the homogeneous case first the DC transport properties are investigated before the influence of external radiation is studied.

3.2.1 DC transport

It was explained in section 1.4.2 that depending on the field at the boundary one can distinguish two different scenarios: for subcritical field $E < E_c$ the resulting accumulation layers travel to the anode where a standing anode domain is formed and no oscillating behavior can be seen. For supercritical field $E > E_c$ at the boundary the resulting depletion layer merges with an accumulation layer to form a dipole domain which travels to the anode where it is annihilated and a new dipole domain is formed.

Since the contact voltage depends crucially on the difference of the chemical potentials in the contact region and the superlattice, I will first present the results for the standard superlattice if the lower edge of the lowest miniband is artificially shifted to higher and lower positions. The electric field at the boundary becomes larger in the first case which results in a higher applied voltage that is necessary to start the dipole domain. In the second case the electric field at the boundary becomes smaller which can lead to the disappearance of oscillations if $E < E_c$ at the boundary. In the real superlattices the contact field will depend on the exact design of the transition region. As will be seen the contact field resulting from the chemical potential difference changes drastically for only little changes in the lower edge of the miniband. Since the parameters of the superlattices like doping, well and barrier width will be known only approximately, the position of the lower edge of the miniband is known only approximately too.

In Fig. 3.10 the current-voltage curves are shown for the standard superlattice with a band edge difference of $\varepsilon_{off}^0 = 130$ meV resulting from the Kronig-Penney model (b) and for a shift to a lower value of $\varepsilon_{off} = 105$ meV by 25 meV (a) and to a higher value of $\varepsilon_{off} = 155$ meV by 25 meV (c). Despite the small changes in band offset the changes in the behavior are quite dramatic. In the case where the miniband edge is lowered the small contact field introduces an accumulation that travels to the anode where it forms a static anode domain. In the other cases the high contact field leads to periodic behavior according to the mechanism described in section 1.4.2, if the voltage is high enough that the depletion layer detaches from the cathode. The voltage necessary for that is high for a raised miniband edge since there the electric field at the contact is higher. On the other hand the high contact field supports the formation of new dipole

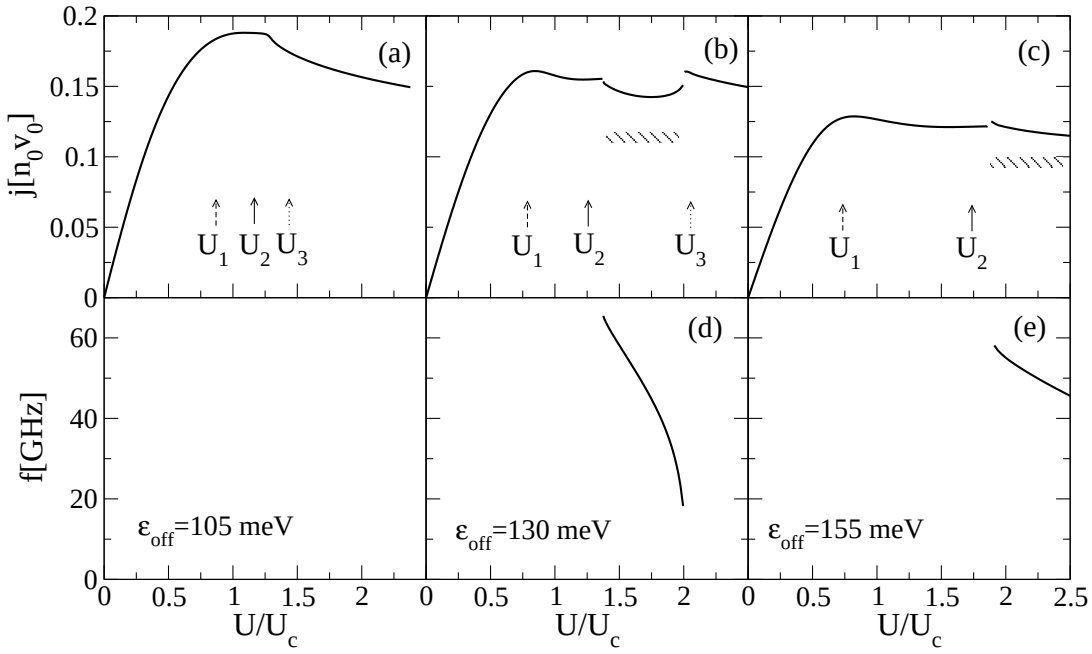

Fig. 3.10: *The current density j in units of $n_0 v_0$ and the oscillating frequency for the standard superlattice (Tab. 1.1) (b,d) and for the same superlattice if energy difference between the miniband edge and the conduction band edge in GaAs ε_{off} is shifted to a lower (a) or higher value (c,e). In the case of lowered miniband edge the electric field at the boundary is not sufficient to create a depletion layer and no oscillating behavior is observed. In the other two cases the electric field is sufficient to create domains which travel to the anode where they are annihilated and a new domains are formed (shaded regions). As could already be expected from the results for infinite superlattices the frequency drops with rising voltage. For the raised miniband edge a high voltage is necessary for the dipole domain to start propagating. Dashed (solid, dotted) arrows indicate voltage values for which the field distribution is shown in Fig. 3.11.*

domains when the old one reaches the anode. Therefore in this case even for high voltages oscillating behavior can be observed while in the case without shift a standing anode domain is formed for high voltages. The arrows indicate voltage values for which the electric field profiles are shown in Fig. 3.11.

The regions for which oscillating behavior is observed are indicated by the shaded regions in Fig. 3.10, and the respective frequencies are plotted below (d,e). In section 3.1 the frequency that would result from the drift velocity of the domains in infinite superlattices was shown. A strong decrease of the drift velocity with rising voltage was observed and this dependence becomes even stronger with boundaries since the annihilation of the domains at the anode takes more and

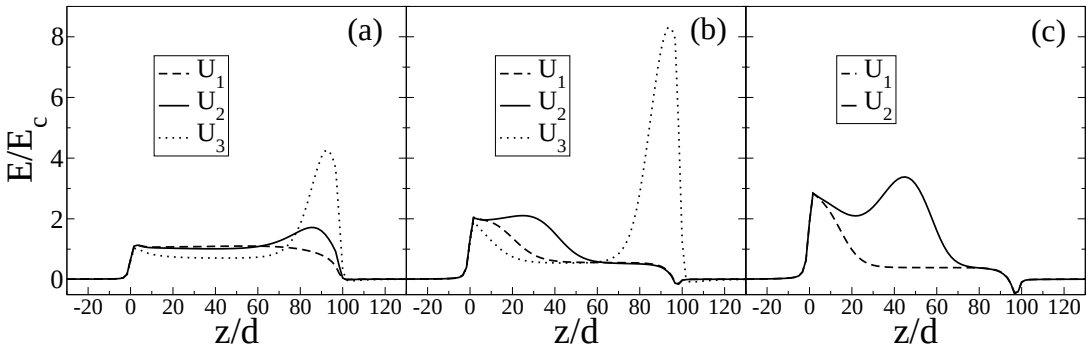

Fig. 3.11: *The field profiles for the voltage values U_i indicated by the arrows in Fig. 3.10 for the unshifted (b) and the lowered (a) and raised (c) miniband edge corresponding to Fig. 3.10. Dashed (solid, dotted) lines correspond to the dashed (solid, dotted) arrows in Fig. 3.10. (a) A standing anode domain forms in the unshifted case. (b,c) A depletion layer is formed which is traveling deeper and deeper into the superlattice for increasing voltage. Above the voltage U_2 the depletion merges with an accumulation and travels to the anode as dipole domain. A standing anode domain is formed above U_3.*

more time until the accumulation layer resides inside the superlattice above some voltage.

This strong dependence of the drift velocity and frequency from the voltage was also observed in simulations using an extended drift-diffusion model [Per04]. It is in striking contrast to the experimentally observed voltage dependence shown in Fig. 3.3. The frequency in the experiment is constant or nearly constant between two current jumps, while in the simulation it is rapidly changing with applied voltage. It is futile to reproduce the experimental frequencies of superlattices with the existing models as attempted in [Bon03] since with changing electric field a wide range of frequencies can be observed and any frequency inside this wide range can be reproduced at an appropriate voltage.

Fig. 3.11 shows the field profiles for the voltage values U_i indicated by the arrows in Fig. 3.10 for the unshifted (b) and the lowered (a) and raised (c) miniband edge corresponding to Fig. 3.10. Dashed (solid, dotted) lines correspond to the dashed (solid, dotted) arrows in Fig. 3.10. One can see how the standing anode domain forms if the field inside the superlattice becomes supercritical for voltages larger than U_2 for the lowered miniband edge. As soon as it is formed it continues growing for rising voltage, but a new domain is never formed. A depletion layer is formed for the unshifted and raised miniband edge which is traveling deeper and deeper into the superlattice for increasing voltage. In the field distribution it is indicated by the dropping field value. Above the voltage U_2 the depletion merges with an accumulation and travels to the anode as dipole domain. This

process is repeated until a standing anode domain is formed above U_3. For the raised miniband edge this voltage value is beyond the investigated voltage region.

Apart from the voltage dependence of the frequency a second large difference between the experiment and the simulation is that in the experiment several current jumps are observed. They are accompanied by jumps of the frequency and the emitted power. Therefore it seems that in the experiment there are different oscillation modes, while in the simulation only the dipole domain mode is observed. I will try to summarize the reasons that could be responsible for the discrepancies between simulation and experiment.

The main reason for the failure in reproducing the observed voltage dependence of the frequency may be the neglect of the surroundings, the description of which was attempted in section 2.3.1. One can easily imagine that the coupling of the superlattice device to a cavity with certain eigenfrequencies can lead to a locking of the frequency to one of the eigenfrequencies and therefore to a constant frequency as a function of the applied voltage. But even if that is an explanation for the constant frequency values over rather wide voltage ranges, the frequency should at least jump to lower values for increasing voltage, while the opposite is the case in the experiment.

In addition to that the jumps in the frequencies in the experiments are at most several per cent, while in the calculated curves the frequency changes by a factor of two from its highest to its lowest values. In fact the frequency drops to zero for increasing voltage since the anode domain requires more and more time to disappear and therefore the frequency goes to zero, but this happens in a tiny voltage range and is probably not a realistic assumption for the experiment. In all simulations for semiconductor superlattices that I know of the principle of microwave creation rests on the propagation of dipole domains and therefore the trend of dropping frequency with increasing voltage is observed. In my opinion the question why in the experiments the frequency is only weakly dependent on the voltage and often rises with increasing voltage remains unsolved up to now.

The other question that needs to be addressed is why there are more than two jumps observed in the experiments while in the calculations only two are found, where one indicates the transition to the oscillating state and the other one the transition to the state with the standing dipole domain. The number of jumps usually depends on the surrounding which indicates that again the main ingredient missing in the model is the surrounding of the superlattice device. To get an idea which effects can be seen if one includes an inductance in series with the superlattice device an inductance of 180 pH was placed in series with the superlattice device in the region with negative differential conductivity in Fig. 3.10a and b between the current peak (U_1) and the onset of the dipole domain oscillations (U_2). The inductance of 180 pH may be rather small for an actual circuit, but without additional damping the oscillations tend to have too

large amplitudes with higher inductances for the applied simulation procedure.

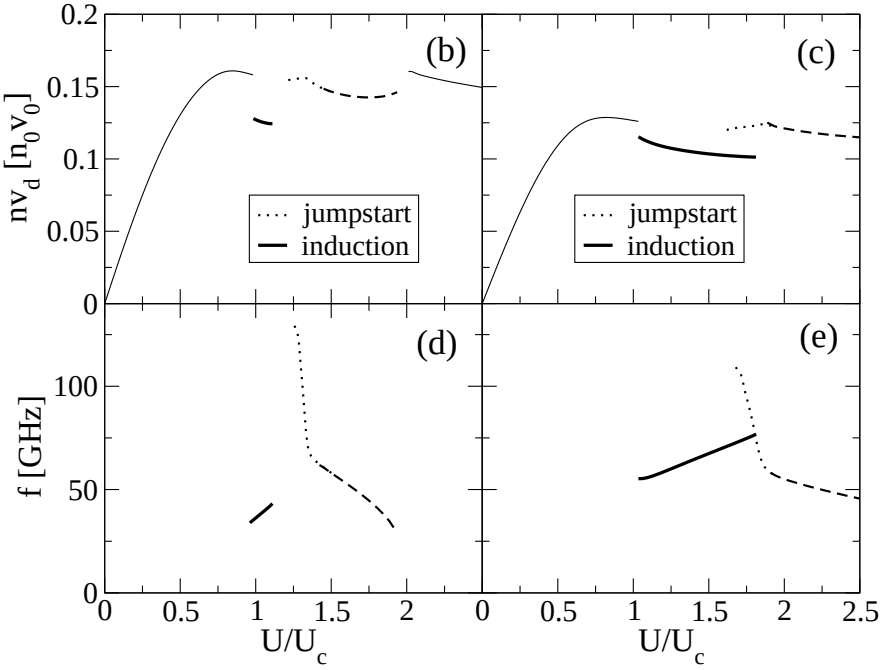

Fig. 3.12: *The current and frequency for the standard superlattice (b,d) and the same superlattice with miniband edge increased by 25 meV (c,e) if either an inductance is put in parallel (thick solid lines) with the superlattice or if the voltage is turned on in a steplike manner (dotted lines). The device can act as microwave source in the region with negative differential conductivity in which it is stable without the additional inductance. One can also produce oscillations if the voltage is turned on steplike and not smoothly (dotted lines). The observed frequencies are rather high then and drop rapidly with increasing voltage.*

Fig. 3.12 shows the calculated currents and frequencies of the oscillations that arise if an inductance (180 pH) is put in series with the superlattice (thick solid lines) for the standard superlattice (b,d) and for this superlattice with slightly increased value of the miniband edge (c,e). The frequencies can be calculated only up to the point where the current voltage curves from Fig. 3.10 become flat. Beyond the point where the current voltage curve of Fig. 3.10 becomes flat the numerical simulation becomes unstable with inductance. Then the oscillations tend to grow too much and a dissipation mechanism would be necessary to limit the growth.

This dissipation mechanism could be provided by inductively coupled resonance circuits with damping which are an equivalent description of a cavity as shown in section 2.3.2, but this mechanism was not included in the calculations. It turns

out that the frequency of the resulting current oscillations is strongly dependent on the inductance value, as one could probably expect, and therefore the absolute value of the frequency is maybe not to be taken seriously. It is difficult to make an estimate for the inductance in the measurements and the one used here is maybe a little too small. Nonetheless, it is interesting to see how even without the inclusion of the resonance circuits coupled to the inductance, which would give a full description of a surrounding cavity as shown in section 2.3.2, the behavior and the current voltage curve of the device are changed.

The oscillating state that is observed with inductance can be understood as follows. The formation of the depletion layer that is formed for high contact field quenches the current and therefore the inductance produces an additional voltage to maintain the current. The depletion grows and starts to propagate, but then the current starts being constant and the additional voltage by the inductance disappears and the dipole domain disappears. Unfortunately the amplitude of this process becomes large as the voltage is increased and diverges close to the point where the current voltage curve becomes flat. Beyond that point the simulation is stable only for much smaller inductance values, which are probably not realistic. While it is commonly accepted that dipole domain motion is a cause of microwave emission, it is not clear whether this oscillation type that is coupled to the inductance value is realized in the experiments. While the frequency of the dipole domain oscillations should be roughly proportional to the length, this oscillations should depend not only on the length but also on the inductance.

In the voltage region beyond the flat part of the current voltage curve in which the simulations were unstable with inductance it is also possible to observe oscillations. This happens if the voltage is turned on steplike and not smoothly. Then dipole domains will be formed which travel only a short distance into the superlattice before they are annihilated since the overall voltage is not sufficient to sustain the domains. This leads to oscillations with rather high-frequencies (dotted lines). This frequency drops rapidly with increasing voltage since the distance from the cathode at which the dipole domains are annihilated grows rapidly with voltage. The current and frequency curves merge finally with the quasistatic current voltage curves (dashed lines) from Fig. 3.10.

As already mentioned using an inductance only is a rather crude approximation of the circuit. For a full description of the surrounding a model would have to be devised for each experimental setup since the properties of a cavity in which the superlattice is situated described in section 2.3.2 is rather different from other measurement setups. One experimental possibility is to contact the superlattice from the top with a needle. The inductance of the needle can be estimated to be on the order of one nH. The influence of an inductance which has this order of magnitude was described above, but it is not clear, whether this model is sufficient to describe the experiments. At least a dissipation mechanism is

necessary since otherwise the oscillations become too large to be treatable by the numerical integration procedure.

Summing up the results of this section the following picture can be drawn. The model introduced in Chapter 2 has some advantages compared to previous models. Since a part of the contact region is included in the numerical simulation, it is not necessary to introduce a capacity parallel to the superlattice as in [Sch02a]. It is also not necessary to make ad hoc assumptions about the behavior of the contacts. The contact field follows from the difference in chemical potentials between the superlattice and the contact region. Other ad hoc assumptions like the introduction of a doping notch or statistical fluctuations of the doping density were tested, but none of them resulted in the creation of dipole domains and current oscillations if the contact field was subcritical. This is a difference to the Gunn diode simulations where these assumptions are usually sufficient to create dipole domains and to reproduce the experiments.

Unfortunately even the inclusion of a inductance in series with the superlattice is not sufficient to explain the experiments in superlattices. The rather wide voltage ranges with constant current oscillation frequencies suggest that the resonance frequencies of the environment are interacting with the oscillations of the superlattice. The inclusion of only an inductance gives a hint how this interacting mode could look like, but to get a conclusive picture a full description of the current circuit and cavities is necessary which was not achieved in this work. Nonetheless, the inclusion should be rather straightforward and might be a project for future research if further understanding is necessary for the development of high-frequency devices.

An advantage of the solution of the Boltzmann equation compared to the drift-diffusion model is that for frequencies beyond $f \ll 1/2\pi\tau \approx 1$ THz the drift-diffusion model becomes unrealistic. Sometimes microwave radiation at frequencies around several hundred GHz is applied to the superlattices and therefore one needs to go beyond the drift-diffusion model. In the next section the results for interaction with high-frequency radiation are presented.

3.2.2 Interaction with external radiation

The results of the last section suggest that the model developed in Chapter 2 still lacks some crucial ingredients to arrive at a model which can reproduce the experimental results. In spite of this it is attempted in this section to understand which processes set in when microwave radiation is shined on the superlattices. Two effects have been described in section 3.1.2, frequency multiplication and domain suppression. It is attempted here to understand which effects the boundaries have in these modes.

Frequency multiplication

In section 3.1 the creation of higher harmonics upon high-frequency irradiation was shown for a periodic system. Now we can extend the considerations to superlattices with boundaries. Intuitively one expects that the formation of domains happens faster since the domains need not grow out of small fluctuations but can develop at the boundaries also. The applied frequency can now be as high as 100 GHz for the standard superlattice and for the highly doped superlattice (Tab. 3.2) this frequency is also used. Fig. 3.13 shows the amplitude of the third harmonic as a function of the applied voltage. Since a fraction of the applied voltage drops at the boundaries, the curve lies below the curve for the superlattice with boundary. Of course the field is due to the boundaries not given by U/L, but the curves are still plotted with respect to the field that corresponds to the applied voltage $E = U/L$ in the homogeneous case to make a comparison with the earlier calculations possible.

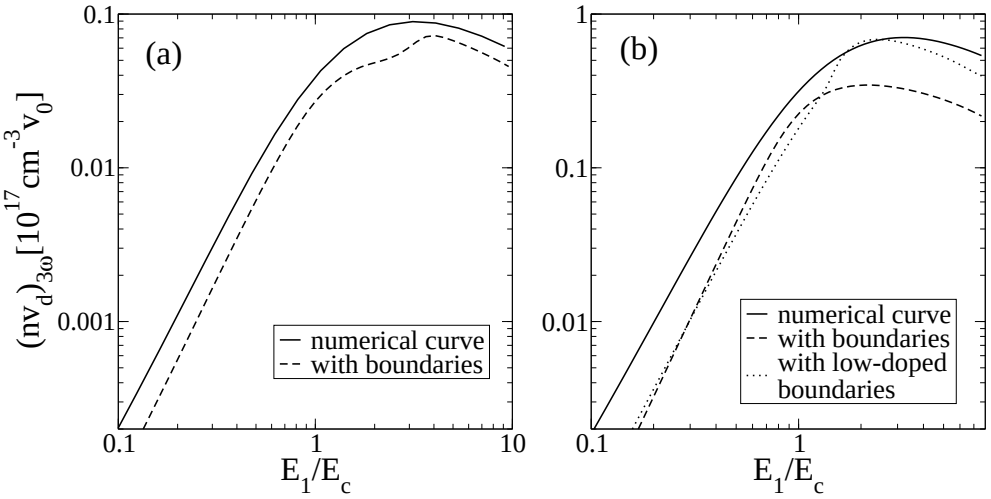

Fig. 3.13: *Amplitude of the third harmonic of nv_d as a function of the irradiation amplitude E_1 for the standard superlattice (a) and for the superlattice from Tab. 3.2 (b). With boundaries the amplitude increases appreciably for the standard superlattice as soon as the the domain formation sets in for $E_0 = 2.5\ E_c$ (dashed line). For the highly doped superlattice this is only observed if the doping in the boundaries is lowered (dotted line) compared to the experimental value of the doping (dashed line).*

In Fig. 3.13a one can see that the amplitude of the third harmonic rises above $E_1 = 2.5\ E_c$. This is the point where the creation of domains sets in. For the highly doped superlattice one encounters the problem that the chemical potential in the superlattice is lower than in the boundaries due to the high doping level in the boundary region ($6\times10^{18}/cm^3$). This produces a negative contact voltage and

the domains form at the anode where the field is already high in the unbiased case instead of the cathode (Fig. 3.14, dashed curves). One cannot determine a certain point where domain formation sets in, the process is rather smooth and therefore no structure can be seen in the dashed harmonics amplitude (Fig. 3.13b). If the doping in the boundaries is lowered to $n = 4 \times 10^{18}/\mathrm{cm}^3$, the contact voltage becomes positive at the cathode and one can see a rise of the amplitude of the third harmonic when the domain formation sets in slightly above E_c (dotted curve).

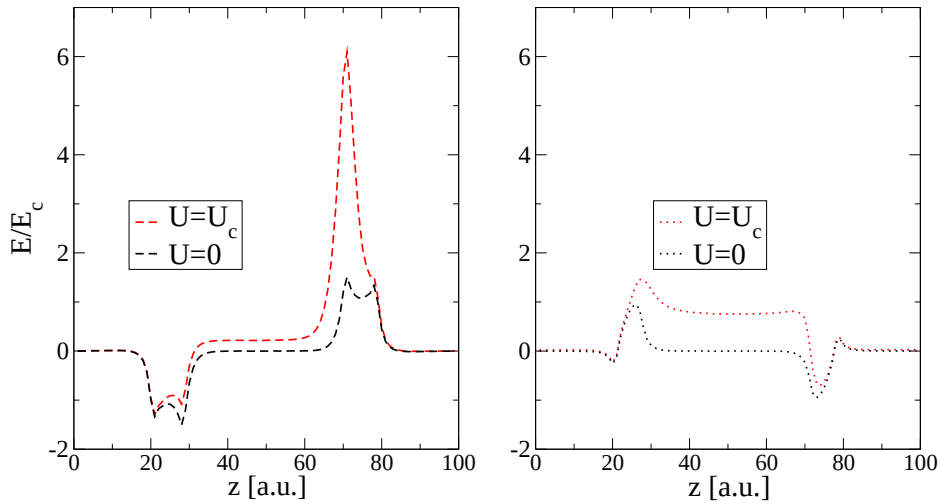

Fig. 3.14: *The field profiles for the highly doped superlattice from Fig. 3.5b for a doping of* $n = 6 \times 10^{18}/\mathrm{cm}^3$ *(left side) and* $n = 4 \times 10^{18}/\mathrm{cm}^3$ *(right side) in the boundaries for zero (black) and critical (grey) applied voltage. In the first case an anode domain develops, while in the second case a depletion layer is created at the cathode.*

In Fig. 3.14 the field profiles for the highly doped superlattice of Fig. 3.5b are plotted for the experimental doping value (left side) and a lower doping value (right side) in the boundaries. For the doping that was used in the experiment the contact field is negative and no dipole domains are produced, only an anode domain can be observed which grows with increasing voltage. In the simulation the chemical potential can be artificially lowered in the boundary region by reducing the doping. The contact field is supercritical then and a depletion layer is formed which finally develops into a dipole domain.

In a frequency multiplication experiment using a superlattice with the parameters in Tab. 3.2 an increase of the emitted power by an order of magnitude was observed at a certain input power and was attributed to the onset of domain formation [Kla04a]. The results of the simulation indicates that the onset of domain creation indeed increases the output power at the third harmonic frequency,

but the increase by an order of magnitude cannot be reproduced. A mechanism enhancing the emitted radiation suddenly could be coupling of the emitted radiation to a surrounding cavity which then produces also irradiation at the third harmonic. That additionally produces radiation at the third harmonic which is resonantly enhanced by this mechanism. A conclusive answer to the question whether this is the cause of the sudden onset or whether it is just the onset of domain formation cannot be given at this point.

Domain suppression

In Chapter 1 we introduced a mechanism that was capable of suppressing domains when high-frequency radiation is shined onto the superlattices: the LSA mode that was initially suggested for Gunn diodes and extended by Kroemer to frequencies above the inverse scattering time. It was shown that the numerical treatment reproduces for a system with periodic boundary conditions the analytical results. Now the calculations are repeated with boundaries to see whether the low-frequency stability can also be observed in this case.

We use again the relative change $r = \frac{E_{max}-E_{min}}{E_{average}}$, with obvious definitions of the quantities, as a convenient measure for the homogeneity. Even if the differential mobility is positive and the system is perfectly stable there will be inhomogeneities at the boundaries, therefore r will not be close to zero even if the superlattice is homogeneous. I considered the first and last ten wells of the superlattice structure as boundary regions and did not consider them for the calculation of r.

Fig. 3.15 shows r as a function of the applied frequency f and amplitude E_1 for different DC fields. One can see that in the region $f < 1/2\pi\tau = 1.6$ THz and $E_1 > E_0 - E_c$, where the classical LSA mode description applies, the positive mobility leads to a homogeneous situation ($r < 0.2$) in the case $E = 2\ E_c$ also when the boundaries are included. In the classical LSA regime one also observes a rather homogeneous state ($r < 0.5$) for $E = 5\ E_c$, but for $E = 10\ E_c$ the electric field becomes hardly homogeneous for any set of parameters f and E_1. In the resonance regions $f = 1.6$ THz $\times E_0/E_c$ in which the superlattices without boundaries were homogeneous even for small AC amplitudes E_1 one can see only a slight suppression of the field inhomogeneity in the superlattice, but a value of $r > 2.5$ corresponds to a well developed domain inside the superlattice. The proposition of Kroemer to take advantage of those resonances may therefore not be possible in the experiment. One has to resort to the regime of the originally proposed LSA mode.

On the other hand one problem of the numerical simulations was the fact that for frequencies above 4 THz a large fraction of the oscillating field dropped in the boundary region. The reason for that is not fully clear and further investigations

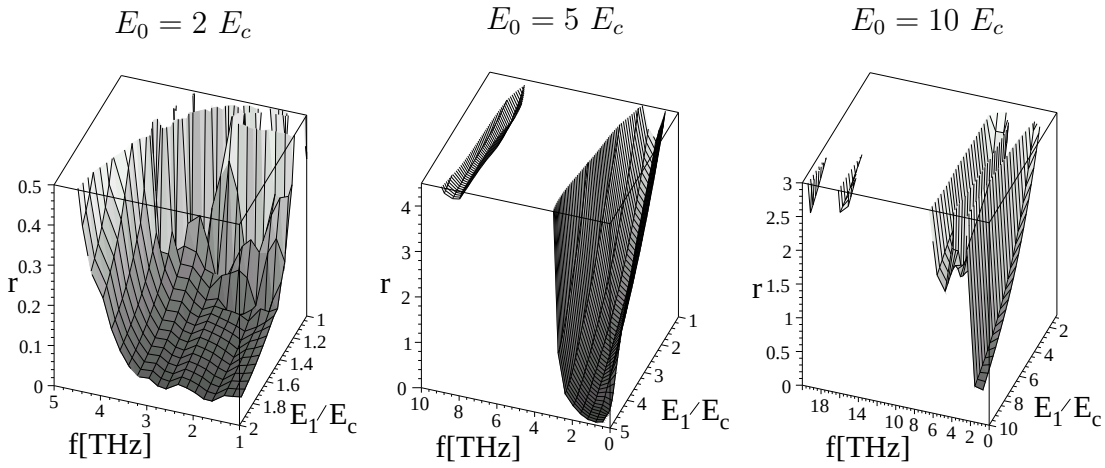

Fig. 3.15: *The relative change r of the electric field as a function of frequency f in THz and amplitude E_1 in units of E_c for different applied DC fields E_0. The range of r is magnified compared to Fig. 3.9 since in the parameter regions with positive differential conductivity the domain formation is slightly suppressed, but the superlattice is not homogeneous.*

are necessary to decide whether this is reasonable. This shielding of the high-frequency radiation from the superlattice is a reason for the fact that the domains cannot be suppressed for those large frequencies. If it turns out that this scenario is unrealistic, it may in the end be possible to work also in the extended LSA mode.

To summarize, the results presented in this chapter indicate that the rather elaborate model developed in Chapter 2 is not yet sufficient to explain the observed behavior in detail. Nevertheless many phenomena could be found with it and it is possible to determine which process could be responsible for the observed behavior. The inclusion of the boundary region is a major step towards a realistic description since the interesting phenomena in the superlattices, like microwave emission and frequency multiplication, are all caused by processes at the boundaries. The calculations indicate where inhomogeneities can form and how they propagate, but it seems to be necessary to include the interaction with the surrounding to observe additional modes that seem to give the complicated structure of the measured curves. Some proposals how to suppress the domains have been recently put forward and with the developed model it can be tested whether the mechanisms which are often predicted for homogeneous systems persist under realistic boundary conditions.

Chapter 4

Summary and Outlook

4.1 Summary

In this thesis the transport properties of semiconductor superlattices under the influence of DC and AC fields were investigated using a semiclassical model of the electron dynamics. A model for the boundary region between the superlattice and the bulk medium was developed and its influence on the properties was studied.

Method

The starting point of a semiclassical treatment of the electron dynamics in semiconductors is the Boltzmann equation which describes the time evolution of the electron distribution f in phase space. It was shown [Wac02] that for the superlattice parameter regime that is considered in this thesis the quantum mechanical description reduces to this semiclassical model. For inhomogeneous semiconductor samples the Monte Carlo method is widely used to solve the Boltzmann equation [Jac83]. However, the Monte Carlo method is numerically rather costly and requires knowledge of the microscopic scattering probabilities. A major simplification is the relaxation time approximation which summarizes the effect of the scattering events under the assumption that they tend to restore the equilibrium distribution f_0.

While giving up the possibility of a precise quantitative description of the system, the differential equation can now be solved numerically via a discretization procedure. The canonical way of simplifying the equation further is to go to the moment-balance equations which describe the time evolution of averaged quantities $\langle a \rangle = \int f(k)a(k)dk$. The final simplifying step is then the derivation of the drift-diffusion model which had been used previously to describe transport in semiconductor superlattices [Bon03, Sch02b]. Unfortunately, the last step is valid only if relaxation processes are faster than the external or internal dynamics in

the samples which will not be the case for applied high-frequency fields or fast-moving inhomogeneities. In addition to that, it is difficult to derive boundary conditions at the interface between the superlattice and the bulk semiconductor material for the moment-balance equations and the drift-diffusion model.

The boundary conditions in semiconductor superlattices are crucial for the behavior since the transport is suppressed above some critical field E_c resulting in negative differential conductivity (NDC). It was already realized in the late 1960's that the boundary conditions are crucial for the behavior in NDC materials since the materials are unstable with respect to the formation of inhomogeneities. Either fluctuations inside the sample or discontinuities at the boundaries will be the nucleation points of charge accumulation or depletion layers which travel through the system. When the layers approach the boundaries of the system the boundary conditions determine whether they will disappear or form stable charged layers.

The boundary conditions for the Boltzmann equation can be formulated for a discontinuous and a continuous transition from the superlattice to the bulk material starting from nonequilibrium Green functions in the first and from a tight-binding ansatz in the second case. Only the superlattice parameters enter the model, in contrast to earlier models where ad hoc assumptions about the boundaries were used to produce behavior that is in agreement with the experiment. The self-consistent solution of the boundary region suggests to consider tunneling processes through the triangular barriers which form at the beginning and at the end of the superlattice region. These processes were included in our calculations. The discontinuous model was used for the boundaries in nearly all cases in the simulations since the transition region cannot be resolved for the grid spacing that was used in the calculations.

The next step towards a realistic description is the inclusion of the current circuit and the superlattice surrounding which is necessary since the moving charge layers create high-frequency currents and radiation which will couple to the resonant properties of the surrounding. A model for the current circuit and a surrounding cavity was developed. However, only the circuit was implemented numerically since the equivalent description of a cavity results in a rather complicated model and the inclusion of an inductance in the current circuit already produced divergences caused by oscillating behavior with increasing amplitude.

Results

To separate the influence of the boundaries from the properties of the superlattices we first investigated the properties of artificial superlattices with periodic boundary conditions so that the system is homogeneous without applied field. All three semiclassical approaches, the Boltzmann equation, the moment-balance

equations, and the drift-diffusion model were solved numerically and the results compared. For voltages larger than the critical voltage $U_c = E_c L$ a traveling dipole domain is formed in all three cases as was already observed in earlier drift-diffusion simulations. The shape and velocity v_{dom} of the domain is similar in all cases. The Boltzmann equation has a stronger diffusion effect and the domain is broader.

From the drift velocity one can extract the time $t_0 = L/v_{dom}$ that is needed for one cycle of the periodic motion of the dipole domain through the superlattice. This time depends strongly on the applied voltage in the simulation and drops by as much as 20 per cent if one increases the voltage from 1.5 U_c to 2 U_c (Fig. 3.2). In contrast to that, in the experiment the frequency is constant within large voltage intervals. It jumps to larger values for increasing voltage, but the frequency values usually change only by several per cent. While locking to a resonance frequency provided by the surrounding could be an explanation for the constant frequency intervals, it is not clear why the frequency rises slightly while it drops strongly in the simulations.

Having established a comparison of the different semiclassical models for DC transport, the behavior under external radiation was investigated as a next step. Since the drift-diffusion model is not a good description for high-frequency properties and the solution of the moment-balance equations was unstable for large applied electric fields, these calculations were done only with the Boltzmann equation. One can separate three different regimes if a high-frequency electric field is applied. As a result, totally different questions can be investigated.

For vanishing DC voltage one can create higher harmonics due to the nonlinearity of the relation between the drift velocity and the electric field. Especially the onset of domain formation for AC fields $E_1 > E_c$ is expected to influence the amplitude of higher harmonics. This is indeed the case in the calculations where the amplitude of the third harmonic rises when domains are allowed to form compared to the homogeneous case (Fig. 3.5). The formation of domains is of course strongly influenced by the presence of boundaries which will be discussed later.

The change in the current density-voltage relation when the superlattice is irradiated is the next interesting feature. The peak current density is suppressed and moves to higher voltages if the superlattice stays homogeneous [Ign95]. If the superlattice is sufficiently long in the supercritical field region during one high-frequency cycle, the formation of domains may on the other hand be possible for subcritical DC voltages, leading to a current suppression for subcritical voltages. For large applied frequencies we could observe the first case where the maximum shifts to the left while for small applied frequencies the second case where the maximum shifts to the right was observed (Fig. 3.6). It was experimentally attempted to determine the time of domain formation by determining the frequency

above which the maximum shifts to the left [Kla04]. The frequency of 3 THz determined there was much larger than the frequency of 200 GHz determined in our simulations for the homogeneous superlattices. This is no contradiction since the formation of domains from fluctuations in the homogeneous case will take much longer than the formation in superlattices with boundaries. We did not attempt to investigate the situation in superlattices with boundaries since with boundaries the situation is already rather complicated in the pure DC case (Fig. 3.10) and it is questionable whether the experimental situation is modeled well enough to allow predictions around the current peak including an AC field.

It has been first derived by Ktitorov *et al.* [Kti72] that the negative differential conductivity for supercritical field $E > E_c$ persists up to the Bloch frequency which is typically on the order of several Terahertz. The problem in taking advantage of this gain mechanism for the design of a microwave emitter is the instability with respect to domain formation. In the LSA mode of operation proposed by Copeland for Gunn diodes [Cop66] the domains are suppressed by the incident radiation that is supposed to be enhanced. A generalization of this mechanism to higher frequencies was proposed for superlattices by Kroemer [Kro00a]. A crucial question for the applicability of this mechanism is whether the domains can be suppressed in a real device.

We have, therefore, in a third step investigated the behavior of a supercritically biased system with periodic boundary conditions under the influence of external radiation to see for which parameters the system will be homogeneous. It is not clear from the outset that this region coincides with the region for which positive differential conductivity was proposed from the homogeneous model, but good agreement has been found. The next step is the inclusion of boundaries which introduce inhomogeneities so that one expects that the homogeneity is less probable to persist. Before the results of this are presented the DC properties of superlattices with boundaries are described.

With boundaries one can calculate the current density-voltage relation and compare it to the experimental curves. The result depends strongly on the exact boundary model which again supports the assumption that the boundary conditions are crucial for the behavior. The best agreement with the experimental curves can be observed if the electric field at the cathode is slightly supercritical. If it is smaller, anode domains are formed and no oscillations are observed. If it is larger, the oscillations do not set in before the applied voltage is very high. The frequency is even more voltage dependent than without boundaries which makes the agreement with the experiment, where the frequency is only slightly voltage dependent, even worse. In addition to that, the voltage region in which periodic behavior can be observed is rather small compared to the experiment.

This region can be extended if one introduces an inductance, which models the experimental setup, in series with the superlattice. Unfortunately, the simulation

was only stable in a small region where self-sustained oscillations were not observed since otherwise the results diverged. Another way of extending the region with oscillations is the application of a voltage jump. This jump introduces fluctuations which support the detachment of the depletion layer from the cathode. Even with both mechanisms the experimental observations cannot be explained.

The suppression of the domains via external radiation for supercritical applied field was only possible for frequencies below 4 THz if boundaries are introduced. The reason is that for frequencies above this value the oscillating field drops in the boundary region and not in the superlattice so that the domain formation is not suppressed in the superlattice. It is not clear whether this is physically reasonable or an artefact of the simulation algorithm.

4.2 Outlook

The discrepancy between the experimentally measured and calculated dependence of the frequency on the applied voltage suggests that a crucial ingredient is still missing in the attempt to model the experimental setup. Several simplifying steps were undertaken to arrive at a model which is numerically tractable and in the following we try to assess the validity of the simplifications.

The usage of the semiclassical transport model is a good approximation if $a := \tau\Delta/2\hbar \gg 1$ and $E/E_c \ll a$ [Wac02]. Since $a \approx 5$ for our standard superlattice, these requirements are fulfilled if the field enhancement inside the dipole domain is not too strong. The lateral dimensions of the superlattice structure are usually several μm and the length of the superlattice is below one μm so that the assumption of homogeneity in the lateral directions is also reasonably well fulfilled. The boundary models developed in this thesis may not be adequate to describe the transition region. The reason may be the lack of knowledge about the exact microscopic structure. Since minor adjustments in the boundary have a huge effect on the results of the calculations, we may not possess a sufficiently exact knowledge of the crystal structure in the boundary region where diffusion of doping atoms and other processes might obscure the desired superlattice design.

The most severe simplification may be the neglect of the surrounding. The strongest evidence for that is the existence of rather large voltage regions in which the emitted frequency is constant. The coupling of the superlattice to the surrounding, which provides different resonance frequencies to which the frequency of the superlattice locks, could be the reason for this. We have presented a model which describes the influence of a surrounding cavity, but the numerical implementation was not achieved since already the inclusion of an external inductance caused numerical difficulties.

It seems that for the development of a device relying on the gain mechanism proposed by Ktitorov a sufficiently precise model including the boundary region would be extremely helpful. An analytical solution of the time-dependent inhomogeneous problem is very difficult, if not impossible, so that one has to resort to numerical methods. Since a Monte Carlo solution of the full Boltzmann equation is rather costly and in my opinion not necessary, the model developed in this thesis seems to be a good candidate for that purpose.

The rapidly emerging field of Terahertz technology asks for the development of a cheap and small solid state source in that frequency range. Since it may not be possible to enter the Terahertz regime with quantum cascade laser technology at room temperature, the superlattices are a suitable candidate if one overcomes the problem of the inhomogeneities. There have been several proposals over the last few years how to avoid the inhomogeneities [Fei04, Sav04, Kro00a, Ryn03] which shows that, despite the fact that the original ideas are more than thirty years old, there are still emerging new design ideas. It remains to be seen whether the Bloch laser will be finally realized.

Appendix A

Derivation of the driving term in the Boltzmann equation

Consider a one-dimensional Hamiltonian[1]

$$H(x) = -\frac{1}{2m}\frac{\partial}{\partial x^2} + V(x) + U(x) \; . \tag{A.1}$$

$V(x)$ is a quasiperiodic function with periodicity length d and varies slowly on the length scale of several lattice constants d. We write the quasiperiodic potential in the form

$$V(x) = f(x)\tilde{V}_p(x) \tag{A.2}$$

as a product of a slowly varying function $f(x)$ and a periodic potential $\tilde{V}_p(x)$. $U(x)$ is a slowly varying external potential. Around some expansion point $\bar{x}$ the Hamiltonian can locally be written as

$$H_p(x,\bar{x}) = -\frac{1}{2m}\frac{\partial}{\partial x^2} + f(\bar{x})\tilde{V}_p(x) + U(x) \; . \tag{A.3}$$

$H_p(x,\bar{x})$ is the Hamiltonian with a potential $V_p(x,\bar{x}) := f(\bar{x})\tilde{V}_p(x)$ that resembles the local potential around $\bar{x}$, but this potential extends over the whole lattice. The Hamiltonian is then

$$H(x) = H_p(x,\bar{x}) + \delta V(x,\bar{x}) + U(x) \tag{A.4}$$

with

$$\delta V(x,\bar{x}) = V(x) - V_p(x,\bar{x}) = (f(x) - f(\bar{x}))\tilde{V}_p(x) = \delta f(\bar{x})\tilde{V}_p(x) \; . \tag{A.5}$$

$\delta V(x,\bar{x})$ is close to zero around the expansion point $\bar{x}$ in a region that extends over several lattice periods d. One can define a Bloch basis $\varphi_{nk}(x,\bar{x}) = u_{nk}(x,\bar{x})e^{ikx}$ of eigenstates for each expansion point $\bar{x}$ for the Hamiltonian $H_p(x,\bar{x})$

$$H_p(x,\bar{x})\varphi_n(k,\bar{x}) = \varepsilon_n(k,\bar{x})\varphi_n(k,\bar{x}) \; . \tag{A.6}$$

[1] Planck's constant $\hbar = 1$ in this Appendix

From the difference of the Dyson equations one gets

$$\left[i\frac{\partial}{\partial T} - (H(x_1) - H(x_2))\right] G(x_1, x_2, \omega, T) = 0\ . \tag{A.7}$$

For our Hamiltonian $H(x)$ this equals to

$$\left[i\frac{\partial}{\partial T} - (H_p(x_1,\bar{x}) + \delta V(x_1,\bar{x}) + U(x_1) - H_p(x_2,\bar{x}) - \delta V(x_2,\bar{x}) - U(x_2))\right] \tag{A.8}$$
$$G(x_1, x_2, \omega, T) = 0\ .$$

Inserting the definition

$$G(x_1, x_2, \omega, T) = \sum_{nn'kk'} \varphi_{nk}(x_1,\bar{x})\varphi^*_{n'k'}(x_2,\bar{x}) G(nk, n'k', \omega, T, \bar{x}) \tag{A.9}$$

in the equation above we get

$$\begin{aligned} &i\frac{\partial}{\partial T} G(nk, n'k', \bar{x}) - (\varepsilon_n(k,\bar{x}) - \varepsilon_{n'}(k',\bar{x}))\, G(nk, n'k', \bar{x}) - \\ &- \sum_{n_1k_1} [\langle nk|\delta V|n_1k_1\rangle G(n_1k_1, n'k', \bar{x}) - G(nk, n_1k_1, \bar{x})\langle n_1k_1|\delta V|n'k'\rangle] - \\ &- \sum_{n_1k_1} [\langle nk|U|n_1k_1\rangle G(n_1k_1, n'k', \bar{x}) - G(nk, n_1k_1, \bar{x})\langle n_1k_1|U|n'k'\rangle] = 0, \end{aligned} \tag{A.10}$$

where the arguments ω and T are suppressed and the definitions

$$\langle nk|\delta V|n'k'\rangle = \int_0^L \varphi^*_{nk}(x',\bar{x})\delta V(x',\bar{x})\varphi_{n'k'}(x',\bar{x})dx' \tag{A.11}$$

and

$$\langle nk|U|n'k'\rangle = \int_0^L \varphi^*_{nk}(x',\bar{x})U(x')\varphi_{n'k'}(x',\bar{x}))dx' \tag{A.12}$$

were used. The Green function is transferred to a local Wannier basis with the definition

$$G(n, n', x_1, x_2) = \frac{1}{N}\sum_{k,k'} G(nk, n'k', \bar{x}) e^{ikx_1} e^{-ik'x_2}, \tag{A.13}$$

where the Wannier states centered around the site x_0 in a periodic lattice are given by the definition

$$a_n(x - x_0) = \frac{1}{\sqrt{N}} \sum_{k\in BZ} e^{-ikx_0}\varphi_{nk}(x)\ . \tag{A.14}$$

With the definition

$$H_p(n, x_1, x_2) = \frac{1}{N}\sum_{k\in BZ} \varepsilon_n(k) e^{ik(x_1-x_2)}\ , \quad i = 1, 2 \tag{A.15}$$

the energy terms in Eq. (A.10) can be transformed

$$A := \sum_{k,k'} \left(\varepsilon_n(k) - \varepsilon_{n'}(k')\right) G(nk, n'k') e^{ikx_1} e^{-ik'x_2} = \quad \text{(A.16)}$$

$$= \sum_{x_3} \left(H_p(n, x_1, x_3) G(n, n', x_3, x_2) - H_p(n', x_3, x_2) G(n, n', x_1, x_3)\right) \ . \quad \text{(A.17)}$$

In an analogous way the Fourier transform of the potential term in Eq. (A.10) can be written as

$$B := \sum_{n_1 x_3} S(n, n_1, x_1, x_3) G(n_1, n', x_3, x_2) - S(n_1, n', x_3, x_2) G(n, n_1, x_1, x_3) \ , \quad \text{(A.18)}$$

with the definition

$$S(n, n', x_1, x_2) := \frac{1}{N} \sum_{kk'} \langle nk|U|n'k'\rangle e^{ikx_1} e^{-ik'x_2} \ . \quad \text{(A.19)}$$

Now use the properties of the Wannier states. $S(n, n', x_1, x_2)$ describes the overlap of two Wannier functions centered around x_1 and x_2 folded with the potential U. Only if the distance $x_1 - x_2$ between the two Wannier function centers is on the order of several lattice constants both functions will have a finite overlap. In the overlap region, which extends only over several lattice constants around $X := (x_1 + x_2)/2$, the potential can be approximated by $U(x) = U(X) + U'(X)(x - X)$. We get with this

$$S(n, n', x_1, x_2) = U(X)\delta_{n,n'}\delta(x_1 - x_2) + \frac{1}{N} \sum_{kk'} U'(X) \langle nk|(x - X)|n'k'\rangle e^{ikx_1 - ik'x_2} \ . \quad \text{(A.20)}$$

Now we use

$$\begin{aligned} \varphi^*_{nk}(x) x \varphi_{n'k'}(x) \ &= \ \frac{1}{2} \left(i \frac{\partial \varphi^*_{nk}}{\partial k} \varphi_{n'k'} - i \frac{\partial u^*_{nk}}{\partial k} e^{-ikx} \varphi_{n'k'} + \right. \\ &\quad \left. + i \varphi^*_{nk} \left(\frac{\partial u_{n'k'}}{\partial k'} \right) e^{ik'x} - i \varphi^*_{nk} \frac{\partial \varphi_{n'k'}}{\partial k'} \right) \end{aligned} \quad \text{(A.21)}$$

to simplify the term

$$\begin{aligned} \langle nk|x|n'k'\rangle \ &= \ \frac{i}{2} \int_0^L \left(u^*_{nk}(x') \frac{\partial u_{n'k'}}{\partial k'}(x') - \frac{\partial u^*_{nk}}{\partial k}(x') u_{n'k'}(x') \right) e^{i(k'-k)x'} dx' - \\ &\quad - \frac{i}{2} \int_0^L \left(\varphi^*_{nk}(x') \frac{\partial \varphi_{n'k'}}{\partial k'}(x') - \frac{\partial \varphi^*_{nk}}{\partial k}(x') \varphi_{n'k'}(x') \right) dx' \ . \end{aligned} \quad \text{(A.22)}$$

$u^*_{n'k'}(x', \bar{x}) \frac{\partial u_{nk}}{\partial k}(x', \bar{x})$ and $\frac{\partial u^*_{nk}}{\partial k}(x') u_{n'k'}(x')$ are periodic in the lattice and therefore the first integral vanishes unless $k = k'$. The second term can be simplified with

a partial integration to get altogether

$$\langle n_1 k|(x-X)|n'k'\rangle = i\delta_{k,k'}X_{n,n'}(k) + \delta_{n,n'}\delta_{k,k'}\left[\frac{i}{2}\left(\frac{\partial}{\partial k'} - \frac{\partial}{\partial k}\right) - X\right] , \quad \text{(A.23)}$$

with $X_{n,n'} = \frac{1}{2}\int_0^L \left(u^*_{nk}(x')\frac{\partial u_{n'k}}{\partial k}(x') - \frac{\partial u^*_{nk}}{\partial k}(x')u_{n'k}(x')\right)dx'$. The term $X_{n,n}(k)$ is only an energy shift for the n-th band and will be neglected in the following. Now get for S

$$S(n,n',x_1,x_2) = U(X)\delta_{n,n'}\delta(x_1-x_2) + \frac{1}{N}\sum_{k\in BZ} iU'(X)X_{n,n'}(k)e^{ik(x_1-x_2)} . \quad \text{(A.24)}$$

Get for the periodic potential term in Eq. (A.10)

$$C := \sum_{n_1 x_3} F(n,n_1,x_1,x_3)G(n_1,n',x_3,x_2) - F(n_1,n',x_3,x_2)G(n,n_1,x_1,x_3) \quad \text{(A.25)}$$

with the definition

$$F(n,n',x_1,x_2) := \frac{1}{N}\sum_{kk'}\langle nk|\delta V|n'k'\rangle e^{ikx_1}e^{-ik'x_2} . \quad \text{(A.26)}$$

The same reasoning as for S leads to

$$\langle nk|(x-X)\tilde{V}_p|n'k'\rangle_{\bar{x}} = i\delta_{k,k'}X^{V_p}_{n,n'}(k) + \langle nk|\tilde{V}_p|n'k\rangle\delta_{k,k'}\left[\frac{i}{2}\left(\frac{\partial}{\partial k'} - \frac{\partial}{\partial k}\right) - X\right] . \quad \text{(A.27)}$$

and

$$\begin{aligned} F(n,n',x_1,x_2) &= \delta f(X)\frac{1}{N}\sum_k \langle nk|\tilde{V}_p|n'k\rangle e^{ik(x_1-x_2)} + \\ &\quad \frac{1}{N}\sum_{k\in BZ} i\delta f'(X)X^{V_p}_{n,n'}(k)e^{ik(x_1-x_2)} \end{aligned} \quad \text{(A.28)}$$

with $X^{V_p}_{n,n'} = \frac{1}{2}\int_0^L \tilde{V}_p(x')\left(u^*_{nk}(x')\frac{\partial u_{n'k'}}{\partial k'}(x') - \frac{\partial u^*_{nk}}{\partial k}(x')u_{n'k'}(x')\right)dx'$. $X^{V_p}_{n,n}$ is again only an energy shift and will be neglected.

Further define central and relative coordinates and the Fourier transform

$$A(p,X) = \sum_{(x_1+x_2)/2=X} A(x_1,x_2)e^{-ip(x_1-x_2)} . \quad \text{(A.29)}$$

With the help of the gradient expansion

$$C(p,X) = A(p,X)B(p,X) - \frac{i}{2}(\partial^A_p\cdot\partial^B_X - \partial^A_X\cdot\partial^B_p) \quad \text{(A.30)}$$

for a folded function

$$C(x_1, x_2) = \sum_{x_3} A(x_1, x_3) B(x_3, x_2) \tag{A.31}$$

we get

$$\sum_x \left[\sum_{x_3} H_p(n, X + x/2, x_3) G(n, n', x_3, X - x/2) \right] e^{-ipx} \approx \tag{A.32}$$

$$\varepsilon_n(p) G(n, n', p, X) - \frac{i}{2} \frac{\partial \varepsilon_n(p)}{\partial p} \frac{G(n, n', p, X)}{\partial X} \tag{A.33}$$

and so on. With this the left-hand side of equation (A.10) becomes

$$\begin{aligned}
& i \frac{\partial G(n, n', p, X)}{\partial T} - (\varepsilon_n(p) - \varepsilon_{n'}(p)) \, G(n, n', p, X) + \\
& + \frac{i}{2} \frac{\partial (\varepsilon_n(p) + \varepsilon_{n'}(p))}{\partial p} \frac{\partial G(n, n', p, X)}{\partial X} + \\
& + \sum_{n_1} \Bigg[- (S/F(n, n_1, p, X) G(n_1, n', p, X) - G(n, n_1, p, X) S/F(n_1, n', p, X)) \\
& + \frac{i}{2} \left(\frac{\partial S/F(n, n_1, p, X)}{\partial p} \frac{\partial G(n_1, n', p, X)}{\partial X} - \frac{\partial S/F(n, n_1, p, X)}{\partial X} \frac{\partial G(n_1, n', p, X)}{\partial p} \right) \\
& - \frac{i}{2} \left(\frac{\partial G(n, n_1, p, X)}{\partial p} \frac{\partial S/F(n_1, n', p, X)}{\partial X} - \frac{\partial G(n, n_1, p, X)}{\partial X} \frac{\partial S/F(n_1, n', p, X)}{\partial p} \right) \Bigg] .
\end{aligned}$$

Now we need the Fourier transforms of S and F

$$S(n, n', p, X) = U(X) \delta_{n,n'} + i U'(X) X_{n,n'}(p) \tag{A.34}$$

$$F(n, n', p, X) = \delta f(X) \langle np | \tilde{V}_p | n' p \rangle + i \delta f'(X) X^{V_p}_{n,n'}(p) \, . \tag{A.35}$$

Considering only two bands 0 and 1 and omitting the arguments p and X we get for the diagonal part ($n = n' = 0$)

$$\begin{aligned}
i \frac{\partial}{\partial T} G(0) \quad & + \quad i \frac{\partial \varepsilon_0(p)}{\partial p} \frac{\partial G(0)}{\partial X} + i \left(\frac{\partial S/F(0,0)}{\partial p} \frac{\partial G(0)}{\partial X} - \frac{\partial S/F(0,0)}{\partial X} \frac{\partial G(0)}{\partial p} \right) - \\
& - \quad (S/F(0,1) G(1,0) - G(0,1) S/F(1,0)) + \\
& + \quad \frac{i}{2} \left(\frac{\partial S/F(0,1)}{\partial p} \frac{\partial G(1,0)}{\partial X} + \frac{\partial S/F(1,0)}{\partial p} \frac{\partial G(0,1)}{\partial X} \right) - \\
& - \quad \frac{i}{2} \left(\frac{\partial S/F(0,1)}{\partial X} \frac{\partial G(1,0)}{\partial p} + \frac{\partial S/F(1,0)}{\partial X} \frac{\partial G(0,1)}{\partial p} \right) = 0
\end{aligned} \tag{A.36}$$

and for the non-diagonal part

$$\begin{aligned} & i\frac{\partial}{\partial T}G(0,1) - [\varepsilon_0 - \varepsilon_1]\, G(0,1) + \frac{i}{2}\frac{\partial(\varepsilon_0+\varepsilon_1)}{\partial p}\frac{\partial G(0,1)}{\partial X} - \\ & - [S(0,0) - S(1,1)]\, G(0,1) - S(0,1)\,[G(1,1) - G(0,0)] \\ & \quad + \sum_{j=1,2}\frac{i}{2}\left(\frac{\partial S(0,j)}{\partial p}\frac{\partial G(j,1)}{\partial X} + \frac{\partial S(j,1)}{\partial p}\frac{\partial G(0,j)}{\partial X}\right) - \\ & \quad - \frac{i}{2}\left(\frac{\partial S(0,j)}{\partial X}\frac{\partial G(j,1)}{\partial p} + \frac{\partial S(j,1)}{\partial X}\frac{\partial G(0,j)}{\partial p}\right) = 0\ . \end{aligned} \tag{A.37}$$

Using Eq. (A.34) and Eq. (A.35) we get for the diagonal equation

$$\begin{aligned} & i\frac{\partial}{\partial T}G(0) + i\frac{\partial\varepsilon_0(p)}{\partial p}\frac{\partial G(0)}{\partial X} - i\frac{\partial F(0,0)}{\partial X}\frac{\partial G(0)}{\partial p} - \\ & \quad -iU'\frac{\partial G(0)}{\partial p} - iU'X_{0,1}\,(G(1,0) + G(0,1)) = 0 \end{aligned} \tag{A.38}$$

where the derivation of the off-diagonal Green function $G(0,1)$ with respect to X and the interband contribution of the quasiperiodic potential were neglected. Now we take a closer look at the diagonal element

$$F(n,n,p,X) = \delta f(X)\langle np|\tilde{V}_p|np\rangle \tag{A.39}$$

where $\delta f(X) = f(X) - f(\bar{x})$. As the total Hamiltonian does not depend on the expansion point, we can choose the expansion point arbitrarily. For a given X let us choose $\bar{x} = X$. Then $\delta f(X)$ vanishes and $F(n,n',p,X) = 0$. However we also need $\partial\delta f(X)/\partial X$ at that point. We have

$$\frac{\partial F(n,n,p,X)}{\partial X} = \frac{\partial\delta f(X)}{\partial X}\langle np|\tilde{V}_p|np\rangle\ . \tag{A.40}$$

Using

$$\frac{\partial\delta f(X)}{\partial X} = \frac{\partial(f(X) - f(\bar{x}))}{\partial X} = \frac{\partial f(\bar{x})}{\partial\bar{x}} \tag{A.41}$$

one obtains

$$\frac{\partial F(n,n,p,X)}{\partial X} = \frac{\partial f(\bar{x})}{\partial\bar{x}}\langle np|\tilde{V}_p|np\rangle = \langle np|\frac{\partial f(\bar{x})}{\partial\bar{x}}\tilde{V}_p|np\rangle\ . \tag{A.42}$$

The potential $f(\bar{x})\tilde{V}_p(x)$ is the periodic potential belonging to the periodic Hamiltonian $H_p(x,\bar{x})$ with the eigenfunctions $\varphi_{nk}(x,\bar{x})$. As in the Hamiltonian only the potential depends on the expansion point we can write

$$\frac{\partial F(n,n,p,X)}{\partial X} = \langle np|\frac{\partial H_p(x,\bar{x})}{\partial\bar{x}}|np\rangle|_{\bar{x}=X}\ . \tag{A.43}$$

Now we use the Helman-Feynman theorem which states

$$\langle np|\frac{\partial H_p(x,\bar{x})}{\partial \bar{x}}|np\rangle = \frac{\partial}{\partial \bar{x}}\langle np|H_{\bar{x}}|np\rangle = \frac{\partial \varepsilon_n(\bar{x})}{\partial \bar{x}} \tag{A.44}$$

for the matrix elements of a Hamiltonian depending on a parameter $\bar{x}$ and its eigenstates $|n\rangle_{\bar{x}}$. Therefore we get finally

$$\frac{\partial F(n,n,p,X)}{\partial X} = \frac{\partial \varepsilon_n(\bar{x})}{\partial \bar{x}}|_{\bar{x}=X} = \frac{\partial \varepsilon_n(X)}{\partial X} \ . \tag{A.45}$$

Inserting this into equation (A.38) we get

$$\begin{aligned} &i\frac{\partial}{\partial T}G(0) + i\frac{\partial \varepsilon_0(p)}{\partial p}\frac{\partial G(0)}{\partial X} - i\frac{\partial \varepsilon_0(p)}{\partial X}\frac{\partial G(0)}{\partial p} - \\ &-iU'\frac{\partial G(0)}{\partial p} - iU'X_{0,1}\left(G(1,0)+G(0,1)\right) = 0 \end{aligned} \tag{A.46}$$

For the non-diagonal equation get

$$i\frac{\partial}{\partial T}G(0,1) - \left[\varepsilon_0(p)-\varepsilon_1(p)\right]G(0,1) - iU'X_{0,1}(G(1)-G(0)) - iU'\frac{\partial G(0,1)}{\partial p} = 0 \tag{A.47}$$

where derivations with respect to the coordinate X were neglected. The coupling of the the diagonal and off-diagonal components will be treated in Appendix D.1. Neglecting this contribution and using the quasi-particle approximation for the lesser Green function

$$G(0)^{<}(p,X) = 2\pi i\delta(\omega - \varepsilon_0(p) - U(X))f(p) \ , \tag{A.48}$$

we get for the diagonal equation after an integration $\int \frac{d\omega}{2\pi}$

$$\frac{\partial f}{\partial T} + \frac{\partial \varepsilon_0(p)}{\partial p}\frac{\partial f}{\partial X} - \frac{\partial \varepsilon_0(p,X)}{\partial X}\frac{\partial f}{\partial p} + eE\frac{\partial f}{\partial p} = 0 \tag{A.49}$$

which is the Boltzmann equation that we were looking for.

Appendix A. Derivation of the driving term in the Boltzmann equation

Appendix B

Derivation of the Ktitorov model

Alternative to the approach in Appendix A it is possible to derive the Boltzmann equation in a heuristic way, which is the original way in which it was introduced. In order to describe the kinetics of an ensemble of electrons Boltzmann introduced in 1872 a probabilistic description for the evolution of the distribution. He introduced a single particle probability distribution in the phase space of the variables $\mathbf{r}$ and $\mathbf{k}$. This distribution function is usually denoted as $f(\mathbf{r}, \mathbf{k}, t)$. The total change of this distribution function in time is

$$\frac{df(\mathbf{r}, \mathbf{k}, t)}{dt} = \frac{\partial f}{\partial t} + \frac{d\mathbf{r}}{dt} \cdot \nabla_{\mathbf{r}} f + \frac{d\mathbf{k}}{dt} \cdot \nabla_{\mathbf{k}} f = \left.\frac{\partial f}{\partial t}\right|_{coll} . \tag{B.1}$$

$\partial f/\partial t|_{coll}$ describes the change of the distribution through collision events between the particles of the distribution or between a particle and an external scatterer, like phonons or impurities. Using Eq. (1.13) and the fact that the velocity is given by the derivative of the dispersion with respect to the quasimomentum get

$$\frac{\partial f}{\partial t} + \frac{\partial \varepsilon}{\partial \mathbf{k}} \cdot \nabla_{\mathbf{r}} f + \frac{1}{\hbar} e\mathbf{E} \cdot \nabla_{\mathbf{k}} f = \left.\frac{\partial f}{\partial t}\right|_{coll} . \tag{B.2}$$

The scattering probabilities of the different scattering mechanisms can be calculated via a Golden rule approach. The equation can then be solved numerically with the Monte Carlo method, but this is rather costly and therefore done in most cases for homogeneous systems only. To proceed one needs to simplify the nonlinear scattering term on the right-hand side of Eq. (B.2). The most frequently used approximation to simplify this term is the relaxation time approximation

$$\left.\frac{\partial f}{\partial t}\right|_{coll} = -\frac{1}{\tau_\varepsilon} \left(f(\mathbf{k}) - \frac{n}{n_0} f_0(\mathbf{k}) \right) - \frac{1}{\tau_{el}} \frac{1}{2} \left(f(\mathbf{k}) - f(-\mathbf{k}) \right) . \tag{B.3}$$

The first term describes the relaxation towards the equilibrium distribution function f_0 via inelastic scattering events, e. g. phonon scattering. The prefactor n/n_0 ensures conservation of particle number in inhomogeneous systems. The second term describes elastic scattering events, e. g. impurity scattering. In a strictly

one-dimensional model the only point in k-space with the same energy would be $-k$ and therefore the elastic scattering term is assumed to have the same form in three dimensions also. If one assumes homogeneity of the superlattice in x- and y-direction, for symmetry reasons

$$\nabla_{\mathbf{r}} f = \begin{pmatrix} 0 \\ 0 \\ \frac{\partial f}{\partial z} \end{pmatrix} \qquad \mathbf{E} = \begin{pmatrix} 0 \\ 0 \\ E \end{pmatrix} \tag{B.4}$$

and the Boltzmann equation reduces to

$$\frac{\partial f}{\partial t} + v_p \frac{\partial f}{\partial z} + \frac{eE}{\hbar} \frac{\partial f}{\partial k} = -\frac{1}{\tau_\varepsilon} \left(f - \frac{n}{n_0} f_0 \right) - \frac{1}{\tau_{el}} \frac{1}{2} \left(f(\mathbf{k}) - f(-\mathbf{k}) \right) \tag{B.5}$$

with $f = f(z, \mathbf{k})$. Now carry out the summations over the wave-vectors k_x and k_y to get

$$\frac{\partial f'}{\partial t} + v_p \frac{\partial f'}{\partial z} + eE \frac{\partial f'}{\partial k} = -\frac{1}{\tau_\varepsilon} (f' - \frac{n}{n_0} f_0') - \frac{1}{\tau_{el}} \frac{1}{2} \left(f'(k) - f'(-k) \right) \tag{B.6}$$

with the definition $f'_{(0)}(z,k) = \sum_{k_x,k_y} f_{(0)}(z, \mathbf{k})$. The sum in the first term can be cast into an integral

$$\sum_{k_x,k_y} f_{(0)}(k_x, k_y, k) = \frac{L^2}{2\pi^2} \int f_{(0)}(k_x, k_y, k) dk_x dk_y \ , \tag{B.7}$$

where on the right hand side spin degeneracy is taken into account. This shows that the effect of the x-y-dimension is that for f_0 one has to use the integrated function f_0'. Assuming a Fermi-Dirac distribution for f_0

$$f_0(\mathbf{k}) = f_0(k_\perp, k) = \left(1 + exp \left[\beta \left(\frac{\hbar^2 k_\perp^2}{2m^*} + \frac{\Delta}{2} \left[1 - \cos(kd) \right] - \mu \right) \right] \right)^{-1} \ , \tag{B.8}$$

one obtains

$$\begin{aligned} f'_{(0)}(z,k) &= \frac{L^2}{\pi} \int_0^\infty k_\perp dk_\perp \left(1 + \exp \left[\beta \left(\frac{\hbar^2 k_\perp^2}{2m^*} + \frac{\Delta}{2} \left[1 - \cos(kd) \right] - \mu \right) \right] \right)^{-1} \\ &= \frac{L^2}{\pi} \frac{2m^*}{\beta \hbar^2} \int_0^\infty \frac{r dr}{1 + \exp \left[r^2 + \beta(\epsilon(k) - \mu) \right]} \end{aligned} \tag{B.9}$$

with $\epsilon(k) = [\Delta/2(1 - \cos(kd))]$. The integral can be solved analytically to give

$$\int_0^\infty \frac{r dr}{1 + \exp \left[r^2 + \beta(\epsilon(k) - \mu) \right]} = -\frac{1}{2} \left[ln(1 + e^{-r^2 - \beta(\epsilon - \mu)}) \right]_0^\infty = \frac{1}{2} ln(1 + e^{-\beta(\epsilon - \mu)}) \tag{B.10}$$

and finally

$$f'_{(0)}(z,k) = \frac{L^2}{2\pi}\frac{2m^*}{\beta\hbar^2} ln(1 + e^{-\beta(\epsilon-\mu)}) \; . \tag{B.11}$$

In the following the prime will be omitted again in the equations. Under the assumption that elastic scattering does not couple to the transverse degrees of freedom one gets

$$\frac{\partial f}{\partial t} + v_p\frac{\partial f}{\partial z} + \frac{eE}{\hbar}\frac{\partial f}{\partial k} = -\frac{1}{\tau_\varepsilon}\left(f(k) - \frac{n}{n_0}f_0(k)\right) - \frac{1}{\tau_{el}}\frac{1}{2}\left(f(k) - f(-k)\right) \; . \tag{B.12}$$

If the system is also homogeneous in the z-direction this equation reduces to

$$\frac{\partial f}{\partial t} + \frac{eE}{\hbar}\frac{\partial f}{\partial k} = -\frac{1}{\tau_\varepsilon}\left(f(k) - f_0(k)\right) - \frac{1}{\tau_{el}}\frac{1}{2}\left(f(k) - f(-k)\right) \tag{B.13}$$

which was proposed by Ktitorov *et al.* in 1972 [Kti72]. Of course the extension of the simple one-dimensional elastic scattering term to three dimensions is somewhat arbitrary. The effect of the two perpendicular dimensions on the elastic scattering has been investigated in [Ger93]. It is shown that the qualitative behavior stays the same as in the strictly one-dimensional description, while the maximum of the v_d-E relation and the critical field E_c where the curve reaches its maximum are changed. In my numerical simulations Eq. (B.12) was mostly used without the elastic scattering term.

Appendix C

The drift-diffusion model

Consider the one-dimensional Boltzmann equation in the form of Eq. (B.12) in Appendix B

$$\frac{\partial f}{\partial t} + v_k \frac{\partial f}{\partial x} + eE\frac{\partial f}{\partial k} = -\nu(f - \frac{n}{n_0} f_0) \tag{C.1}$$

without the elastic scattering term. Here $v_k = \Delta d/2\hbar \sin(kd) = v_0 \sin(kd)$ is the quasiparticle group velocity and $\varepsilon_p = -\Delta/2 \cos(kd)$. The average $\langle \cdots \rangle$ is determined by

$$\langle \cdots \rangle = \frac{1}{n} \int \cdots f(k,x,t) dk \; .$$

The moment-balance equations are obtained by multiplying both sides of the Boltzmann equation with 1, v, ε and integrating over k-space. One gets the continuity equation and

$$\frac{\partial (n\langle v \rangle)}{\partial t} + \frac{\partial (n\langle v^2 \rangle)}{\partial x} - en \left\langle \frac{\partial v}{\partial p} \right\rangle E = -\nu n \langle v \rangle \tag{C.2}$$

$$\frac{\partial (n\langle \varepsilon \rangle)}{\partial t} + \frac{\partial (n\langle v\varepsilon \rangle)}{\partial x} - en\langle v \rangle E = -\nu n (\langle \varepsilon \rangle - \varepsilon_T) \; . \tag{C.3}$$

If one uses the solution of the homogeneous Boltzmann equation to calculate the higher momenta one obtains

$$\frac{\partial (n\langle v \rangle)}{\partial t} + \frac{v_0^2}{2}\frac{\partial}{\partial x}\left[\left(1 - \frac{I_2}{I_0}\left(1 + \left(\frac{2E}{Ec} \right)^2 \right)^{-1} \right) n \right] + \frac{ed^2}{\hbar^2} n\langle \varepsilon \rangle E = -\nu n \langle v \rangle \tag{C.4}$$

$$\frac{\partial (n\langle \varepsilon \rangle)}{\partial t} - \frac{\Delta}{2} v_0 \frac{I_2}{I_0}\frac{\partial}{\partial x}\left[\frac{E/Ec}{1 + \left(\frac{2E}{Ec}\right)^2} n \right] - en\langle v \rangle E = -\nu n (\langle \varepsilon \rangle - \varepsilon_T) \tag{C.5}$$

where I_m are the modified Bessel functions. In the homogeneous and time-independent case these equations can be solved to give (omitting the averaging brackets from now on)

$$v_d = v_0 \frac{I_1}{I_0} \frac{E/E_c}{1 + (E/E_c)^2} \tag{C.6}$$

and

$$\varepsilon_d = \frac{\varepsilon_0}{1+(E/E_c)^2} = -\frac{\Delta}{2}\frac{I_1}{I_0}\frac{1}{1+(E/E_c)^2} \tag{C.7}$$

where we have used $E_c = \hbar\nu/ed$ and that the equilibrium energy of the electrons is given by $\varepsilon_0 = -\Delta/2\langle cos(pd/\hbar)\rangle = -\Delta/2 \times I_1/I_0$.

From equation (C.5) we get

$$n\varepsilon = n\varepsilon_0 - \frac{1}{\nu}\left(\frac{\partial(n\varepsilon)}{\partial t} - \frac{\Delta}{2}v_0\frac{I_2}{I_0}\frac{\partial}{\partial x}\left[\frac{E'}{1+(2E')^2}n\right] - envE\right) \tag{C.8}$$

where $E' = E/E_c$, and inserting this into equation (C.5) we get finally

$$nv(1+E'^2) = nv_0\frac{I_1}{I_0}E' - \frac{v_0^2}{2\nu}\frac{\partial}{\partial x}\left[\left(1-\frac{I_2}{I_0}\frac{1}{1+(2E')^2}\right)n\right] -$$
$$-\frac{v_0^2E'}{2\nu}\frac{I_2}{I_0}\frac{\partial}{\partial x}\left[\frac{2E'}{1+(2E')^2}n\right] - \frac{1}{\nu}\frac{\partial n}{\partial t}\left(v - \frac{dE'}{\hbar}\varepsilon\right) - \frac{n}{\nu}\left(\frac{\partial v}{\partial E'} - \frac{dE'}{\hbar}\frac{\partial \varepsilon}{\partial E'}\right)\frac{\partial E'}{\partial t}\ .$$

Now assume to have a slowly varying problem in space and time. Inserting the static solutions v_d and ε_d for v and ε we get

$$-\frac{1}{\nu}\frac{\partial n}{\partial t}\left(v - \frac{dE'}{\hbar}\varepsilon\right) = \frac{1}{\nu}\frac{\partial nv}{\partial x}2v_d = \frac{2v_d^2}{\nu}\frac{\partial n}{\partial x} + \frac{2nv_d}{\nu}\frac{\partial v}{\partial E'}\frac{\partial E'}{\partial x} \tag{C.9}$$

and

$$\left(\frac{\partial v}{\partial E'} - \frac{dE'}{\hbar}\frac{\partial \varepsilon}{\partial E'}\right)\frac{\partial E'}{\partial t} =$$
$$\left(v_0\frac{I_1}{I_0}\frac{1-E'^2}{(1+(E')^2)^2} + v_0\frac{I_1}{I_0}\frac{2E'^2}{(1+(E')^2)^2}\right)\frac{\partial E'}{\partial t} = v_0\frac{I_1}{I_0}\frac{1}{1+(E')^2}\frac{\partial E'}{\partial t} \tag{C.10}$$

and we get altogether

$$nv(1+E'^2) = nv_0\frac{I_1}{I_0}E' - \frac{v_0^2}{2\nu}\left(1-\frac{I_2}{I_0}\frac{1-2E'^2}{1+(2E')^2}\right)\frac{\partial n}{\partial x} + \frac{2v_d^2}{\nu}\frac{\partial n}{\partial x} -$$
$$\frac{v_0^2}{2\nu}\frac{I_2}{I_0}n\frac{2E'(5-4E'^2)}{(1+(2E')^2)^2}\frac{\partial E'}{\partial x} + \frac{2nv_d}{\nu}\frac{\partial v}{\partial E'}\frac{\partial E'}{\partial x} - \frac{n}{\nu}v_0\frac{I_1}{I_0}\frac{1}{1+(E')^2}\frac{\partial E'}{\partial t}\ . \tag{C.11}$$

Now we define

$$D := \frac{1}{1+E'^2}\frac{v_0^2}{2\nu}\left(1-\frac{I_2}{I_0}\frac{1-2E'^2}{1+(2E')^2} - 4\left(\frac{I_1}{I_0}\frac{E'}{1+(E')^2}\right)^2\right) \tag{C.12}$$

and

$$C := \frac{n}{\nu}v_0\frac{I_1}{I_0}\frac{1}{(1+(E')^2)^2}\ , \tag{C.13}$$

Neglecting the $\frac{\partial E}{\partial x}$-terms in equation (C.11) we get

$$nv = nv_d - D\frac{\partial n}{\partial x} - C\frac{\partial E'}{\partial t} \ . \tag{C.14}$$

The ratio of the mobility and the diffusion coefficient is given by

$$\begin{aligned}
\frac{D}{\mu} = \frac{D}{v_d/E} &= \frac{\frac{1}{1+E'^2}\frac{v_0^2}{2\nu}\left(1 - \frac{I_2}{I_0}\frac{1-2E'^2}{1+(2E')^2} - 4\left(\frac{I_1}{I_0}\frac{E'}{1+(E')^2}\right)^2\right)}{v_0\frac{I_1}{I_0}\frac{1/E_c}{1+(E/E_c)^2}} = \\
&= \frac{v_0 E_c}{2\nu}\frac{I_0}{I_1}\left(1 - \frac{I_2}{I_0}\right)\left(1 + \frac{\frac{I_2}{I_0}\frac{6E'^2}{1+(2E')^2} - 4\left(\frac{I_1}{I_0}\frac{E'}{1+(E')^2}\right)^2}{\left(1 - \frac{I_2}{I_0}\right)}\right) = \\
&= \frac{k_B T}{e}\left(1 + \frac{\frac{I_2}{I_0}\frac{6E'^2}{1+(2E')^2} - 4\left(\frac{I_1}{I_0}\frac{E'}{1+(E')^2}\right)^2}{\left(1 - \frac{I_2}{I_0}\right)}\right) \ ,
\end{aligned} \tag{C.15}$$

using Bessel function identities. This coincides with the result from [Ign84]. In the low-field limit $E' \to 0$ or the small miniband limit $\beta\Delta/2 \to 0$ this reduces to the Einstein relation $D/\mu = k_B T/e$. Fig. C.1 shows the ratio D/μ for different

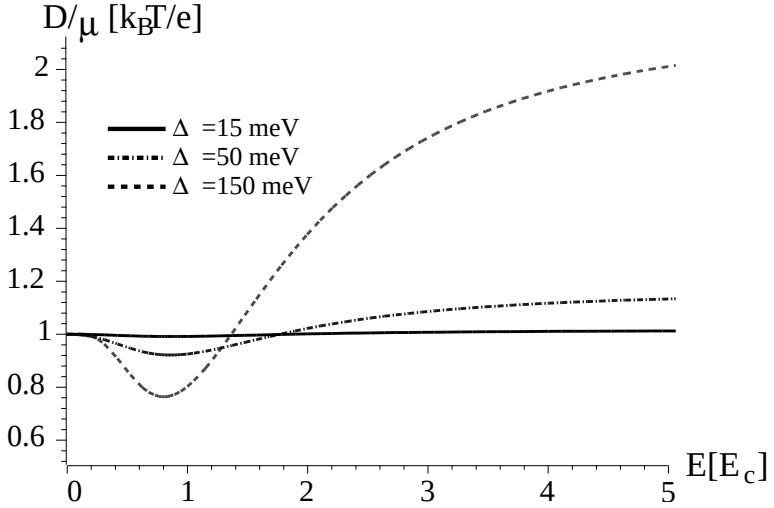

Fig. C.1: *The diffusion coefficient D over the mobility μ as a function of the normalized applied field $E' = E/E_c$ and different miniband widths Δ for room temperature.*

miniband widths at room temperature. In the limit $E' \to \infty$ get

$$\frac{D}{\mu} = \left(\frac{3}{4}\frac{I_0}{I_1}\frac{\beta\Delta}{2} - \frac{1}{2}\right)\frac{k_B T}{e} \ , \tag{C.16}$$

i. e. the curves saturate for large E'. For not too large minibands ($\beta\Delta/2 \leq 1$) we get $D/\mu = \left(1 + \frac{3}{16}\left(\frac{\beta\Delta}{2}\right)^2\right)\frac{k_B T}{e}$ for the saturation value.

Appendix D

Tunneling

D.1 Zener tunneling

I first consider the simplest conceivable model for Zener tunneling, that is a periodic potential with only one Fourier component of the potential not equal to zero[1]

$$V(x) = 2V_Q \cos(Qx) = V_Q \left(e^{iQx} + e^{-iQx}\right) \quad \text{with} \quad V_Q \ll \frac{(Q/2)^2}{2m} \,. \tag{D.1}$$

Around the point $k = Q/2$ in the reciprocal space the dispersion is linearized and the potential couples approximately only the two bands depicted in Fig. D.1.

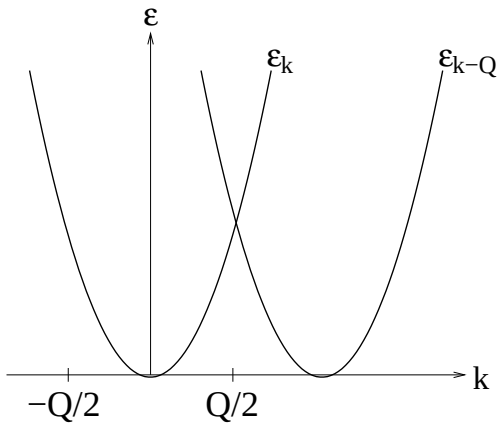

Fig. D.1: *The free electron parabola and the same parabola shifted by a reciprocal lattice vector Q.*

If an electric field E is applied, the quantum mechanical eigenstates will travel through the reciprocal space according to the relation $\dot{k} = eE$. The energy of the free electron is linearized by

$$\varepsilon(k) = \frac{(Q/2)^2}{2m} + \frac{Q/2}{m}(k - Q/2), \tag{D.2}$$

[1] Planck's constant $\hbar = 1$ in this Appendix

or as a function of time, shifting the zero energy to $(Q/2)^2/2m$ and setting $k = Q/2$ at $t = 0$

$$\varepsilon(t) = \frac{Q/2}{m} eEt = \dot{\varepsilon} t \ . \tag{D.3}$$

The state $\varepsilon_{k-Q}(t) \approx -\dot{\varepsilon} t$ is coupled to the state ε_k via the amplitude V_Q. For the amplitude of the two states of the crossing bands one has to solve the Schrödinger equation

$$\begin{pmatrix} \varepsilon(t) & V_Q \\ V_Q & -\varepsilon(t) \end{pmatrix} \begin{pmatrix} a \\ b \end{pmatrix} = i \frac{\partial}{\partial t} \begin{pmatrix} a \\ b \end{pmatrix} \ . \tag{D.4}$$

This problem was considered by Zener in 1932 [Zen32]. He considered the problem of two crossing energy levels with linear dependence of the energy difference in time and constant coupling matrix element. Starting with the system in one state $a(-\infty) = 1$ and $|b(-\infty)| = 0$ one can calculate the probability P that the electron stays in the initial state, i. e. $|a(\infty)|$, solving the coupled differential equations resulting from Eq. D.4. The result is

$$P = exp\left(-\frac{\pi V_Q^2}{\dot{\varepsilon}}\right) \ . \tag{D.5}$$

Zener did not refer in his paper to the fact that tunneling between energy bands might be described by the model. He rather published two years later his classical paper [Zen34] which attributed the high-field breakdown in dielectrics to tunneling processes between bands. The model he uses there has at first sight nothing to do with the previous model, but the connection will be established in the following.

Starting from the model in Fig. D.1 one can approach the problem as follows. One can transform the basis in Eq. (D.4) locally in time since the Hamiltonian

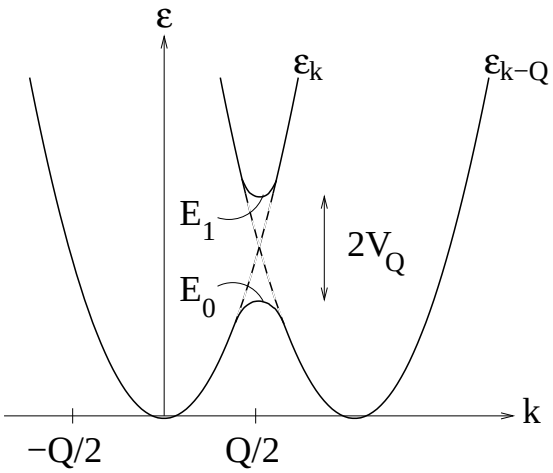

Fig. D.2: *The crossing of the two energy parabola (dotted lines) with the eigenenergies $E_{0/1}(k)$ of the local eigenstates (solid lines).*

is time-dependent to the eigenstates (Fig. D.2) and denote the corresponding amplitudes by α and β:

$$\begin{pmatrix} a \\ b \end{pmatrix} = \begin{pmatrix} x & y \\ y & -x \end{pmatrix} \begin{pmatrix} \alpha \\ \beta \end{pmatrix} . \tag{D.6}$$

The columns of the unitary matrix are the eigenvectors with time-dependent entries, for which one has

$$x^2(t) = \left(1 + \frac{\varepsilon}{W}\right)/2, \quad y^2(t) = \left(1 - \frac{\varepsilon}{W}\right)/2 \quad \text{and} \quad x(t)y(t) = \frac{V_Q}{2W(t)} \tag{D.7}$$

where $W(t) = \sqrt{\varepsilon^2 + V_Q^2}$. The corresponding eigenvalues are $E_{0/1}(k) = \pm W$. Then Eq. (D.4) can be written in the new basis as

$$\begin{pmatrix} -iW(t) & \dot{\varepsilon}\frac{V_Q}{2W^2} \\ \dot{\varepsilon}\frac{V_Q}{2W^2} & iW(t) \end{pmatrix} \begin{pmatrix} \alpha \\ \beta \end{pmatrix} = \frac{\partial}{\partial t} \begin{pmatrix} \alpha \\ \beta \end{pmatrix} . \tag{D.8}$$

The equations for the density matrix are

$$\frac{\partial}{\partial t}(\beta\beta^* - \alpha\alpha^*) = -2S(\beta\alpha^* + \alpha\beta^*) \tag{D.9}$$

$$\frac{\partial}{\partial t}\beta\alpha^* = 2iW\beta\alpha^* + S(\beta\beta^* - \alpha\alpha^*) \tag{D.10}$$

$$\frac{\partial}{\partial t}\alpha\beta^* = -2iW\alpha\beta^* + S(\beta\beta^* - \alpha\alpha^*) \tag{D.11}$$

with $S = \dot{\varepsilon}\frac{V_Q}{2W^2}$. Defining $U_1 := \beta\alpha^* + \alpha\beta^*$, $U_2 := i(\beta\alpha^* - \alpha\beta^*)$ and $U_3 := \beta\beta^* - \alpha\alpha^*$ one obtains

$$\frac{d}{dt}\mathbf{U} = \mathbf{\Omega} \times \mathbf{U} \tag{D.12}$$

with $\mathbf{\Omega} = 2S\mathbf{e_2} - 2W\mathbf{e_3}$. This describes the rotation of $\mathbf{U}$ around the direction of $\mathbf{\Omega}$. The coupled differential equations can be solved e. g. with Maple and the result in Eq. (D.5) is reproduced numerically. We described this alternative way of getting the Zener transition probability since one can relate the equations resulting from the Boltzmann equation and the equations in the literature easier with it.

To make the transition to a general system with a periodic potential we start with equations (A.38) and (A.47) for a homogeneous situation

$$\frac{\partial}{\partial T}G_0 + eEX_{0,1}\left(G_{10} + G_{01}\right) + eE\frac{\partial G_0}{\partial p} = 0 \tag{D.13}$$

$$\frac{\partial}{\partial T}G_{01} + i\left[E_0(p) - E_1(p)\right]G_{01} + eEX_{0,1}(G_1 - G_0) + eE\frac{\partial G_{01}}{\partial p} = 0 . \tag{D.14}$$

Now we transform the equations into a moving frame. Define $x = p - eET$, $\tilde{G}_0(x,T) = G_0(p - eET, T)$ and so on. We get

$$\frac{\partial G_0}{\partial T} = -eE\frac{\partial \tilde{G}_0}{\partial x} + \frac{\partial \tilde{G}_0}{\partial T} \tag{D.15}$$

$$\frac{\partial G_0}{\partial p} = \frac{\partial \tilde{G}_0}{\partial x} \tag{D.16}$$

and therefore

$$\frac{\partial \tilde{G}_0}{\partial T} + eEX_{0,1}(\tilde{G}_{10} + \tilde{G}_{01}) = 0\ . \tag{D.17}$$

The coupling constant W has to be evaluated at the point $p = x + eET$. Transforming the equations for G_1 we get

$$\frac{\partial \tilde{G}_1}{\partial T} - eEX_{0,1}(\tilde{G}_{10} + \tilde{G}_{01}) = 0\ . \tag{D.18}$$

For the off-diagonal part we get

$$\frac{\partial \tilde{G}_{01}}{\partial T} + eEX_{0,1}(\tilde{G}_1 - \tilde{G}_0) - i\left[E_1(p) - E_0(p)\right]\tilde{G}_{01} = 0 \tag{D.19}$$

and the complex conjugate for $\tilde{G}_{10}$. The diagonal equations can be written

$$\frac{\partial \tilde{G}_1 - \tilde{G}_0}{\partial T} = 2eEX_{0,1}(\tilde{G}_{10} + \tilde{G}_{01})\ . \tag{D.20}$$

Specializing these equations to the case considered before, namely the crossing of two free-electron parabolas coupled via a constant matrix element, one can calculate $X_{0,1}$. The Bloch states are given for this case by

$$\varphi_{k,1} = xe^{ikx} + ye^{i(k-Q)x} \quad \text{and} \quad \varphi_{k,0} = ye^{ikx} - xe^{i(k-Q)x} \tag{D.21}$$

so that

$$X_{0,1} = \frac{1}{2}\int_0^L \left(u^*_{nk}(x')\frac{\partial u_{n'k'}}{\partial k'}(x') - \frac{\partial u^*_{nk}}{\partial k}(x')u_{n'k'}(x')\right)dx' = -\frac{V_Q}{2W^2}\frac{\partial \varepsilon}{\partial k}\ . \tag{D.22}$$

Then one has $eEX_{0,1} = \dot{k}X_{0,1} = -S$ and the equations for the Green functions are in this limit equivalent to Eqs. (D.9, D.10, D.11) identifying G_{01} with $\alpha^*\beta$ and so on.

In the following it is assumed that the diagonal Green functions are only slightly affected by the transition, i. e. in Eq. (D.19) one approximates $\tilde{G}_1 = 0$ and $\tilde{G}_0 = 1$. We get then for the off-diagonal part

$$\tilde{G}_{01}(t) = \int_{-t_0}^{t} eEX_{0,1}(t')e^{-i\int_t^{t'}(E_1 - E_0)d\tau'}dt'\ . \tag{D.23}$$

The occupation in the upper band is therefore at a time t_0

$$\tilde{G}_1(t_0) = \frac{1}{2}\int_{-t_0}^{t_0} \frac{\partial\left(\tilde{G}_1 - \tilde{G}_0\right)}{\partial t} dt = \tag{D.24}$$

$$\int_{-t_0}^{t_0} eEX_{0,1}(t) \int_{-t_0}^{t} eEX_{0,1}(t') e^{-i\int_t^{t'}(E_1-E_0)d\tau'} dt' dt + c.c. = \tag{D.25}$$

$$= \int_{-t_0}^{t_0} eEX_{0,1}(t) \int_{t}^{t_0} eEX_{0,1}(t') e^{i\int_t^{t'}(E_1-E_0)d\tau'} dt' dt + c.c. \tag{D.26}$$

which can be written as

$$\tilde{G}_1(t_0) = \left| \int_{-t_0}^{t_0} eEX_{0,1}(t) e^{i\int_{-t_0}^{t'}(E_1-E_0)(\tau')d\tau'} dt \right|^2 . \tag{D.27}$$

This is exactly the tunneling probability given in [Kri86] and applied to inter-miniband tunneling in [Sib89]. Since k and t are linearly related the probability for a transition for the transversal of the Brillouin zone can be written as

$$\tilde{G}_1(t_0) = \left| \int_{-Q/2}^{Q/2} X_{0,1}(k) e^{i/(eE)\int_0^k (E_1-E_0)(k')dk'} dk \right|^2 =: |M_{0,1}|^2 . \tag{D.28}$$

Here it is assumed that the Brillouin zone is transversed in the time interval $-t_0 \cdots t_0$. Kane [Kan59, Kan60] has shown that the integral over the Brillouin zone in Eq. (D.28) is the overlap of two Wannier-Stark states in different bands. At this point it is also possible to make a connection to the description of tunneling by Zener [Zen34].

Let us take a close look at the integral $M_{0,1} = \int_{-Q/2}^{Q/2} X_{0,1}(k) e^{i/(eE)\int_0^k (E_1-E_0)(k')dk'} dk$ in the tunneling probability for one zone crossing. If we are only interested in the exponential factor, neglecting the interband matrix element $X_{0,1}$, the integral can be solved with the help of the method of steepest descent. Apart from prefactors, which we do not care about at the moment, the integral can be approximated by

$$M_{0,1} = e^{i/(eE)\int_0^{k_0} (E_1-E_0)(k')dk'} \tag{D.29}$$

where a complex k_0 is given by the condition $E_0(k_0) = E_1(k_0) = 0$ and the zero-point of the energy was put to the middle of the bandgap. Since the two bands are not degenerate in one dimension this equation can only be solved in the complex k-plane. Define the parameters z_0 and z_1 for a given complex k-value by the relations

$$z_0 = \frac{E_0(k)}{eE} \text{ where } z < 0 \qquad \text{and} \qquad z_1 = \frac{E_1(k)}{eE} \text{ where } z > 0 . \tag{D.30}$$

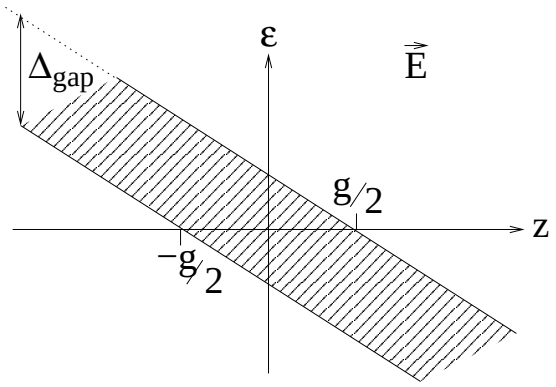

Fig. D.3: *The miniband gap with the local energy shifted by the electric field.*

It can be interpreted as the position, where the total energy $E_i(k) - eEz$ of a particle with given k is zero (Fig. D.3). Of course the energy values $-\Delta_{gap}/2 < E < \Delta_{gap}/2$ can be only reached for complex k-values which belong to exponentially growing or decaying states in the bandgap. Get

$$M_{0,1} = \exp\left(i \int_0^{k_0} (z_1 - z_0)(k')dk'\right) . \tag{D.31}$$

The integrals can also be written as integral over the new parameter z

$$M_{0,1} = \exp\left(i \int_{g/2}^{0} z_1 \frac{dk'}{dz_1} dz_1 - i \int_{-g/2}^{0} z_0 \frac{dk'}{dz_0} dz_0\right) , \tag{D.32}$$

with $g = E_{gap}/(eE)$. Using an integration by parts yields

$$M_{0,1} = \exp\left(i \int_0^{g/2} k' dz_1 + i \int_{-g/2}^{0} k' dz_0\right) . \tag{D.33}$$

Here k' can be deduced by inverting Eqs. (D.30). This is exactly the expression used by Zener in [Zen34] to calculate the interband transition probability. A complex k-value is deduced from inverting the energy dispersions in the forbidden region and then one integrates over the energetically forbidden region in the spirit of a WKB approximation.

Now let us specialize again to the crossing of two free-electron parabola. Here the relations (D.30) can be easily inverted using $E_{0/1}(k) = \mp\sqrt{\alpha^2 k^2 + V_Q^2}$ with $\alpha = \partial\varepsilon/\partial k$ to get

$$k = \frac{i}{\alpha}\sqrt{V_Q^2 - (eEz)^2} . \tag{D.34}$$

Evaluating the integral we get

$$M_{0,1} = \exp\left(-\frac{\pi V_Q^2}{2\alpha eE}\right) \tag{D.35}$$

or for the transition probability of one zone crossing

$$P = \exp\left(-\frac{\pi V_Q^2}{\dot{\varepsilon}}\right) \tag{D.36}$$

which reproduces the result found earlier. It is interesting to note that this approximation reproduces the exact probability even though we have thrown away all prefactors during the derivation.

The Zener tunneling probability through the miniband gap for a typical superlattice can be estimated as follows:
For a GaAs/AlGaAs superlattice with standard parameters (Tab. 1.1) one obtains for the gap energy $\varepsilon_{gap} = 340$ meV. For a typical value of the field $E = 10^6$ V/m we get $\pi V_Q^2/\hbar\dot{\varepsilon} \approx 100$. The probability becomes appreciable if either the field is much larger or the gap becomes smaller. Therefore interband transitions can normally be neglected.

D.2 Tunneling through triangular barriers

With the help of the approximation derived above the tunneling probability out of the miniband through the triangular barrier at the right end of the superlattice was estimated. Fig. D.4 shows the scenario. If the barrier is only penetrated

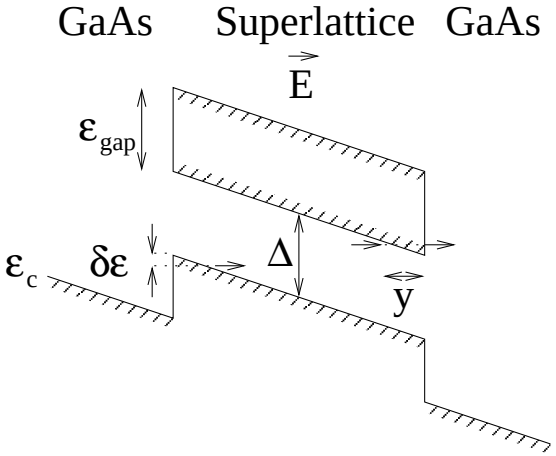

Fig. D.4: *Electrons can tunnel through the triangular barriers at both ends of the superlattice with applied field. At the left side the energy difference $\delta\varepsilon$ of an electron to the miniband bottom is determining the tunneling probability and at the right side the distance to the superlattice end y is determining the probability.*

slightly, the imaginary k at the point $z = -g/2 + \delta z$ can be approximated by

$$k = \frac{i\sqrt{2V_Q eE}}{\alpha}\sqrt{\delta z} \tag{D.37}$$

which results integrated from 0 to y in a transition probability

$$P = \exp\left(-\frac{\sqrt{2V_Q eE}}{\alpha}\frac{4}{3}y^{3/2}\right) . \tag{D.38}$$

It is interesting to note that for a fixed position y the tunneling probability decreases with increasing field which is plausible since the triangular barrier grows with rising field. In Chapter 3 the implications of this tunneling on the transport for realistic device parameters is investigated.

To complete the considerations on tunneling let us finally consider the triangular barrier that arises at the left side of the superlattice when a field is applied (see Fig. D.4). Electrons with energy $\delta\varepsilon$ below the peak of the triangle can still tunnel into the miniband region. Using $\delta\varepsilon = yeE$ in Eq. (D.38) we get

$$P = \exp\left(-\frac{4}{3eE}\frac{\sqrt{2V_Q}}{\alpha}\delta\varepsilon^{3/2}\right) . \tag{D.39}$$

Alternatively one can evaluate the WKB-integral

$$I = \sqrt{2m_l^\star}\int_0^{\delta\varepsilon/eE}\sqrt{\delta\varepsilon - eEx}dx = \frac{2}{3eE}\sqrt{2m_l^\star}\delta\varepsilon^{3/2} \tag{D.40}$$

to get for the probability

$$P = \exp(-2I) = \exp\left(-\frac{4}{3eE}\sqrt{2m_l^\star}\delta\varepsilon^{3/2}\right) \tag{D.41}$$

which is equivalent to D.39 using the effective mass of electrons at the bottom of the miniband

$$m_l^\star = \left.\frac{\partial^2\varepsilon}{\partial k^2}\right|^{-1}_{k=Q/2} = \frac{V_Q d^2 m^2}{\pi^2} = \frac{V_Q}{\alpha^2} . \tag{D.42}$$

Appendix E

The upwind procedure

In this appendix the upwind procedure which was used to discretize the Boltzmann equation is described. The upwind procedure is illustrated first for the discretization of the Boltzmann equation for a periodic potential without variation

$$\frac{\partial f}{\partial t} = -v(p)\frac{\partial f}{\partial z} - eE\frac{\partial f}{\partial p} \; . \tag{E.1}$$

The time derivative is discretized by

$$\frac{\partial f}{\partial t} = \frac{f(t+\Delta t) - f(t)}{\Delta t} \; . \tag{E.2}$$

The derivatives on the right side are calculated using the values at the time t and therefore $f(t+\Delta t)$ can be calculated from the values at time t, i. e. it is an explicit scheme.

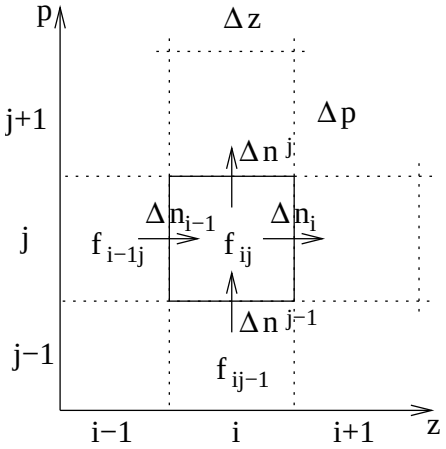

Fig. E.1: *The grid element at space point i and momentum point j with density f_{ij} and the surrounding grid elements. The width of the elements is Δz in z-direction and Δp in momentum direction. The quantities Δn show the flow of particles to the neighboring elements which results from the particle drift in phase space.*

The upwind discretization is used to describe a particle flow in phase space and depends on the direction of the flow of the particles. Let us assume $v > 0$ and $eE > 0$, the other cases can be deduced analogously. Fig. E.1 shows an arbitrary

element of phase space with particle density f_{ij} where i and j denote the index in real and momentum space. For positive velocity the number of particles flowing out of the phase space element into the right neighboring element in space at site $i+1$ is given by $\Delta n_i = A f_{ij} v \Delta t$, where A is the area of the surface through which the particles stream. The number of particles flowing into the phase space element from the left is given by $\Delta n_{i-1} = A f_{i-1j} v \Delta t$ so that the change in density is given by

$$\frac{\Delta f}{\Delta t} = \frac{\Delta n}{A \Delta z \Delta t} = \frac{-\Delta n_i + \Delta n_{i-1}}{A \Delta z \Delta t} = -v(p) \frac{f_{ij} - f_{i-1j}}{\Delta z} \; . \tag{E.3}$$

This suggests to discretize the derivative in equation (E.1) by

$$-v \frac{\partial f}{\partial z} = -v \frac{f_{ij} - f_{i-1j}}{\Delta z} \; . \tag{E.4}$$

rather than a central difference scheme $\frac{\partial f}{\partial z} = \frac{f_{i+1j} - f_{i-1j}}{2\Delta z}$ or another discretizing procedure. In the same way the flow direction in momentum space for positive eE suggests to use the discretization

$$\frac{\partial f}{\partial p} = \frac{f_{ij} - f_{ij-1}}{\Delta p} \; . \tag{E.5}$$

Besides the intuitive justification for the upwind procedure it turned out that it is very stable for the coupled Poisson-Boltzmann problem even if one introduces discontinuities at boundaries between different regions. While a stability analysis could be carried out for the Boltzmann equation alone, it is not clear to me how to generalize this analysis to the coupled Poisson-Boltzmann system, which is therefore not attempted here. A disadvantage of the upwind procedure is that it introduces additional diffusion effects, which tend to smoothen sharp wave fronts. But using the relaxation time approximation an exact quantitative analysis is out of reach anyway and I am mainly interested in the dynamics rather than the exact shape of the domains in the NDC material and therefore this disadvantage is accepted. Other explicit integration schemes for equations of type (E.1) were tested and turned out to be unstable especially at the boundaries, while implicit schemes were not tested at all due to the effort necessary for the implementation.

The next question that needs to be addressed is how the extension to equation (2.18) can be achieved. The derivative at constant energy necessitates to take the density at the neighboring gridpoint with equal energy. Then one can discretize $\frac{\partial \varepsilon(p)}{\partial p} \, |_z \, \frac{\partial \tilde{f}}{\partial z} \, |_\varepsilon$ using the upwind method

$$\frac{\partial \varepsilon(p)}{\partial p} \, |_z \, \frac{\partial \tilde{f}}{\partial z} \, |_\varepsilon = \left. \frac{\partial \varepsilon}{\partial p} \right|_z \frac{\tilde{f}_{i\varepsilon} - \tilde{f}_{i-1\varepsilon}}{\Delta z} \; . \tag{E.6}$$

The density $\tilde{f}_{i-1\varepsilon}$ is the density at the neighboring p-point with the same energy. This discretization turned out to be more stable than using equation (2.14) where $\partial\varepsilon/\partial z$ appears if the dispersion changes on a short scale so that $\partial\varepsilon/\partial z$ is large.

Appendix F

Cavity

The derivation in this appendix follows [Ung89]. We assume that a resonator can be described by a cavity with conducting walls, the source can be described by a known current distribution. Furthermore there may be a hole in the cavity for the emission of radiation. The idea is to expand the field in the cavity in the absence of the source by a complete set of eigenmodes. We assume that all fields have a time dependence of the form: $\mathbf{E}(\mathbf{x}, t) = \mathbf{E}(\mathbf{x}) \exp(-i\omega t)$.

We start from Maxwell's equations

$$\nabla \times \mathbf{E}(\mathbf{x}) = i\omega\mu_0 \mathbf{H}(\mathbf{x}) \tag{F.1}$$

$$\nabla \times \mathbf{H}(\mathbf{x}) = \mathbf{J}(\mathbf{x}) - i\omega\epsilon_0 \mathbf{E}(\mathbf{x}) \; . \tag{F.2}$$

For the fields we use the expansion with respect to eigenmodes with frequency ω_n of the cavity with ideal conducting walls in the absence of sources and holes. The corresponding fields $\mathbf{E}_n$ and $\mathbf{H}_n$ form an orthogonal set. They fulfill the boundary conditions that the tangential component of $\mathbf{E}_n$ and the normal component of $\mathbf{H}_n$ vanish on the surface. We assume that the fields are normalized as

$$\epsilon_0 \int_V dv \mathbf{E}_n \mathbf{E}_n^* = \mu_0 \int_V dv \mathbf{H}_n \mathbf{H}_n^* = 1 \tag{F.3}$$

where V is the volume of the cavity. Defining expansion coefficients by

$$a_n = \epsilon_0 \int_V dv \mathbf{E}\mathbf{E}_n^* \quad \text{and} \quad b_n = \mu_0 \int_V dv \mathbf{H}\mathbf{H}_n^* \; , \tag{F.4}$$

we obtain the approximate expansion for the true fields:

$$\mathbf{E} \simeq \sum_n a_n \mathbf{E}_n \quad \text{and} \quad \mathbf{H} \simeq \sum_n b_n \mathbf{H}_n \; . \tag{F.5}$$

This expansion is only approximate as it does not consider the penetration of the true fields into the walls of the cavity. It is also incomplete in the description of fields generated by the sources. The best approximation for the coefficients

a_n, b_n in the sense of a variational principle is obtained by taking matrixelements of Maxwell's equations:

$$\int_V dv \mathbf{H}_n^*(\mathbf{x}) \cdot (\nabla \times \mathbf{E}(\mathbf{x})) = i\omega b_n \tag{F.6}$$

$$\int_V dv \mathbf{E}_n^*(\mathbf{x}) \cdot (\nabla \times \mathbf{H}(\mathbf{x})) = c_n - i\omega a_n \tag{F.7}$$

where

$$c_n := \int_V dv \mathbf{J}(\mathbf{x}) \mathbf{E}_n^*(\mathbf{x}) \; . \tag{F.8}$$

Using $\nabla(\mathbf{a} \times \mathbf{b}) = \mathbf{b}(\nabla \times \mathbf{a}) - \mathbf{a}(\nabla \times \mathbf{b})$ the left hand sides can be rewritten. Performing the volume integration we can transform the volume integral over the divergence into a surface integral and obtain

$$\int_F df \hat{\mathbf{n}} \cdot (\mathbf{E} \times \mathbf{H}_n^*) + i\omega_n a_n = i\omega b_n \tag{F.9}$$

$$- \int_F df \hat{\mathbf{n}} \cdot (\mathbf{E}_n^* \times \mathbf{H}) - i\omega_n b_n = c_n - i\omega a_n \; . \tag{F.10}$$

Here $\hat{\mathbf{n}}$ is a normal vector pointing into the wall of the cavity. As the tangential component of $\mathbf{E}_n$ vanishes on the surface due to the boundary condition, the integral $\int_F df \hat{\mathbf{n}} (\mathbf{E}_n^* \times \mathbf{H})$ vanishes. On the other hand the true electric field $\mathbf{E}$ has a small tangential component due to the finite conductivity and finite penetration of the field into the wall. This small component can be estimated to be

$$\hat{\mathbf{n}} \times \mathbf{E} = \eta \mathbf{H} \quad \text{with} \quad \eta = (1 - i) R_A \tag{F.11}$$

where $R_A = \sqrt{\frac{\omega \mu_0}{2\sigma}}$ is the surface resistance (for a derivation see e. g. [Jac62][1]). Then the integral over the surface, leaving out the holes, becomes

$$\int_{F - F_1} df \hat{\mathbf{n}} (\mathbf{E} \times \mathbf{H}_n^*) = \int_{F - F_1} df \mathbf{H}_n^* (\hat{\mathbf{n}} \times \mathbf{E}) = \eta \int_{F - F_1} df \mathbf{H}_n^* \mathbf{H} \simeq \tag{F.12}$$

$$\simeq (1 - i) R_A \sum_m b_m \int_{F - F_1} df \mathbf{H}_n^* \mathbf{H}_m =: \sum_m h_{nm} b_m \; . \tag{F.13}$$

Let us assume that we know the fields on the holes and write

$$g_n := \int_{F_1} df \hat{\mathbf{n}} (\mathbf{E}_n^* \times \mathbf{H}) \tag{F.14}$$

[1] The normal vector $\hat{n}$ is defined in [Jac62] pointing into the vacuum, while here it is pointing into the metal.

then we obtain the equations

$$g_n + \sum_m h_{n,m} b_m + i\omega_n a_n = i\omega b_n \tag{F.15}$$

$$-i\omega_n b_n = c_n - i\omega a_n \; . \tag{F.16}$$

Eliminating a_n we obtain an equation for b_n

$$\left(\frac{\omega_n}{\omega} - \frac{\omega}{\omega_n}\right) b_n - \frac{i}{\omega_n} \sum_m h_{n,m} b_m = i\frac{c_n}{\omega} + i\frac{g_n}{\omega_n} \; . \tag{F.17}$$

Let us assume further that the opening is very small so that $g_n \approx 0$. For ω near a eigenfrequency ω_k the coefficient b_k is large and dominates the damping term. Introducing the quality factor Q_k by

$$\frac{h_{k,k}}{\omega_k} = (1-i) R_A \frac{\int df |\mathbf{H}_k|^2}{\omega_k} =: \frac{(1-i)}{Q_k} \tag{F.18}$$

we obtain

$$b_n = i\frac{c_n}{\omega} \left[\left(\frac{\omega_n}{\omega} - \frac{\omega}{\omega_n}\right) - \frac{1+i}{Q_n} \right]^{-1} \tag{F.19}$$

where $1/Q_n$ introduces a shift and damping of the resonance frequency. For the other modes with ω_n away from ω we may neglect the damping.

Now let us discuss an example where the cavity is excited by a Bloch oscillator device which is attached to the bottom of the cavity.

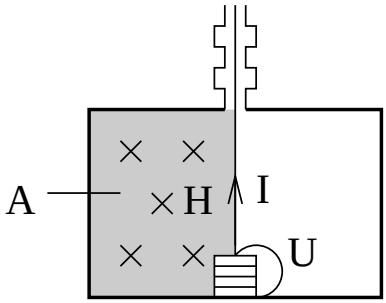

Fig. F.1: *The cavity with the superlattice attached to the bottom. A changing magnetic field H in the area A creates a voltage U that extends from the bottom to the top of the superlattice.*

From the top of the oscillator a wire extends to the top of the cavity. Here it leaves the cavity through a hole which isolates the DC current from the wall of the cavity, but is a short for high-frequency currents. The high-frequency currents circulate through the wire and back in the wall of the cavity. The coupling coefficients c_n between the current distribution and the electric fields of the eigenmodes of the cavity are given by

$$c_n = \int_V dv \mathbf{J} \cdot \mathbf{E}_n^* = I \int \mathbf{E}_n^* d\mathbf{s} \; . \tag{F.20}$$

Since the electric fields of the (ideal) eigenmodes have no tangential components along the wall of the cavity, the integral over the current density can be transformed into a line integral forming a closed loop, and therefore can be transformed into a surface integral over the flux of the eigenmode

$$c_n = I \int_A (\nabla \times \mathbf{E}_n^*) d\mathbf{f} = -i\omega_n \mu_0 I \int_A \mathbf{H}_n^* d\mathbf{f} \ . \tag{F.21}$$

It does not matter which loop we choose, the result should be independent from that. In the case of a circular cavity with the wire in the central axis only the modes with circular symmetry should couple.

On the other hand the total flux through the loop produces a voltage drop

$$U(t) = \frac{d\Phi(t)}{dt} \tag{F.22}$$

with the amplitude

$$U = -i\omega\mu_0 \int_A \mathbf{H} d\mathbf{f} \simeq -i\omega\mu_0 \sum_n b_n \int_A \mathbf{H}_n d\mathbf{f} \ . \tag{F.23}$$

Inserting the values of the expansion coefficients b_n we find

$$Z := \frac{U}{I} = -i \sum_n \omega_n l_n \left[\left(\frac{\omega_n}{\omega} - \frac{\omega}{\omega_n} \right) - \frac{1+i}{Q_n} \right]^{-1} \tag{F.24}$$

with

$$l_n := \mu_0^2 \left| \int_A \mathbf{H}_n d\mathbf{f} \right|^2 \ . \tag{F.25}$$

This ratio Z can be considered as entrance resistance (entrance impedance) of the cavity. It is the sum $Z = \sum_n Z_n$ of impedances from each mode

$$Z_n = -i\omega_n l_n \left[\left(\frac{\omega_n}{\omega} - \frac{\omega}{\omega_n} \right) - \frac{1+i}{Q_n} \right]^{-1} \ . \tag{F.26}$$

It is shown in Chapter 2 how this impedance can be modeled by an equivalent circuit.

Bibliography

[Bas96] G. Bastard: *Wave mechanics applied to semiconductor heterostructures*, les éditions de physique, Les Ulis Cedex, France (1988)

[Bloch28] F. Bloch: *Über die Quantenmechanik der Elektronen in Kristallgittern*, Z. Phys. **52**, 555 (1928)

[Bon03] L. L. Bonilla, R. Escobedo, A. Perales: *Generalized drift-diffusion model for miniband superlattices*, Phys. Rev. B **68**, 241304(R) (2003)

[Bon75] V. Bonch-Bruevich, I. Zvyagin, A. Mirnov: *Domain Instabilities in Semiconductors*, Consultants Bureau, New York, (1975)

[Cop66] J. A. Copeland: *A New Mode of Operation for Bulk Negative Resistance*, Proc. IEEE **54**, 1479 (1966)

[Cop67a] J. A. Copeland: *LSA Oscillator-Diode Theory*, J. Appl. Phys. **38**(8), 3096 (1967)

[Cop67b] J. A. Copeland: *Theoretical Study of a Gunn Diode in a Resonant Circuit*, IEEE Trans. El. Dev. **ED-14**(2), 55 (1967)

[Dun03] G. M. Dunn, M. J. Kearney: *A theoretical study of differing active region doping profiles for W-band (75-110 GHz) InP Gunn diodes*, Semicon. Sci. Technol. **18**, 794 (2003)

[Eav01] A. A. Krokhin, T. M. Fromhold, A E. Belyaev, H. M. Murphy, L. Eaves, D. Sherwood, P. C. Main, M. Henini: *Suppression of electron injection into a finite superlattice in an applied magnetic field*, Phys. Rev. B **63**, 195323 (2001)

[Eis04] H. Eisele: Institute of Microwaves and Photonics, School of Electronic and Electrical Engineering, University of Leeds, *private communications*

[Esa70] L. Esaki, R. Tsu: *Superlattice and Negative Differential Conductivity in Semiconductors*, IBM J. Res. Dev. **14**(1), 61 (1970)

[Fei04] T. Feil, W. Wegscheider, B. Rieder, J. Keller, M. Bichler, D. Schuh, G. Abstreiter: *Atomically precise modulated two-dimensional electron gas exhibiting stable negative differential resistance*, Physica E **22**, 733 (2004)

[Fri83] M: R. Friscourt, P. A. Rolland, A. Cappy, E. Constant, G. Salmer: *Theoretical Contribution to the Design of Millimeter-Wave TEO's*, IEEE Trans. El. Dev. **ED-30**(3), 223 (1983)

[Ger93] R. R. Gerhardts: *Effect of elastic scattering on miniband transport in semiconductor superlattices*, Phys. Rev. B **48**(12), 9178 (1993)

[Gre98] J. Grenzer: *Mikrowellenerzeugung mit Hilfe von GaAs/AlAs-Halbleiterübergitter-Bauelementen optimaler struktureller Qualität*, Logos-Verlag, Berlin (1998)

[Gue71] P. Guéret: *Convective and Absolute Instabilities in Semiconductors Exhibiting Negative Differential Mobility*, Phys. Rev. Lett. **27**(5), 9178 (1971)

[Gun63] J. B. Gunn: *Microwave oscillations in III-V semiconductors*, Solid State Commun. **1**(4), 88 (1963)

[Hau96] H. Haug, A. P. Jauho: *Quantum Kinetics in Transport and Optics of Semiconductors*, Springer-Verlag, Heidelberg (1996)

[Hil62] C. Hilsum: *Transferred electron amplifiers and oscillators*, Proc. IRE **50**(2), 185 (1962)

[Ign76] A. A. Ignatov, Yu. A. Romanov: *Nonlinear Electromagnetic Properties of Semiconductors with a Superlattice*, phys. stat. sol. (b) **73**, 327 (1976)

[Ign83] A. A. Ignatov, V. I. Shashkin: *A simplified approach to nonlinear HF response theory of superlattice materials*, Phys. Lett. **94**A, 169 (1983)

[Ign84] A. A. Ignatov, V. I. Shashkin: *Diffusion coefficient of heated carriers, spectrum of space-charge instability frequencies of semiconductor superlattices*, Sov. Phys. Semicond. **18**(4), 449 (1984)

[Ign91] A. A. Ignatov, E. P. Dodin, V. I. Shashkin: *Transient response theory of semiconductor superlattices: Connection with Bloch oscillation*, Mod. Phys. Lett. B **5**, 1087 (1991)

[Ign93] A. A. Ignatov, K. F. Renk, E. P. Dodin: *Esaki-Tsu Superlattice Oscillator: Josephson-Like Dynamics of Carriers*, Phys. Rev. Lett. **70**(13), 1996 (1993)

[Ign95] A. A. Ignatov, E. Schomburg, J. Grenzer, K. F. Renk, E. P. Dodin: *THz-field induced nonlinear transport and dc voltage generation in a semiconductor due to Bloch oscillations*, Z. Phys. B **98**, 187 (1995)

[Iko69] T. Ikoma, H. Torizuka, H. Yanai: *Observation of voltage and current waveforms of the transferred-electron oscillators*, Proc. IEEE **57**, 340 (1969)

[Jac83] C. Jacoboni, L. Reggiani: *The Monte Carlo method for the solution of charge transport in semiconductors with application to covalent materials*, Rev. Mod. Phys. **55**(3), 645 (1983)

[Ivc97] E. L. Ivchenko, G. E. Pikus: *Superlattices and Other Heterostructures*, Second Edition, Springer, Heidelberg, (1997)

[Jac62] J. D. Jackson: *Classical Electrodynamics*, John Wiley and Sons Inc., New York, (1962)

[Jon73] D. Jones, H. D. Rees: *A reappraisal of instabilities due to the transferred electron effect*, J. Phys. C **6**, 1781 (1973)

[Kan59] E. O. Kane: *Zener Tunneling in Semiconductors*, J. Phys. Chem. Solids **12**, 181 (1959)

[Kan60] E. O. Kane: *Theory of Tunneling*, J. Appl. Phys. **32**(1), 83 (1960)

[Kel62] L. Keldysh: *Optical Characteristics of Electrons with a Band Energy Spectrum in a Strong Electric Field*, Sov. Phys. JETP. **16**(2), 471 (1963), Zh. Eksp. Teor. Fiz. **43**, 661 (1962)

[Ken67] W. K. Kennedy, L. F. Eastman: *LSA operation of large volume bulk GaAs samples*, IEEE Trans. **ED-14**(9), 500 (1967)

[Kir84] O. A. Kireev, M. E. Levinshtein, S. L. Rumjantsev: *Anode domain transient processes in supercritical Gunn diodes*, Solid State Electronics **27**(3), 233 (1984)

[Kla04] F. Klappenberger, K. N. Alekseev, K. F. Renk, R. Scheuerer, E. Schomburg, S. J. Allen, G. R. Ramian, S. S. Scott, A. Kovsh, V. Ustinov, A. Zhukov: *Ultrafast creation and annihilation of space-charge domains in a semiconductor superlattice observed by use of Terahertz fields*, Eur. Phys. J. B **39**(4), 483 (2004)

[Kla04a] F. Klappenberger, P. Renk, K. F. Renk, B. Rieder, D. G. Pavelev, V. Ustinov, A. Zhukov, N. Maleev, A. Vasilyev: *Semiconductor-superlattice frequency multiplier for generation of submillimeter waves*, Appl. Phys. Lett. **84**(19), 3924 (2004)

[Kov04] Y. Koval, M. V. Fistul, A. V. Ustinov: *Enhancement of Josephson phase diffusion by microwaves*, Phys. Lett. A **93**, 087004 (2004)

[Kri86] J. B. Krieger, G. J. Jafrate: *Time Evolution of Bloch electrons in a homogeneous electric field*, Phys. Rev. B **33**(8), 5494 (1986)

[Kro31] R. d. L. Kronig, W. G. Penney: *Quantum Mechanics of Electrons in Crystal Lattices*, Proc. Roy. Soc. A **130**, 499 (1931)

[Kro64] H. Kroemer: *Theory of the Gunn effect*, Proc. IEEE **52**(12), 1736 (1964)

[Kro66] H. Kroemer: *Nonlinear Space-Charge Domain Dynamics in s Semiconductor with Negative Differential Mobility*, IEEE Trans. El. Dev. **13**(1), 27 (1966)

[Kro68] H. Kroemer: *The Gunn Effect Under Imperfect Cathode Boundary Conditions*, IEEE Trans. El. Dev. **15**(11), 819 (1968)

[Kro78] H. Kroemer: *Hot-electron relaxation effects in devices*, Solid St. Electronics **21**, 61 (1978)

[Kro00a] H. Kroemer: *Large-amplitude oscillation dynamics and domain suppression in a superlattice Bloch oscillator*, cond-mat/0009311, (2000)

[Kro00b] H. Kroemer: *On the nature of the negative-conductivity resonance in a superlattice Bloch oscillator*, cond-mat/0007482, (2000)

[Kti72] S. A. Ktitorov, G. S. Simin, V. Ya. Sindalovskii: *Bragg reflections and the high-frequency conductivity of an electronic solid-state plasma*, Soviet Physics - Solid State **13**(8), 1872 (1972)

[Kuh98] T. Kuhn: in *Theory of Transport Properties of Semiconductor Nanostructures*, edited by E. Schöll (Chapman and Hall, London, 1998)

[Cao99] J. C. Cao, X. L. Lei: *Synchronization and chaos in miniband semiconductor superlattices*, Phys. Rev. B **60**(3), 1871 (1999)

[Lev79] M. E. Levinshtein, G. S. Simin: *Dynamics of disappearance of a Gunn domain in the anode*, Sov. Phys. Semicond. **13**(5), 529 (1979)

[McC66] D. E. McCumber, A. G. Chynoweth: *Theory of Negative-Conductance Amplification and of Gunn Instabilities in "Two-Valley" Semiconductors*, IEEE Trans. El. Dev. **ED-13**(1), 4 (1966)

[Per04] Á. Perales, L. L. Bonilla, R. Escobedo: *Miniband transport and oscillations in semiconductor superlattices*, Nanotechnology **15**, 229 (2004)

[Pfe90] L. N. Pfeiffer, K. West, H. L. Störmer, J. P. Eisenstein, K. W. Baldwin, D. Gershoni, J. Spector: *Formation of a high quality two-dimensional electron gas on cleaved GaAs*, Appl. Phys. Lett. **56**, 1697 (1990)

[Rid61] B. K. Ridley, T. B. Watkins: *The possibility of negative resistance*, Proc. Phys. Soc. **78**(8), 293 (1961)

[Rid63] B. K. Ridley: *Specific negative resistance in solids*, Proc. Phys. Soc. **82**(12), 954 (1963)

[Ryn03] D. Ryndyk, N. V. Demarina, J. Keller, E. Schomburg: *Superlattice with hot electron injection: an approach to a Bloch oscillator*, Phys. Rev. B **67**(3), 33305 (2003)

[Sav04] P. G. Savvidis, B. Kolasa, G. Lee, and S. J. Allen: *Resonant crossover of terahertz loss to gain in a Bloch oscillating InAs/AlSb super-superlattice*, Phys. Rev. Lett. **92**, 196802 (2004)

[Sch02a] R. Scheuerer, E. Schomburg, K. F. Renk, A. Wacker, E. Schöll: *Feasibility of a semiconductor oscillator based on quenched domains for the generation of submillimeter waves*, Appl. Phys. Lett. **81**(8), 1515 (2004)

[Sch02b] R. Scheuerer: *Domänendynamik in Halbleiter-Übergittern*, Dissertation, Regensburg (2002)

[Sch98a] E. Schöll (Editor): *Theory of Transport Properties of Semiconductor Nanostructures*, vol.4 of *Electronic Materials Series*, Chapman and Hall, London (1998)

[Sch98b] E. Schomburg, T. Blomeier, K. Hofbeck, J. Grenzer, S. Brandl, I. Lingott, A. A. Ignatov, K. F. Renk, D. G. Pavel'ev, Yu. Koschurinov, B. Ya. Melzer, V. M. Ustinov, S. V. Ivanov, A. Zhukov, P. S. Kop'ev: *Current oscillation in superlattices with different miniband widths*, Phys. Rev. B **58**(7), 4035 (1998)

[Sch99a] E. Schomburg, M. Henini, J. M. Chamberlain, D. P. Stevenson, S. Brandl, K. Hofbeck, K. F. Renk, W. Wegscheider: *Self-sustained current oscillations above 100 GHz in a GaAs/AlAs superlattice*, Appl. Phys. Lett. **74**, 2179 (1999)

[Sch99b] E. Schomburg, R. Scheuerer, S. Brandl, K. F. Renk, D. G. Pavel'ev, Yu. Koschurinov, A. Zhukov, A. Kovsh, P. S. Kop'ev: *InGaAs/InAlAs superlattice oscillator at 147 GHz*, Electronics Letters **35**(1), 4035 (1999)

[Sch03] E. Schomburg, N. V. Demarina, K. F. Renk: *Amplification of a terahertz field in a semiconductor superlattice via phase-locked k-space bunches of Bloch oscillating electrons*, Phys. Rev. B **67**(15), 155302 (2003)

[Shu86] M. Shur: *GaAs devices and circuits*, Plenum Press, New York (1986)

[Sib89] A. Sibille: *Calculations of Zener interminiband tunneling rates in superlattices*, Solid State Electronics **32**(12), 1455 (1989)

[Suc98] M. Sucheka: *The doping notch in the numerical modeling of uniformly doped transferred electron devices*, Electron Technology **31**(2), 242 (1998)

[Thi67] H. W. Thim, S. Knight: *Carrier generation and switching phenomena in n-GaAs devices*, Appl. Phys. Lett. **11**(3), 83 (1967)

[Thi71] H. Thim: *Stability and Switching in Overcritically Doped Gunn Diodes*, Proc. IEEE **59**, 1285 (1971)

[Ung89] H. G. Unger: *Elektromagnetische Theorie für die Hochfrequenztechnik*, Teil II, Dr. Alfred Hüthig Verlag, Heidelberg (1989)

[Wac02] A. Wacker: *Semiconductor Superlattices: A model system for nonlinear transport*, Phys. Rep. **357**, 1 (2002)

[Zen32] C. Zener: *Non-Adiabatic Crossing of Energy Levels*, Proc. Roy. Soc. **A137**, 696 (1932)

[Zen34] C. Zener: *A Theory of the Electrical Breakdown of Solid Dielectrics*, Proc. Roy. Soc. **A145**, 523 (1934)

Acknowledgements

First of all I thank my advisor **Prof. Dr. Joachim Keller** for his support and continuous interest in my work. His permanent willingness to discuss problems related to my work and physics in general was crucial for the development of this thesis and a better comprehension of many physical phenomena.

I am most thankful to **Prof. Dr. Karl F. Renk** for giving me the opportunity to cooperate with a very active group in the field of semiconductor superlattices. Particularly I would like to thank **Dr. habil. Ekkehard Schomburg**, **Dr. Roland Scheuerer**, **Dr. Michael Häußler**, **Dr. Florian Klappenberger**, **Dr. Natalia Demarina**, and **Anatoly Glukhovskoy** for the introduction into the field and countless discussions. Florian deserves special credit for permanently coming up with ideas for further calculations and constructive comments on the results.

I thank **Thomas Feil** for numerous discussions on superlattice physics.

It was a pleasure to work at the chair of **Prof. Dr. Klaus Richter** where a wonderful working atmosphere was provided by many people over the years:

- **Dr. Dmitry Ryndyk** who stoically tolerated the chaos before and during the DPG Spring Meeting 2002 and had an answer to almost any question,
- my changing roommates **Dr. Robert Zitzler** who sacrificed his time for proof-reading the thesis, **Dr. Grigory Tkachov**, **Dr. Marko Turek**, **Christian Lechner**, and **Michael Wimmer** who were often asked for assistance in physics problems and for technical support,
- the other PhD students **Dr. Josef Kainz**, **Dr. Andreas Jung**, **Andreas Laßl**, and **Tobias Paul** who were helpful on many occasions,
- and of course **Angela Reißer** who always friendly handled all the organizational matters.

Finally, I would like to thank my **parents** for their long-standing support in my education.

This research was supported by the **Deutsche Forschungsgemeinschaft**, Graduiertenkolleg *Nichtlinearität und Nichtgleichgewicht in kondensierter Materie*.